

Imperial College of Science, Technology and Medicine
Department of Electrical and Electronic Engineering
Control and Power Research Group

Energy Management of Hybrid and Battery Electric Vehicles

Arghavan Nazemi

Submitted in part fulfilment of the requirements for the degree of
Doctor of Philosophy in Electrical and Electronic Engineering of Imperial College London and
the Diploma of Imperial College, October 2022

Declaration

I hereby declare, that to the best of my knowledge, the content of this thesis is my own, except where sources have been referenced or acknowledged. This thesis has not been submitted for any other degrees.

The copyright of this thesis rests with the author. Unless otherwise indicated, its contents are licensed under a Creative Commons Attribution-Non Commercial 4.0 International Licence (CC BY-NC). Under this licence, you may copy and redistribute the material in any medium or format. You may also create and distribute modified versions of the work. This is on the condition that: you credit the author and do not use it, or any derivative works, for a commercial purpose. When reusing or sharing this work, ensure you make the licence terms clear to others by naming the licence and linking to the licence text. Where a work has been adapted, you should indicate that the work has been changed and describe those changes. Please seek permission from the copyright holder for uses of this work that are not included in this licence or permitted under UK Copyright Law.

Abstract

This work focuses on improving the fuel economy of parallel Hybrid Electric Vehicles (HEVs) and dual-motor Electric Vehicles (EVs) through energy management strategies. Both vehicle models have two propulsion branches, each powering a separate axle: An engine and an electric motor in the HEV and two electric motors in the EV. This similarity in the vehicle models emphasises the need for similar energy management solutions.

In **Part Energy Management of HEVs** of this thesis, a high-fidelity parallel Through-The-Road (TTR) HEV model is developed to study and test conventional control strategies. The traditional control strategies serve as a guide for developing novel heuristic control strategies. The Equivalent Consumption Minimisation Strategy (ECMS) is an optimisation-based control strategy used as the benchmark in this part of the work.

A family of rule-based energy management strategies is proposed for parallel HEVs, including the Torque-levelling Threshold-changing Strategy (TTS) and its simplified version, the Simplified Torque-levelling Threshold-changing Strategy (STTS). The TTS applies a concept of torque-levelling, which ensures the engine works efficiently by operating with a constant torque as the load demand crosses a certain threshold, unlike the load-following approach commonly used. However, the TTS requires finely tuned constant torque and threshold parameters, making it unsuitable for real-time applications. To address this, two feedback-like updating laws are incorporated into the TTS to determine the constant torque and threshold online for real-time applications. Real-time versions of these strategies, Real-time Torque-levelling Threshold-changing Strategy (RTTS) and Real-time Simplified Torque-levelling Threshold-changing Strategy (RSTTS), are developed using a novel Driving Pattern Recognition (DPR) algorithm. The effectiveness of the RTTS is demonstrated by implementing it on a high-fidelity parallel hybrid passenger car and benchmarking it against ECMS.

In **Part Energy Management of EVs** of the thesis, a low-fidelity model of a novel EV powertrain with two electric propulsion systems, one at each axle, has been developed to study and test its energy management with one of the main conventional optimal control methods, Dynamic Programming (DP). The EV model uses two differently sized traction motors at the front and rear axles. The thermal dynamics of the utilised Permanent Magnet Synchronous Motors (PMSMs) are studied. DP is first implemented onto the Baseline model that does not include any PMSM thermal dynamics, referred to as the **Baseline DP**, which acts as a benchmark since it is the conventional case. The

thermal dynamics of the traction motors are then introduced in the second DP problem formulation, referred to as the **Thermal DP**, which is compared against the Baseline DP to evaluate the possible benefits of energy efficiency by the more informed energy management optimisation formulation. The best method is chosen to include these thermal dynamics in the overall energy management control strategy without significantly compromising computational time.

Acknowledgements

I would like to express my gratitude to my supervisor, Dr. Simos Evangelou, for his constant support. My colleagues Luna, Richard, Nikos, Georgios, Nico, Roberto and Miles for their non-stop encouragement. My dad and brother for believing in me. Finally, my mother, for teaching me resilience and strength through her fight against cancer.

List of Abbreviations

BSFC Brake Specific Fuel Consumption

CS Charge-Sustaining

DP Dynamic Programming

DPR Driving Pattern Recognition

EACS Electric Assist Control Strategy

ECMS Equivalent Consumption Minimisation Strategy

EFC Equivalent Fuel Consumption

EM Electric Motor

EMMS Efficiency Maximising Map Strategy

EPA Environmental Protection Agency

EV Electric Vehicle

FEM Finite Element Method

HIL Hardware-In-the-Loop

GHG Greenhouse Gas

HEV Hybrid Electric Vehicle

ICE Internal Combustion Engine

LPTN Lumped Parameter Thermal Network

MC Markov-chain

MPC Model Predictive Control

NRDC National Resources Defence Council

NN Neural Network

OPSS Optimal Primary Source Strategy

PFCS Power Follower Control Strategy

PMP Pontrygain's Minimum Principle

PMSM Permanent Magnet Synchronous Motor

RSTTS Real-time Simplified Torque-levelling Threshold-changing Strategy

RTTS Real-time Torque-levelling Threshold-changing Strategy

SCS Supervisory Control Strategy

SOC State of Charge

SSS Start-Stop System

STTS Simplified Torque-levelling Threshold-changing Strategy

TCS Thermostat Control Strategy

TTR Through-The-Road

TTS Torque-levelling Threshold-changing Strategy

V2G Vehicle to Grid

WLTP Worldwide Harmonised Light vehicle Test Procedure

XOS Exclusive Operation Strategy

Contents

Abstract	iii
Acknowledgements	v
I Intro	1
1 Introduction	2
1.1 Rationale	2
1.2 Motivation and Objectives	3
1.3 Contributions	5
1.4 Outline	5
2 Literature Review	8
2.1 Brief History	8
2.1.1 HEV Architectures	10
2.1.2 HEV Advantages and Disadvantages	10
2.1.3 EV Architectures	12

2.1.4	EV Advantages and Disadvantages	14
2.2	Vehicle Modelling Topology	17
2.2.1	Forward-facing	17
2.2.2	Backward-facing	17
2.3	HEV and EV Control Strategies	18
2.3.1	Optimisation-based Strategies	18
2.3.2	Rule-based Strategies	19
2.3.3	Real-time Control Strategies	21
2.4	Thermal Modelling of Electric Motors	22
2.4.1	Finite Element Method (FEM)	22
2.4.2	Rotor Flux-based Estimation	22
2.4.3	Rotor High-frequency Impedance Based Estimation	22
2.4.4	Lumped Parameter Thermal Networks (LPTNs)	23

II Energy Management of HEVs 25

3 Hybrid Electric Vehicle Model 26

3.1	Background	26
3.2	Primary Source	26
3.2.1	Engine Model	27
3.2.2	Start-Stop System (SSS)	30
3.2.3	ICE Gearbox	30

3.3	Secondary Source	31
3.3.1	Battery	31
3.3.2	DC-DC Converter	32
3.3.3	DC Link	32
3.3.4	Inverter	33
3.3.5	Permanent Magnet Synchronous Motor (PMSM)	33
3.3.6	PMSM Transmission	34
3.4	Driver Model	35
3.5	System Integration	35
3.6	Chapter Summary	36
4	Conventional Control Strategies for the Energy Management of HEVs	37
4.1	Design and Implementation of ECMS	37
4.1.1	Fuel Economy Evaluation	38
4.1.2	Equivalent Fuel Consumption Minimisation Strategy (ECMS)	39
4.2	Chapter Summary	45
5	Heuristic Control Strategies for the Energy Management of HEVs	46
5.1	Torque-Levelling Threshold-Changing Strategy (TTS)	46
5.2	Simplified Torque-levelling Threshold-changing Strategy (STTS)	50
5.3	Novel Real-time Heuristic Control Strategies	51
5.3.1	Real-time Torque-levelling Threshold-changing Strategy (RTTS)	52

5.3.2	Real-time Simplified Torque-levelling Threshold-changing Strategy (RSTTS)	54
5.4	Chapter Summary	55
6	Simulation Results for the Energy Management of HEVs	56
6.1	Implementation of the ECMS, TTS and STTS	56
6.1.1	Power Profiles	57
6.1.2	SOC Profiles	64
6.1.3	Fuel Economy	67
6.2	Implementation of the RTTS and RSTTS	69
6.2.1	Power Profiles	70
6.2.2	Torque Profiles	72
6.2.3	SOC Profiles	73
6.2.4	Fuel Economy	74
6.3	Chapter Summary	78
III	Energy Management of EVs	79
7	Electric Vehicle Model	80
7.1	Baseline EV Model	81
7.1.1	Battery Model	81
7.1.2	DC-DC Converter	83
7.1.3	DC Link	83

7.1.4	Inverter	83
7.1.5	Permanent Magnet Synchronous Motor (PMSM)	84
7.2	Thermal EV Model	87
7.2.1	Thermal Dynamic Modelling of the PMSMs	87
7.3	System Integration	95
7.4	Chapter Summary	97
8	Optimal Control Problem & Results for the Energy Management of EVs	98
8.1	Optimal Control Problem Formulation	98
8.2	Baseline DP	99
8.2.1	Baseline Model System Integration	99
8.2.2	Baseline Optimal Control Problem Formulation	100
8.3	Thermal DP	102
8.3.1	Thermal Model System Integration	102
8.3.2	Thermal Optimal Control Problem Formulation	103
8.4	Dynamic Programming Solutions and Simulation Results	104
8.4.1	Torque and Power Split Profiles	104
8.4.2	Temperature Profiles	106
8.4.3	Torque, Speed and Temperature Operating Points	107
8.4.4	Powertrain Efficiency and Losses	109
8.4.5	SOC Profiles	115
8.5	Chapter Summary	116

IV Conclusion 117

9 Conclusion 118

9.1 Summary of Achievements 118

9.2 Future Work 120

Bibliography 122

List of Tables

3.1	Engine model Alpha parameters	29
3.2	Engine model Beta parameters	29
3.3	Gear ratio values	30
3.4	Li-on battery parameters	32
4.1	EFC equivalence factors for the model Alpha	39
4.2	EFC equivalence factors for the model Beta	39
4.3	Optimal ECMS equivalence factors for the model Alpha	40
4.4	Optimal ECMS equivalence factors for the model Beta	41
5.1	TTS optimal parameters for the model Alpha	51
5.2	TTS optimal parameters for the model Beta	51
5.3	STTS optimal parameters for the model Alpha	51
6.1	Fuel economy of the ECMS for the model Alpha	67
6.2	Fuel economy of the ECMS for the model Beta	67
6.3	Fuel economy of the TTS for the model Alpha	67

6.4	Fuel economy of the TTS for the model Beta	67
6.5	Fuel economy of the STTS for the model Alpha	68
6.6	Fuel economy of the ECMS over the WLTP and the Experimental drive cycle for the model Alpha	77
6.7	Fuel economy of the RTTS over the WLTP and the Experimental drive cycles for the model Alpha	77
6.8	Fuel economy of the RSTTS over the WLTP and the Experimental drive cycles for the model Alpha	77
6.9	Fuel economy of the ECMS over the WLTP and the Experimental drive cycles for the model Beta	77
6.10	Fuel economy of the RTTS over the WLTP and the Experimental drive cycles for the model Beta	77
7.1	Li-on battery parameters	82
7.2	Front and Rear PMSM parameters	85
7.3	Front and Rear PMSM second-order thermal dynamics parameters	95
8.1	Front and Rear PMSM energy losses for the Baseline and Thermal DP case studies, over the JN1015 drive cycle	110
8.2	Energy losses over the JN1015 drive cycle in other powertrain components: Inverter, Battery and Gearbox	113
8.3	Final SOC for the Baseline and Thermal DP case studies	115

List of Figures

2.1	Classification of HEVs [1]	11
3.1	The overall architecture of the TTR HEV.	27
3.2	Block diagram showing the interconnection of the Battery, DC-DC converter, DC link, Inverter, Permanent Magnet Synchronous Motor (PMSM), Gearbox (Gbox), Rear transmission system (Transmission), Internal Combustion Engine (ICE), Supervisory Control Strategy (SCS), Driver and Car.	27
3.3	Engine model Alpha efficiency maps	28
3.4	Engine model Beta efficiency maps	29
3.5	Gear ratio as a function of vehicle speed.	31
3.6	DC-DC converter efficiency for varying values of load power.	33
3.7	Inverter efficiency for varying values of load power.	33
3.8	PMSM steady-state power efficiency map for variations in the load torque T_m , and rotor speed ω_m . As only forward vehicle motion is considered in this work, the rotor speed is always non-negative, and the PMSM has two modes of operation: 1) positive T_m (motoring) and 2) negative T_m (regenerating). The contours correspond to constant efficiencies in the range 75-96%.	34

4.1	Correlation between the electrical energy E_e , and the fuel energy E_f , for driving cycles WL-L (a), WL-M (b), WL-H (c) and WL-E (d) for the model Alpha.	41
4.2	Optimal ECMS power share factor maps for the standard driving cycles for the model Alpha; dark blue corresponds to pure electric mode, and white represents the infeasible region. The maps are for driving cycles WL-L (a), WL-M (b), WL-H (c) and WL-E (d).	42
4.3	Correlation between the electrical energy E_e , and the fuel energy E_f , for driving cycles WL-L (a), WL-M (b), WL-H (c) and WL-E (d) for the model Beta.	43
4.4	Optimal ECMS power share factor maps for the standard driving cycles for the model Beta; dark blue corresponds to pure electric mode, and white represents the infeasible region. The maps are for driving cycles WL-L (a), WL-M (b), WL-H (c) and WL-E (d).	44
5.1	Optimal TTS power share factor for WL-L, WL-M, WL-H and WL-E, left to right, respectively; the top row consists of maps at the cross-section of $\omega = \omega_{mid}$ and the bottom row at $SOC = SOC_{mid}$. Dark blue corresponds to pure electric mode, and white represents the infeasible region. These maps are for the engine model Alpha.	49
5.2	Optimal TTS power share factor for WL-L, WL-M, WL-H and WL-E, left to right, respectively; the top row consists of maps at the cross-section of $\omega = \omega_{mid}$ and the bottom row at $SOC = SOC_{mid}$. Dark blue corresponds to pure electric mode, and white represents the infeasible region. These maps are for the engine model Beta.	49
5.3	The TTS operates in three distinct modes depending on the given SOC , ω_e and P_{PL} : Electric mode (yellow), constant ICE torque mode (green), maximum ICE power mode (blue). White represents the infeasible region.	50
5.4	DPR block diagram.	53
6.1	Four components of the WLTP (WL-L, WL-M, WL-H and WL-E).	57

6.2	ECMS power time profiles for the engine power P_{ed} , motor/generator power P_{md} , and load power P_{PL} for the first iteration of driving cycles WL-L, WL-M, WL-H, and WL-E, top to bottom. These plots are for the model Alpha.	59
6.3	ECMS power time profiles for the engine power P_{ed} , motor/generator power P_{md} , and load power P_{PL} for the first iteration of driving cycles WL-L, WL-M, WL-H, and WL-E, top to bottom. These plots are for the model Beta.	60
6.4	TTS power time profiles for the engine power P_{ed} , motor/generator power P_{md} , and load power P_{PL} for the first iteration of driving cycles WL-L, WL-M, WL-H, and WL-E, top to bottom. These plots are for the model Alpha.	61
6.5	TTS power time profiles for the engine power P_{ed} , motor/generator power P_{md} , and load power P_{PL} for the first iteration of driving cycles WL-L, WL-M, WL-H, and WL-E, top to bottom. These plots are for the model Beta.	62
6.6	STTS power time profiles for the engine power P_{ed} , motor/generator power P_{md} , and load power P_{PL} for the first iteration of driving cycles WL-L, WL-M, WL-H, and WL-E, top to bottom. These plots are for the model Alpha.	63
6.7	SOC time profiles of the ECMS, TTS and STTS for the first iteration of driving cycles WL-L (a), WL-M (b), WL-H (c), and WL-E (d). These plots are for the model Alpha.	65
6.8	SOC time profiles of the ECMS, TTS and STTS for the first iteration of driving cycles WL-L (a), WL-M (b), WL-H (c), and WL-E (d). These plots are for the model Beta.	66
6.9	Comparison of the fuel economy of the TTS relative to the performance of the ECMS for the WL-L, WL-M, WL-H and WL-E drive cycles for the model Alpha.	68
6.10	Comparison of the fuel economy of the TTS relative to the performance of the ECMS for the WL-L, WL-M, WL-H and WL-E drive cycles for the model Beta.	68
6.11	The Experimental drive cycle collected in London.	69

6.12	Power profiles of the engine and the propulsion load of the ECMS and the RTTS over the WLTP (top) and the Experimental drive cycle (bottom) for the model Alpha. . . .	70
6.13	Power profiles of the engine and the propulsion load of the ECMS and the RTTS over the WLTP (top) and the Experimental drive cycle (bottom) for the model Beta. . . .	71
6.14	Power profiles of the engine and the propulsion load of the ECMS and the RSTTS over the WLTP (top) and the Experimental drive cycle (bottom) for the model Alpha.	71
6.15	RTTS engine torque T_e , over the WLTP (top) and the Experimental drive cycle (bottom) for the model Alpha.	72
6.16	RTTS engine torque T_e , over the WLTP (top) and the Experimental drive cycle (bottom) for the model Beta.	73
6.17	RSTTS engine torque T_e , over the WLTP (top) and the Experimental drive cycle (bottom) for the model Alpha.	74
6.18	SOC profiles of the ECMS, RTTS and the RSTTS over the WLTP (top) and the Experimental drive cycle (bottom) for the model Alpha.	75
6.19	SOC profiles of the ECMS and the RTTS over the WLTP (top) and the Experimental drive cycle (bottom) for the model Beta.	75
6.20	Comparison of the fuel economy of the RTTS relative to the performance of the ECMS over the WLTP and the Experimental driving cycles for the model Alpha. . .	76
6.21	Comparison of the fuel economy of the RTTS relative to the performance of the ECMS over the WLTP and the Experimental driving cycles for the model Beta. . . .	76
6.22	Comparison of the fuel economy of the RSTTS relative to the performance of the ECMS over the WLTP and the Experimental driving cycles for the model Alpha. . .	76
7.1	Overall architecture of the dual-motor EV.	80
7.2	Internal battery resistance as a function of SOC.	82

7.3	Battery open circuit voltage as a function of SOC.	83
7.4	PMSM steady-state power efficiency maps for the variations in the front PMSM load torque $T_{m,F}$, and the front rotor speed $\omega_{m,F}$ (left); the rear PMSM load torque $T_{m,R}$, and the rear rotor speed $\omega_{m,R}$ (right). As only the forward vehicle motion is considered in this work, the rotor speed is always non-negative, and the PMSM has two modes of operation: 1) positive torque (motoring) and 2) negative torque (regenerating). The contours correspond to constant efficiencies.	86
7.5	The front PMSM steady-state power efficiency maps for variations in the load torque $T_{m,F}$, and the front rotor speed $\omega_{m,F}$, for six different motor stator windings' temperatures. As only forward vehicle motion is considered in this work, the rotor speed is always non-negative, and the PMSM has two modes of operation: 1) positive $T_{m,F}$ (motoring) and 2) negative $T_{m,F}$ (regenerating). The contours correspond to constant efficiencies. The depicted efficiencies correspond to temperatures of $-40\text{ }^{\circ}\text{C}$ (a), $0\text{ }^{\circ}\text{C}$ (b), $40\text{ }^{\circ}\text{C}$ (c), $80\text{ }^{\circ}\text{C}$ (d), $120\text{ }^{\circ}\text{C}$ (e) and $165\text{ }^{\circ}\text{C}$ (f).	92
7.6	The rear PMSM steady-state power efficiency maps for variations in the load torque $T_{m,R}$, and the rear rotor speed $\omega_{m,R}$, for six different motor stator windings' temperatures. As only forward vehicle motion is considered in this work, the rotor speed is always non-negative, and the PMSM has two modes of operation: 1) positive $T_{m,R}$ (motoring) and 2) negative $T_{m,R}$ (regenerating). The contours correspond to constant efficiencies. The depicted efficiencies correspond to temperatures of $-40\text{ }^{\circ}\text{C}$ (a), $0\text{ }^{\circ}\text{C}$ (b), $40\text{ }^{\circ}\text{C}$ (c), $80\text{ }^{\circ}\text{C}$ (d), $120\text{ }^{\circ}\text{C}$ (e) and $165\text{ }^{\circ}\text{C}$ (f).	93
7.7	Thermal equivalent circuit of the PMSM.	94
7.8	The testing (test) and simulation (sim) temperatures of the front PMSM stator windings $\theta_{Cu,F}$, and the front PMSM rotor temperature $\theta_{Fe,F}$	94
7.9	The testing (test) and simulation (sim) temperatures of the rear PMSM stator windings $\theta_{Cu,R}$, and the rear PMSM rotor temperature $\theta_{Fe,R}$	94

8.1	Velocity and acceleration profiles of the JN1015 drive cycle (right), Gear number used over the JN1015 drive cycle (left).	104
8.2	The Baseline DP optimal torque split between the front and rear motors over the JN1015 drive cycle. $T_{m,F}$ and $T_{m,R}$ denote the front and rear motor driving torques and T_{Br} denotes the mechanical braking torque.	105
8.3	The Thermal DP optimal torque split between the front and rear motors over the JN1015 drive cycle. $T_{m,F}$ and $T_{m,R}$ denote the front and rear motor driving torques and T_{Br} denotes the mechanical braking torque.	105
8.4	The Baseline DP optimal power split between the front and rear motors over the JN1015 drive cycle. $P_{m,F}$ and $P_{m,R}$ denote the front and rear motor driving torques and P_{Br} denotes the mechanical braking torque.	105
8.5	The Thermal DP optimal power split between the front and rear motors over the JN1015 drive cycle. $P_{m,F}$ and $P_{m,R}$ denote the front and rear motor driving torques and P_{Br} denotes the mechanical braking torque.	106
8.6	Time histories of the front and rear motors' stator windings' temperatures for the Baseline and Thermal DP case studies over the JN1015 drive cycle.	106
8.7	Time histories of the front and rear motors' rotor temperatures for the Baseline and Thermal DP case studies over the JN1015 drive cycle.	106
8.8	Torque versus angular speed of the front motor for the Baseline and Thermal DP case studies, over the JN1015 drive cycle.	107
8.9	Torque versus angular speed of the rear motor for the Baseline and Thermal DP case studies, over the JN1015 drive cycle.	108
8.10	Torque versus angular speed Baseline DP operating points of the front motor over the JN1015 drive cycle, superimposed on the front motor efficiency map at a constant temperature of 10 °C.	108

8.11 Torque versus angular speed Baseline DP operating points of the rear motor over the JN1015 drive cycle, superimposed on the rear motor efficiency map at a constant temperature of 10 °C.	109
8.12 The stator windings' temperature of the front motor shown for the temperature intervals of 10 to 25 °C (top left), 25 to 40 °C (top right), 40 to 55 °C (bottom left) and 55 to 70 °C (bottom right). The efficiency visualised in every interval is the average of the respective temperature interval.	110
8.13 Stator windings' temperature of the rear motor shown for the temperature intervals of 10 to 25 °C (top left), 25 to 40 °C (top right), 40 to 55 °C (bottom left) and 55 to 70 °C (bottom right). The efficiency visualised in every interval is the average of the respective temperature interval.	111
8.14 Front PMSM Copper loss $P_{Cu,F}$, for the Baseline and Thermal DP case studies over the JN1015 drive cycle.	111
8.15 Rear PMSM copper loss $P_{Cu,R}$, for the Baseline and Thermal DP case studies over the JN1015 drive cycle.	112
8.16 Front PMSM Iron loss $P_{Fe,F}$, for the Baseline and Thermal DP case studies over the JN1015 drive cycle.	112
8.17 Rear PMSM Iron loss $P_{Fe,R}$, for the Baseline and Thermal DP case studies over the JN1015 drive cycle.	112
8.18 Total front PMSM loss $P_{L,F}$, for the Baseline and Thermal DP case studies over the JN1015 drive cycle.	113
8.19 Total rear PMSM loss $P_{L,R}$, for the Baseline and Thermal DP case studies over the JN1015 drive cycle.	113
8.20 Time profile of the front PMSM efficiency e_F , for the Baseline and Thermal DP case studies over the JN1015 drive cycle.	114

8.21	Time profile of the rear PMSM efficiency e_R , for the Baseline and Thermal DP case studies over the JN1015 drive cycle.	114
8.22	Comparison of the drivetrain losses between the Baseline and Thermal DP case studies over the JN1015 drive cycle.	114
8.23	SOC time profiles of the Baseline and Thermal DP case studies over the JN1015 drive cycle.	115

Part I

Intro

Chapter 1

Introduction

1.1 Rationale

According to the National Resources Defence Council (NRDC) [2], urban growth will continue to rise between now and 2050. The world is facing tremendous challenges ahead with CO₂ and NO_x levels growing at a fast pace. We are exceeding and eroding the earth's carrying capacity by more than 40% each year. A 2014 Environmental Protection Agency (EPA) study showed that CO₂ contributes to 81% of total Greenhouse Gas (GHG) emissions. Consequently, the personal transport industry has been recognised as an area where significant reductions in GHG emissions must be made.

Electric and hybrid electric vehicles represent some of the solutions to reduce GHG emissions. The growth of hybridisation and electrification technologies could potentially reduce pollution and comply with the worldwide regulations introduced by governments on emissions and fuel consumption. Hybrid Electric Vehicles (Hybrid Electric Vehicle (HEV)s) combine the advantages of engine-based and fully-electric vehicles, using fossil fuel and electric power sources to drive the vehicle. They are regarded as a step in the right direction towards more practical and viable emission-free vehicles [3].

Electric Vehicles (Electric Vehicle (EV)s) have been gaining more popularity in today's market, offering environmental benefits and positively impacting the energy and transportation sectors. Additionally, they reduce noise pollution and are easy to operate and maintain. Furthermore, EVs make a

significant contribution to the next-generation power grid, the 'smart grid'. All these benefits have led to manufacturers' and users' piqued interest in EVs. HEVs are often seen as a transition between Internal Combustion Engine (ICE) and fully electric vehicles. EVs can now have more than one motor, which introduces the possibility of improved range. With the engine removed in an electric vehicle, there is more space, design, and control flexibility [4].

The concept of HEV is almost as old as engine-based vehicles. Introducing HEVs into the market is seen as a considerable contribution towards raising awareness about the need for eco-friendly vehicles. However, there is an ongoing effort to push for better fuel economy from these vehicles and to make them more competitive and affordable. This could be done by improving the vehicle's aerodynamics, materials used in its construction, and powertrain efficiency. Improving the energy management strategy or the Supervisory Control System (SCS) is crucial to achieving better fuel economy, leading to a more efficient powertrain operation [5]. The SCS's critical function is to determine how the power demand is split between the multiple energy sources during the vehicle's operation.

Both HEVs and EVs are recognised as environmentally friendly modes of transportation. HEVs are capable of reducing GHG emissions, whereas EVs can completely eliminate them. Additionally, HEVs are known for producing less noise pollution than traditional vehicles, while EVs further minimise noise pollution.

1.2 Motivation and Objectives

The research community has focused more on complex control theory concepts. Due to pursuing advanced control theories, the complexity and accuracy of vehicle models have often been sacrificed. The design of the new powertrains calls for further research in this field. Several recent papers on HEVs have highlighted the need for developing control techniques to be tested on high-fidelity models [3, 6].

This first part of this thesis, **Energy management of HEVs**, aims to develop a high-fidelity parallel HEV model and implement conventional control strategies from the literature. This part also aims to develop novel control techniques for parallel HEVs, inspired by conventional strategies. Within

the category of parallel HEVs, a sub-category known as Through-The-Road (TTR) HEVs has been identified as a research gap. Hence, further research on this configuration of HEVs can help improve energy management strategies and make TTR HEVs more fuel-efficient [3].

There have been various studies conducted on the energy management of EVs with multiple energy sources, including batteries, fuel cells, ultra-capacitors, flywheels, and solar panels. However, to date, no academic literature has explored the use of dual-motor electric vehicles with non-identical motors, and the effect of temperature on the efficiency of traction motors and its impact on the energy management strategy.

The second part of the thesis, **Energy management of EVs**, involves the development of a backward-facing dual-motor EV, as well as the implementation of two energy management strategies utilising the DP method. The first DP problem assumes a constant motor temperature, whereas the second DP problem utilises the Lumped Parameter Thermal Network (LPTN) method to estimate the temperature of the Permanent Magnet Synchronous Motors (PMSMs). This investigation examines how the estimation and monitoring of motor temperature impact the energy management strategy.

The primary objectives of this study are listed below:

- To develop and employ a high-fidelity forward-facing parallel HEV model, based on the series HEV model developed in [6], suitable for testing control strategies
- To study and learn from the standard control techniques for both HEVs and EVs in the literature
- To apply conventional control strategies to the developed TTR HEV model
- To utilise the insights gained by the implemented conventional control strategies to develop novel heuristic strategies for parallel TTR HEVs
- To develop a backward-facing dual-motor electric vehicle model
- To explore the various thermal modelling techniques of the drivetrain components documented in the literature
- To model the thermal dynamics of the electric motors, estimating the temperature at various heat nodes

- To apply the conventional DP control strategy to the developed dual-motor EV model
- To develop a novel energy management strategy using DP, enhancing the overall efficiency and fuel economy of the developed dual-motor EV by incorporating the estimated motor temperatures

1.3 Contributions

The main contributions of this thesis are as follows:

- The design and implementation of the heuristic methods for a parallel HEV based on the efficiency maps of the powertrain components and inspired by the conventional methods used in the literature
- The development of real-time heuristic methods for the energy management of HEVs, suitable for industrial applications
- The development of a novel Driving Pattern Recognition (DPR) algorithm to be used in the framework of real-time energy management strategies
- The modelling of electric motor thermal dynamics to estimate the temperature of the primary heat paths of the traction motors in the dual-motor EV powertrains
- The design and implementation of a DP optimisation strategy for the energy management of dual-motor EVs, considering the temperature of both motors, which provides new insights into the optimal operation of such powertrains

1.4 Outline

In **Chapter 2**, a literature review of HEVs and EVs is presented. The chapter covers a brief history of HEVs and EVs, HEV and EV architectures, as well as their respective advantages and disadvantages. Furthermore, the chapter reviews vehicle modelling topology, including forward-facing and

backward-facing modelling techniques. Finally, the chapter provides an overview of HEV and EV control strategies, including optimisation-based, rule-based, and real-time control strategies, as well as thermal modelling of electric motors, which includes Finite Element Method (FEM), Rotor Flux-based Estimation, Rotor High-frequency Impedance-based Estimation, and Lumped Thermal Network (LPTN) strategies. The software used in this work for modelling and optimisation is MATLAB, and Simulink [7].

Chapter 3 describes the forward-facing modelling of a high-fidelity parallel TTR HEV, which is then implemented into Simulink. The modelling of the powertrain components and the driver model is explained with an emphasis on the primary source, secondary source and system integration. This chapter mainly focuses on the significant changes and updates from the original series HEV model in [6].

Chapter 4 introduces the optimisation-based strategy, Equivalent Consumption Minimisation Strategy (ECMS), through a brief literature review. This is followed by the implementation and tuning of the ECMS on the developed TTR vehicle model.

In **Chapter 5**, a family of heuristic methods inspired by ECMS have been developed with the aim of maximising powertrain efficiency and improving fuel economy. The first method presented in this chapter is called the Torque-levelling Threshold-changing Strategy (TTS). The chapter goes on to discuss the design principles, tuning, and implementation of the TTS in Simulink, based on the analysis conducted on powertrain efficiency and insights gained from the ECMS. In addition, the chapter also introduces the Simplified Torque-levelling Threshold-changing Strategy (STTS). Finally, two novel real-time controllers, the Real-time Torque-levelling Threshold-changing Strategy (RTTS) and the Real-time Simplified Torque-levelling Threshold-changing Strategy (RSTTS) are developed.

In **Chapter 6**, the simulation results for both conventional and heuristic HEV energy management strategies, as well as the utilised driving cycles, are presented. The TTS and STTS show impressive performance and outperform the ECMS. Furthermore, the RTTS and RSTTS perform better than the ECMS in most cases. The proposed novel real-time control strategies are found to be better suited for real-driving scenarios.

The forward-facing modelling of dual-motor EVs is explained in **Chapter 7**. Two traction motors propel this electric vehicle - one at the front and one at the rear axle. The modelling of the powertrain components and their efficiencies are presented.

In **Chapter 8**, two DP energy management strategies are explained and implemented for the dual-motor electric vehicle. DP is used to solve the optimal energy management strategy problem. The first DP is the standard method found in the literature with one state, which is the State of Charge (SOC). The second DP considers the traction motors' temperature variation and has three states: SOC and the stator windings' temperatures of both front and rear motors. The chapter also models the thermal dynamics of the traction motors in this EV using the LPTN method, which is then validated against experimental data provided by the industrial partner.

Chapter 8 also presents the simulation results for the energy management of EVs. The optimal torque split between the two traction motors acquired in the first DP with one state is fed as input into the DP framework, which considers the temperature and efficiency variations of the electric motors. This is referred to as the 'Baseline DP' case study. Next, the optimal torque split is determined with knowledge of the stator windings' temperatures of both front and rear motors and their impacts on the PMSM efficiency and optimal energy management solution. This case study is referred to as the 'Thermal DP'. The cost functions are defined to achieve the optimal energy distribution between the two traction motors in the Baseline and Thermal DP case studies for a given driving cycle. Finally, the Thermal DP is compared to the Baseline DP for the same driving cycle.

The last part of this thesis, **Chapter 9**, provides a summary of the achievements and outlines future work.

Chapter 2

Literature Review

2.1 Brief History

As climate change and energy concerns become more apparent, conventional fossil fuel-based vehicles are being replaced by greener alternatives such as electric and hybrid vehicles. It is expected that this alternative mode of transport will soon replace traditional vehicles, given current market trends [8]. In response, many automotive companies are developing low-carbon vehicles such as hybrids and electric vehicles [4]. Some legislation has incentivised automotive companies and vehicle users to opt for fuel-efficient options. For instance, in 2021, the UK government introduced a ban on selling new petrol and diesel cars by 2030. This measure could make the UK the fastest G7 country to decarbonise vehicles [9].

Besides the ban, the UK government has implemented additional measures to promote the adoption of Electric Vehicles (EVs). As of June 2022, new homes with associated parking must have an EV charging point, according to the government's new EV charging requirements [10]. Furthermore, the government has been offering a 25% subsidy on the purchase price of ultra-low emission cars since early 2012 and has introduced tax breaks in favour of these vehicles. These initiatives are aimed at incentivising consumers to choose eco-friendly alternatives and expedite the shift towards more sustainable modes of transportation.

The first experimental EV prototypes were built just after the discovery of electromagnetism in 1820 [11]. EVs were initially introduced as a solution in 1881, shortly after the invention of electric motors and rechargeable batteries [12]. By 1897, EVs had taken over 28% of the market and were preferred over ICE vehicles [13]. However, their reliance on bulky battery packs and limited driving range hindered their widespread adoption [14]. As oil prices decreased and ICE vehicles became more advanced, they gained more popularity and ultimately dominated the market.

HEVs were then introduced as an interim solution to EVs while technological advancements were made in the energy sector. HEVs are often seen as a bridge between conventional cars and EVs, with EVs being the ultimate goal. With ongoing technological advances aimed at making batteries more powerful, governments' pro-EV agendas, and the improvement of charging infrastructure, HEVs are certainly a step in the right direction towards achieving emission-free vehicles [15].

In the early days of automotive transport, HEVs were primarily developed as a solution to address the issues of EVs. The first hybrid vehicles were built by Pieper establishments in Belgium and Vendovelli and Priestly Electric Carriage company in 1899 [16]. The former had a parallel architecture, while the latter was a tricycle with a series architecture. In 1903, the Austrian company Jacob Lohner & Co. developed one of the first series hybrids, the Lohner-Porsche vehicle [17]. In this design, dynamic braking was used, in which one of the traction motors' armatures was short-circuited or replaced by a resistance. Different HEV architectures are further discussed in subsection 2.1.1.

While other HEVs were built from 1899 to 1914, power electronics were not incorporated into their design until the 1960s [16]. As the limited range of EVs became more apparent, HEVs gained more popularity in the 1990s. Major petrol and diesel car manufacturers built hybrid prototypes, such as the Dodge Intrepid ESX 1, 2, 3, Ford Prodigy, and GM Precept in the United States. However, none of these products made it to the production stage. In Europe, Renault developed a small parallel hybrid, and Volkswagen prototyped an HEV called Chico. The Japanese manufacturers Toyota and Honda made the most significant contribution in 1997, with the Toyota Prius, Honda Insight, and Honda Civic being among the first HEVs to tackle vehicle fuel consumption [16].

2.1.1 HEV Architectures

HEVs are categorised into four main types [1]:

1. **Series Hybrid:** The electric motor drives the vehicle. The engine-generator set either charges the battery or powers the motor while coasting.
2. **Parallel Hybrid:** The electric motor and the engine can drive the vehicle individually or simultaneously.
3. **Series-parallel Hybrid:** Combination of both series and parallel configurations.
4. **Complex Hybrid:** Complex configurations that do not fall into the above categories.

These concepts are visualised in Figure 2.1. These HEVs are further sub-categorised into three main types based on the location of the Electric Motor (EM) with respect to the transmission system:

- **Pre-transmission** (single-shaft): The EM is located between the engine and the transmission system [18].
- **Post-transmission** (double-shaft): The electric motor is coupled to the engine branch after the transmission system [19].
- **Through-The-Road** (double-drive): The engine and the EM act on two separate axles. The only mechanical link between the two prime movers is through the road [20].

2.1.2 HEV Advantages and Disadvantages

The advantages and disadvantages of HEVs are briefly described in the following section.

Advantages

- **Environmentally Friendly:** HEVs reduce fossil fuel consumption and GHG emissions compared to conventional vehicles and generally work in Charge-Sustaining (CS) mode in which the final SOC of the battery at the end of the trip is close to the initial SOC [3].

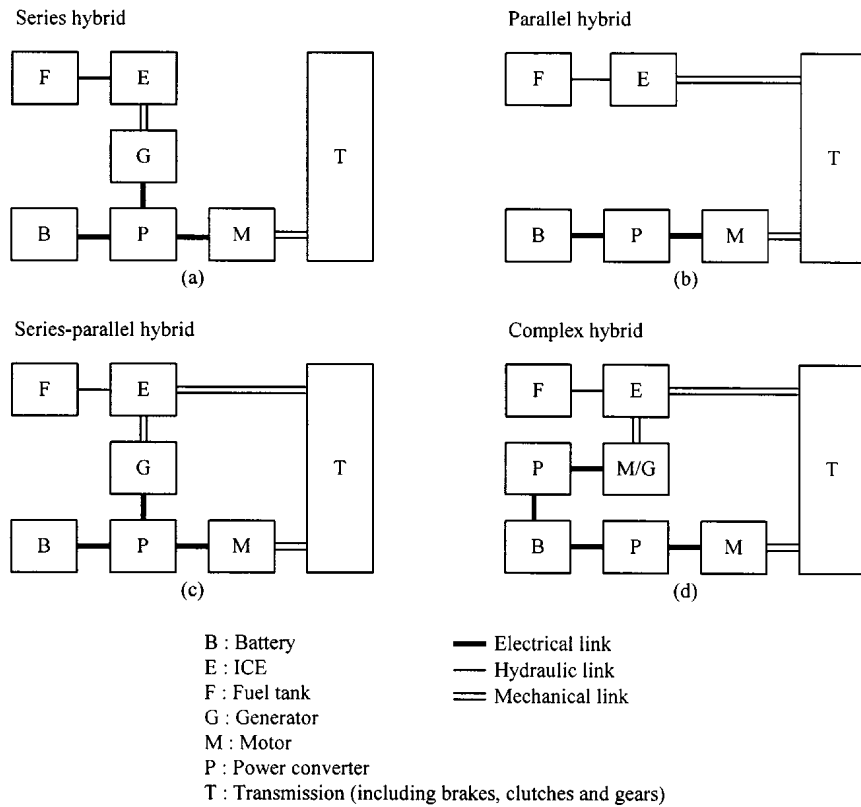


Figure 2.1: Classification of HEVs [1]

- **Financial Benefits:** Governments support green vehicles by introducing reduced tax bills and incentives to help make HEVs more affordable.
- **No Range Anxiety:** There is little to no range anxiety associated with HEVs, as the engine is present for backup once the battery is fully depleted. This means that users are not apprehensive about locating charging stations [14].

Disadvantages

- **Not Emission-free:** HEVs have a smaller carbon footprint than ICE vehicles. However, HEVs are still fossil fuel dependent.
- **Purchase Cost:** Hybrid cars are comparatively more expensive than their equivalent ICE vehicles.
- **Maintenance Cost:** The complex nature of HEVs and their dependency on skilled mechanics for repairs lead to high maintenance costs [3].

- **Poorer Handling:** A typical HEV powertrain comprises a relatively lighter engine (compared to a conventional car) and a powerful battery pack. Extra weight could lead to fuel inefficiency. Hence, manufacturers try to reduce the weight of components such as EMs and batteries, leading to less support in the chassis and suspension system [14].

Parallel HEV Advantages and Disadvantages

Since the HEV under investigation in **Part Energy Management of HEVs** is a parallel HEV, the advantages and disadvantages of such HEVs are briefly described in this section.

Advantages

- Energy loss caused by the indirect connection of the engine to the wheels is eliminated (i.e. no energy form conversion) [21].
- Additional degree of freedom in direct torque supply to the wheels; this power-sharing can optimise the power split between the electric and fuel paths. [22].
- As the powertrain does not comprise a generator, the engine and the EM can be sized for a fraction of the maximum power. This results in compactness [21].

Disadvantages

- A clutch or some other mechanical coupling between the engine and the wheels is required [22].
- The complexity of this configuration results in a more challenging control problem. [21].

2.1.3 EV Architectures

Unlike ICE vehicles, EVs provide more design flexibility. Due to this flexibility, various EV configurations have emerged, briefly explained in the following section.

Single EM

- **Conventional ICE Vehicle Converted Electric**

The earliest EV type was converted from ICE vehicles [23]. An EM and battery pack replaced the engine and the fuel tank. The transmission components used were the same as the ones in an ICE vehicle, such as clutch, multi-ratio gearbox, and differential [4]. This configuration was initially designed to be effective for an ICE vehicle; therefore, it did not achieve excellent efficiency once converted to an EV as it involved unnecessary excess mass [24].

- **Single EM with Final Drive**

Electric motors are generally more efficient than engines and have near-maximum torque at various speeds. The torque is reduced once the electric motor is operated above base speed due to field-weakening. This is because the induced voltage almost equals the maximum source voltage. For the induced voltage to be kept constant whilst the speed is increased, a negative d-current is injected, producing a magnetic flux in the opposite direction to the permanent magnet flux present [25]. Due to these specific characteristics of an EM, a multi-speed transmission is unnecessary, so the clutch and the complexity associated with such a transmission can be omitted. A single high-torque low-speed motor can be used along with a single-speed gearbox [26–28]. This configuration of EV is one of the most dominant types in the EV market [4]. However, without a variable gearbox ratio, the motor can not be operated in a near-optimal region with its maximum efficiency [29].

Multiple EMs

- **Double EMs with Double-axle Drive**

Each axle can be driven by an independent electric motor and gearbox. An appropriate power split strategy must be chosen when traction is performed using two energy sources. This introduces extra control and design flexibility. One vehicle that uses this configuration is Tesla Model X [30], with separate front and rear electric motors, each coupled with fixed-ratio gearboxes.

- **Multiple EMs with Independently-driven Wheels**

There is a possibility to eliminate differentials by incorporating separate electric motors to drive left and right wheels on the same axle. This creates extra space in the chassis. Therefore, a larger, more powerful battery can be used, resulting in a better driving range [31]. Furthermore, with increased freedom, there is more room to implement energy management strategies to operate these motors efficiently. This leads to increased overall efficiency and decreased energy consumption [29]. However, an electronic differential is needed to control the torque between the right and left wheels, which, if not done correctly, can lead to vehicle instability [27]. The cost of two small motors, the control units, and the power electronics are more expensive than a single traction motor with the equivalent power rating and the hardware associated with it [24, 27].

- **In-wheel Motor Drive**

It is possible to integrate the motor into the wheel [32]. There are still not many passenger cars in the market that utilise this approach. They are, however, predominantly used in mobile robotics [29, 33]. The main advantage of this method is the elimination of all the mechanical gears and the losses associated with these parts [24]. This results in a lighter vehicle mass and more flexibility in terms of space and the sizing of components [28, 34, 35].

2.1.4 EV Advantages and Disadvantages

In this section, the benefits and shortcomings of EVs are briefly introduced.

Advantages

- **Reduced Fuel Cost and GHG Emissions**

This is one of the main attractions of EVs. There are concerns that EVs could increase GHG emissions from power plants during peak hours when fossil fuels are used to produce electricity [36]. However, taking into account other means of generating power that produce less GHG, such as renewable sources, the GHG production from power plants due to EV penetra-

tion is lower than that of equivalent power generation from ICE vehicles. The power plants also produce energy in bulk, which minimises the per unit emission. With the vast integration of renewable sources, which can be promoted and supported by EVs, the emissions from power generation and transportation, can be reduced [37]. Over the lifetime of an EV, it produces fewer emissions than a conventional vehicle [38].

- **Higher Efficiency than Conventional Vehicles**

The EV efficiency usually lies in the 70% region, whereas for ICE vehicles, the efficiency lies in the 60 to 70% range [39]. This results in lower operating costs and increased durability of EVs.

- **Positive Impacts on the Grid**

EVs facilitate the smart grid. Smart grid can make intelligent decisions based on interaction and communication with EVs [40]. Smart grids offer robust power levels and voltage stability and promote the integration of renewable energy sources. EVs also facilitate the bidirectional Vehicle to Grid (V2G) system, in which the EV can return power to the grid. By incorporating V2G, the peak power demand could be reduced to 56% [40]. This is an attractive technology as it requires little to no change of infrastructure [41]. In a V2G framework, EV fleet operators could potentially reduce operating costs by 26.5% [40].

- **Reduced Noise Pollution**

EVs produce less noise, which is an attractive characteristic, especially in urban areas.

Disadvantages

- **Limited Battery Capacity**

One of the main barriers to wide-scale EV adoption is the limited battery capacity [42]. The range depends on factors beyond the battery's capacity, such as driving style, vehicle speed, and the use of auxiliary functions like air conditioning. This can cause range anxiety, particularly for long-distance travel [43]. In other words, the user is concerned about finding a charging point before the battery is fully depleted [44]. Tesla Model S 100D has a range of approximately 564 km with the air conditioning not in use [30], and the Chevrolet Bolt's range is approximately

383 km [45]. Although these cars can travel similar distances to ICE vehicles on a full tank of fuel, range anxiety remains one of the barriers to entering the EV market. However, most EVs' range can easily support everyday urban use. [46] reports that the daily driving mileage in the US is less than 100 miles and even lower in the UK according to UK's Department for Transport [47].

- **Grid Dependency**

EVs need electricity to charge up; this could stress the grid, especially in power-shortage regions. Charging many EVs during peak time could lead to a considerable increase in electricity demand, causing a significant grid overload and potential power cuts [48].

- **Social Acceptance**

The adoption of EVs, like any new technology, requires changes in certain habits related to refueling and driving that can be challenging for some users [49].

- **Long Charging Time**

This is another drawback of EVs. Charging times can take several hours, depending on the battery type, voltage level, and connector type. On the contrary, with ICE vehicles, loading the tank with fuel takes minutes. According to a study, some EV users are willing to pay extra to reduce charging times by an hour, ranging from \$425-\$3250 depending on the user [50].

- **Under-developed Charging Infrastructure**

Even though there has been a surge in the number of charging stations, there are still fewer than petrol stations. Furthermore, not all charging points are compatible with every car, making this issue even more pronounced. Some car manufacturers such as Tesla and Nissan are developing their bespoke charging stations [8].

- **High Purchase Price**

EVs are often more expensive than their equivalent ICE vehicles. This is due to the high cost of battery packs [44]. However, EVs benefit from lower operating costs compared to conventional vehicles. Furthermore, some governments, such as the UK and Germany, have lowered tax, insurance and parking fees for EVs to encourage people to replace conventional cars with EVs.

With the rapid pace of technological advances and mass production, EV prices will eventually decrease [8].

2.2 Vehicle Modelling Topology

There are two main approaches to modelling vehicles: 'Forward-facing' and 'Backward-facing'.

2.2.1 Forward-facing

Forward-facing models take motions as inputs instead of net forces. These models have high fidelity and follow a specific drive cycle. It is essential to include a driver model to realistically represent a human driver controlling the vehicle, which often takes the form of a Proportional-Integral (PI) controller in its simplest form. Inevitably, an error between the drive cycle speed trace and the vehicle speed will occur, and the driver's controller tries to minimise this error. This approach to modelling tests the limits of the physical system and provides insights into the vehicle's driveability. Forward-facing simulations are realistic but slow in execution [4]. A forward-facing approach has been incorporated in this work to model an HEV in Chapter 3.

2.2.2 Backward-facing

In the backward-facing modelling approach, it is assumed that the vehicle follows a specific drive cycle [51]. Both speed and torque are imposed onto the powertrain components, and the law of conservation of energy is applied from one component to the next. The traction forces are calculated from the known vehicle speed and acceleration. These forces are then converted to wheel torque and angular speed and transferred to the respective energy sources via the transmission systems. The appropriate losses in the power flow are introduced in the form of fixed efficiencies or quasi-static n-dimensional efficiency maps. According to [52], a backward-facing model can be considered non-causal. The backward-facing modelling approach does not represent the dynamic behaviour of the

components (e.g. the use of steady-state maps for the electric maps); this is the main disadvantage compared to the forward-facing approach. However, the simulations require less computational effort than those of forward-facing models [53]. These models are often used along with optimal control tools to set a benchmark. Two backward-facing vehicle models are introduced in Chapter 7. The first model computes the PMSM efficiency based on motor angular speed and torque, whereas the second model computes the efficiency based on motor temperature, angular speed, and torque.

2.3 HEV and EV Control Strategies

Over the past two decades, various supervisory control strategies have been developed for hybrid and electric vehicles. This section briefly introduces the main control strategies used in the field.

2.3.1 Optimisation-based Strategies

Optimisation-based control methods determine the optimal power split ratio among multiple energy sources by solving a complex optimisation problem. These optimisation-based methods can either be static [54, 55] or dynamic [56–58]. In dynamic optimisation, the computational object is a finite time horizon instead of instantaneous. DP is a commonly used optimisation-based control strategy in which a cost function is minimised over a drive cycle [59]. The dynamic optimisation approach relies on an analytical or numerical vehicle model [16]. The optimal solution in the DP approach is a global one. However, as this method inspects all possible solutions to find the global solution, it is computationally intensive and poorly suited for real-time applications nor high-fidelity complex vehicle models [16]. Even though this method can not be implemented in real-time, it can help modify the existing rule-based strategies or inspire new methods [60]. This method is discussed in greater detail in Chapter 7. Pontrygain's Minimum Principle (PMP) is another popular optimisation-based method which can find the optimal control strategy by minimising the Hamiltonian function [61]. However, this is a necessary but not sufficient condition to achieve a globally optimal solution. PMP can not be applied directly as the co-states in the function need to be determined by iteratively trying [62].

Model Predictive Control (MPC) is another optimal control method in which a speed or torque predictor is used to predict a finite horizon vehicle speed or torque requirement [60]. Neural Network (NN) models could implement the information found through prediction [63], torque requirement exponentially decreasing models [64], or Markov-chain (MC) [65]. The information gathered via the prediction model is then used to design the control strategy using an optimal control algorithm such as DP [66], nonlinear programming [67], or quadratic programming algorithm [68].

The Equivalent Consumption Minimisation Strategy (ECMS) is one of the most commonly used optimisation-based strategies for benchmarking. The power split between the energy sources is optimised every instant for a specific driving cycle [69]. This strategy is discussed in greater detail in Chapter 4. The ECMS is the most promising optimisation-based approach, preferred by automotive manufacturers, as the cost function depends on the current system variables without relying on prediction. According to [70], the fuel economy for the optimal DP solution and the sub-optimal ECMS solution is very similar. The ECMS has a reasonable definition for the equivalence factors and is the best benchmarking tool for high-fidelity models. However, determining the equivalence factors is not trivial [70, 71]. DP has not been pursued in the first part of this thesis, as the HEV model under evaluation is a high-fidelity model; therefore, it is infeasible to perform DP on such a complex model due to its high computational load.

The control solutions' optimal nature is very attractive, but these strategies are time-consuming and computationally expensive, and the required apriori knowledge of the driving cycle is impractical. Therefore, they are mainly used for benchmarking and evaluating the controllers' optimality [5].

2.3.2 Rule-based Strategies

Rule-based control systems could be developed based on human expertise, intuition, heuristics, driving cycles and mathematical models.

Rule-based strategies can be sub-categorised into fuzzy-based strategies and deterministic methods. In the framework of HEVs, the former method is used to minimise the fuel economy and to ensure the SOC of the battery is sustained within a specific range whilst meeting the driver's torque request [59].

Unlike fuzzy-based strategies, deterministic methods usually use look-up tables, which are not real-time data. In deterministic methods, real-time parameters are used, and linguistic languages describe the input variables as 'High', 'Medium' and 'Low'. This method requires real-time operations to obtain the knowledge and experience to tune the controller; this can be time-consuming and costly [16].

In the load-following principle, the fuel energy source is used to 'follow' the load power, whereas the electric branch is ideally used at zero power levels. In the SCS design for series HEVs, the concept of power-following is used in the Power Follower Control Strategy (PFCS) [59], and the Exclusive Operation Strategy (XOS) [6], which incorporates a power-following behaviour inspired by PFCS. In the SCS design for parallel HEVs, The Electric Assist Control Strategy (EACS) is used in [72], based on the power-following principle. This method is utilised in commercial HEVs such as Toyota Prius and Honda Insight [73]. However, its design process is time-consuming. The main drawback of the load-following principle is that the Charge-Sustaining (CS) operation in which $SOC_{final} \approx SOC_{init}$ is dependent on the regenerative braking mechanism; therefore, the CS operation can not be achieved for all driving cycles as some have limited amount of regenerative braking.

In the load-levelling approach, the fuel energy source is operated steadily while the electric energy source acts as a buffer and is used to 'level' the load [74]. Thermostat Control Strategy (TCS) and Optimal Primary Source Strategy (OPSS) are amongst the strategies which are based on the load-levelling principle [6]. TCS and other load-levelling methods usually apply to series HEVs, where there is no direct mechanical connection between the engine and the wheels. Thus, the engine-generator set can be operated more steadily [16]. Load-levelling is discussed in Chapter 5.

Amongst various heuristic methods, NN can be pointed out [75, 76]. Even though the simulations indicate that this method can improve fuel economy, the lack of experiments makes the results less persuasive.

Heuristic methods are easily implementable, but there is no guarantee of efficiency and robustness as it is based on engineering experience.

2.3.3 Real-time Control Strategies

The global optimisation methods are not directly suitable for real-world applications as they are causal solutions. Real-time energy management must be simple enough to avoid high computational load and keep the memory resources low so that it can be executed in real time. Several attempts have been made to develop real-time control strategies for HEVs; the strategies in [69, 72, 77, 78] are based on instantaneous optimisation. The cost functions in these optimisation-based real-time control strategies are only based on the system's current control variables rather than apriori knowledge of the driving conditions.

The general approach to designing real-time controllers is summarised in the following design steps [79]:

- Solve the offline optimisation-based optimal control problem globally to be used as a benchmark and to extract some simple rules for the real-time controller.
- Make the controller causal by solving the optimal control problem to predict future driving conditions. The prediction horizon must be selected as a trade-off between the prediction accuracy and the time scale of the dynamics of the model.
- Make the controller more robust against modelling and prediction uncertainties, for instance, by introducing penalty functions, rule functions, or feedback control systems.

The real-time controllers introduced in this work are inspired by the heuristic methods introduced in Chapter 5 and are discussed in detail in section 5.3.

Driving Pattern Recognition (DPR) is one of the most widely used approaches in real-time strategies [80]. DPR contains a set of strategies designed for specific situations, such as different driving styles or traffic conditions. However, the occasional wrong classification of driving patterns impacts the performance even though DPR promotes robustness. In [81], a learning vector quantisation-based DPR module was suggested. In the literature, the load-following and load-levelling approaches have been extensively employed in rule-based SCSs for HEVs [6, 16, 59, 72, 74, 82]. A novel DPR algorithm is developed in this work and presented in section 5.3.

2.4 Thermal Modelling of Electric Motors

Permanent Magnet Synchronous Motors (PMSMs) are widely used in the automotive and HEV/EV sectors. PMSMs have high efficiency, power density and reliable performance [83–85]. Monitoring the critical temperatures of electric machines is crucial as there can be risks of demagnetisation and inefficient operation of the motors [86, 87]. A few methods in the literature to model electric machines' thermal dynamics are briefly described in this section.

2.4.1 Finite Element Method (FEM)

In FEM, multi-physics coupling is used to simulate the electromagnetic and temperature field of the motor [88, 89]. This method has high estimation accuracy but depends on factors such as motor geometry, boundary conditions, and material properties, leading to computationally heavy and complex solutions. Furthermore, due to the complex nature of this solution, it can only be used offline for analysis purposes.

2.4.2 Rotor Flux-based Estimation

In [90], a method based on rotor flux has been proposed. Although this method is simple and easy to conduct, unlike FEM, it can only predict the rotor temperature. Moreover, the estimation accuracy depends on the observation accuracy of the rotor flux linkage; the relationship between flux linkage and temperature is not always linear.

2.4.3 Rotor High-frequency Impedance Based Estimation

Compared to the rotor flux-based method, this estimation method has the advantage of being able to capture the transient impedance change in the rotor. However, the injection of high-frequency signals may lead to additional rotor losses, which could result in a significant temperature increase. Some examples can be found in [91–93].

2.4.4 Lumped Parameter Thermal Networks (LPTNs)

LPTN is a simplified alternative to monitor the motor temperature. This method is based on the simplified physical motor model and its structure; LPTN can estimate the motor temperature online [94, 95]. Three LPTN-based methods are mainly characterised by the number of thermal nodes.

Dark Grey-box LPTN

This method usually comprises two to five nodes representing the most dominant heat paths in the motor; these LPTNs do not involve complicated motor thermal structures. The thermal parameters are identified based on experimental data obtained from sensors [96–102].

Light Grey-box LPTN

Compared to the previous method, light grey-box LPTN involves more thermal nodes (five to fifteen nodes), and more heat paths in the motor are considered to design the LPTN based on heat transfer theory [103, 104]. The dependency of this LPTN method on the geometrical characteristics and the material of the motor are the main drawbacks.

White-box LPTN

This method involves more nodes than the Light Grey-box and accurately represents the thermal dynamics; however, the significant number of nodes leads to high computational cost [105, 106].

Comparison of LPTN Methods

In most EV and HEV applications, the Dark Grey-box LPTN method is used due to its lack of dependency on the motors' full material and geometric characteristics. Furthermore, its easy implementation and low computational cost make it suitable for real-time applications. Some EV application

examples can be found in [96, 98, 99, 107]. The Dark Grey-box LPTN method is used in subsection 8.3.1 to estimate the temperature of the PMSM motor, which is then used as a state in an optimal control framework in Chapter 8. The simplified nature of this method makes it suitable for optimal control problems. Light Grey-box and White-box LPTNs are based on the heat transfer theory [108]. There is no guarantee of high accuracy with these methods as they strongly depend on the motor geometry and heat transfer characteristics of the motor material. Moreover, due to their complex nature, they are unsuitable for real-time temperature estimation.

Part II

Energy Management of HEVs

Chapter 3

Hybrid Electric Vehicle Model

3.1 Background

The vehicle model considered in the present work is a parallel TTR HEV with two different propulsion systems acting on separate axles. The powertrain architecture of the TTR HEV is presented in Figure 3.1. The engine branch (primary power source) drives the front axle. The battery branch (secondary power source) includes a battery, DC-DC converter, DC link, DC/AC inverter, PMSM and a fixed gear transmission connected to the rear axle. Figure 3.2 shows a block diagram with detailed interconnections of powertrain components and the Supervisory Control System (SCS). In the first section of the work, the powertrain components used are the same as those in the series HEV model developed in [6] and [109]. This section describes the TTR HEV powertrain model, with the modelling of each powertrain component and its integration.

3.2 Primary Source

In this section, two engine models are presented. Model Alpha in section 3.2.1 represents a high-fidelity 2.0L diesel engine. Model Beta in section 3.2.1 represents a 2.0L petrol engine.

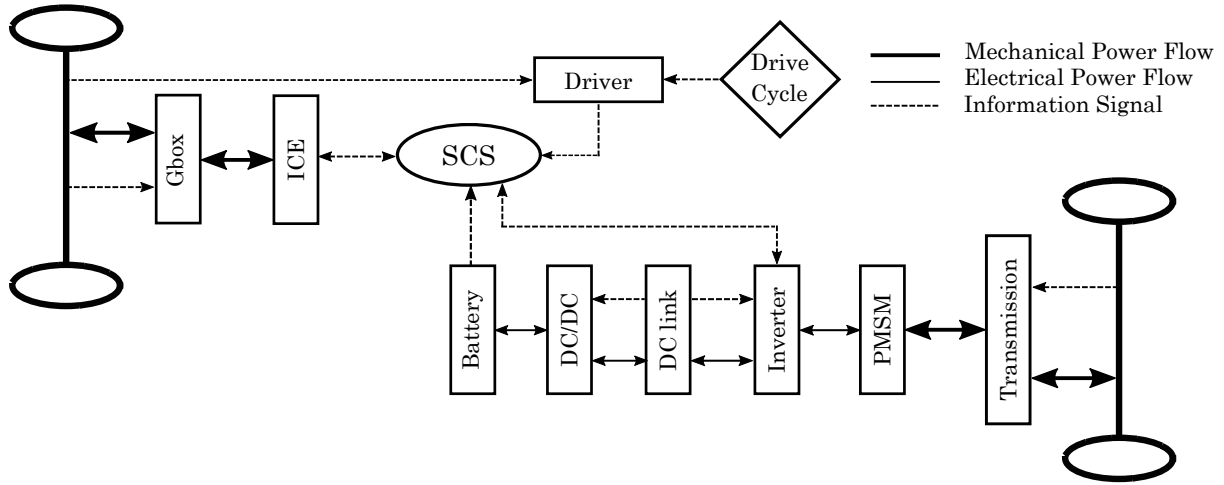


Figure 3.1: The overall architecture of the TTR HEV.

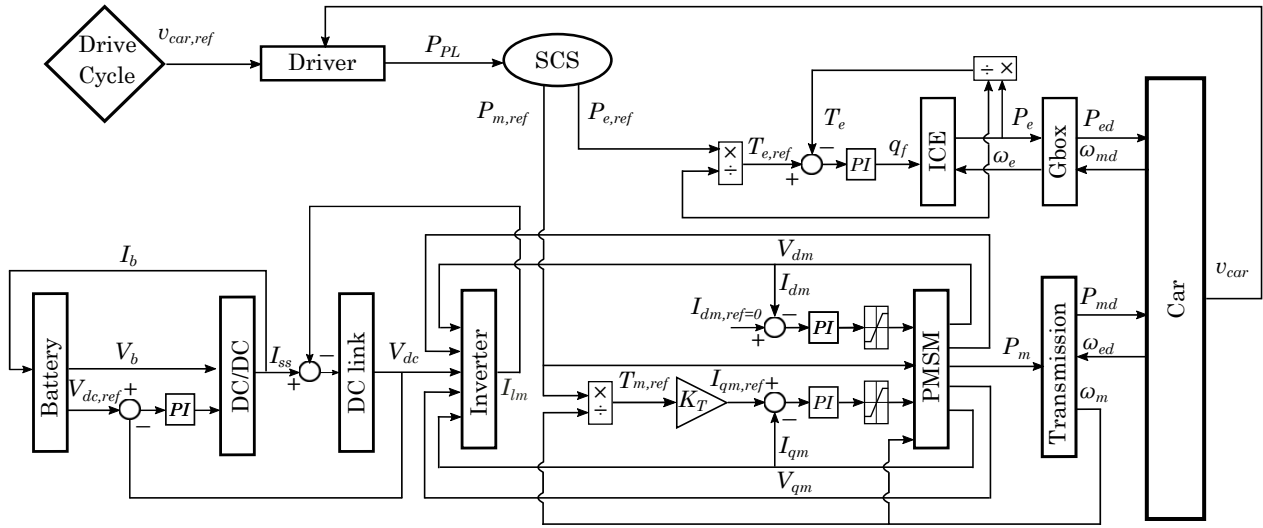


Figure 3.2: Block diagram showing the interconnection of the Battery, DC-DC converter, DC link, Inverter, PMSM, Gearbox (Gbox), Rear transmission system (Transmission), ICE, SCS, Driver and Car.

3.2.1 Engine Model

Engine Model Alpha

Similarly to the engine model in [110], the present work considers a turbocharged Puma 2.0L diesel engine with the engine efficiency map $\eta_e(T_e, \omega_e)$ presented in Figure 3.3a, which is obtained from Ricardo Wave full CFD model simulation results as a function of the engine torque T_e and engine

speed ω_e [111]. The engine dynamics are as follows:

$$\frac{dm_f}{dt} = q_f(T_e, \omega_e). \quad (3.1)$$

The fuel chemical power is:

$$P_f = Q_{LHV} q_f(T_e, \omega_e) \quad (3.2)$$

where m_f and $q_f(T_e, \omega_e)$ are the engine fuel mass and fuel consumption rate, respectively. Q_{LHV} is the fuel lower heating value, which is converted into the engine mechanical power P_e :

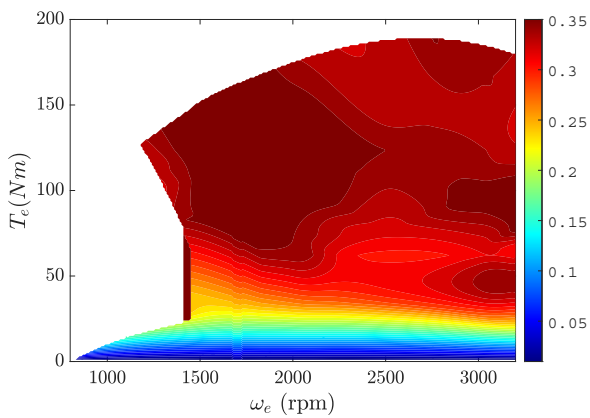
$$P_e = T_e \omega_e \quad (3.3)$$

$$P_e = \eta_e(T_e, \omega_e) P_f. \quad (3.4)$$

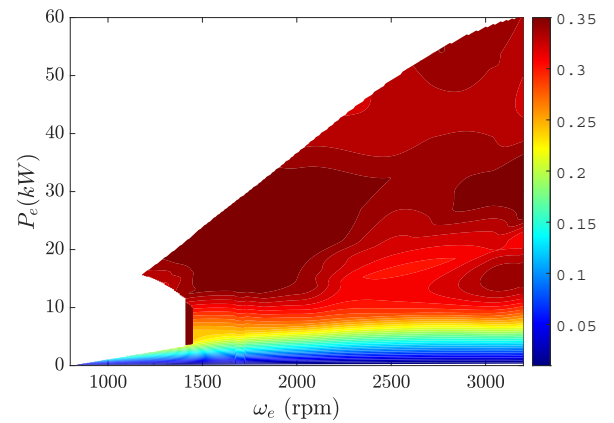
According to (3.2) and (3.4), the fuel consumption rate $q_f(T_e, \omega_e)$ is determined by

$$q_f(T_e, \omega_e) = \frac{P_e}{\eta_e(T_e, \omega_e) Q_{LHV}}. \quad (3.5)$$

The engine parameters are summarised in Table 3.1.



(a) Engine efficiency map for varying engine load torque T_e , and engine speed ω_e , for model Alpha.



(b) Engine efficiency map for varying engine load power P_e , and engine speed ω_e , for model Alpha.

Figure 3.3: Engine model Alpha efficiency maps

Table 3.1: Engine model Alpha parameters

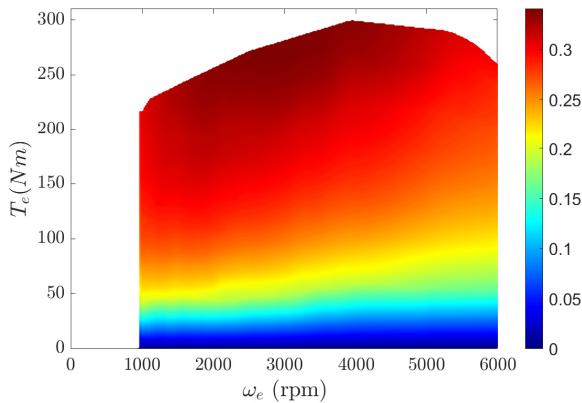
Parameter	Symbol	Value
Engine max power	$P_{e,max}$	58 kW
Lower heating value	Q_{LHV}	42.8 MJ/kg
Engine idle speed	ω_{idle}	800 rpm
Engine maximum speed	ω_{max}	3200 rpm

Engine Model Beta

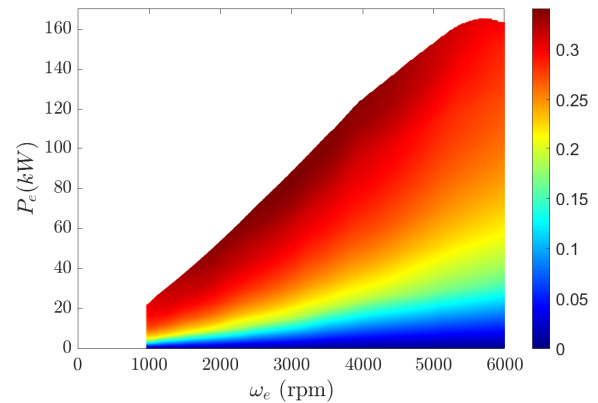
This section describes the second engine model, referred to as model Beta. The main engine parameters are listed in Table 3.2. Similarly to [112], the present work considers a 2.0L petrol engine with the efficiency map $\eta_e(T_e, \omega_e)$ presented in Figure 3.4a. Efficiency has been displayed for every engine torque T_e and engine speed ω_e operating point in Figure 3.4a, and for every engine power P_e and engine speed ω_e operating point in Figure 3.4b.

Table 3.2: Engine model Beta parameters

Parameter	Symbol	Value
Engine max power	$P_{e,max}$	120 kW
Lower heating value	Q_{LHV}	44.4 MJ/kg
Engine idle speed	ω_{idle}	1000 rpm
Engine maximum speed	ω_{max}	6000 rpm



(a) Engine efficiency map for varying engine load torque T_e , and engine speed ω_e , for model Beta.



(b) Engine efficiency map for varying engine load power P_e , and engine speed ω_e , for model Beta.

Figure 3.4: Engine model Beta efficiency maps

3.2.2 Start-Stop System (SSS)

To consider the losses associated with engine switching on/off and engine idling, a Start-Stop System (SSS) is also included in the vehicle model similar to the one used in [6]. In this work, the penalty has been defined according to the method used in [6] and in such a way that it corresponds to the fuel consumed by idling the ICE for 1 s. A penalty of 0.11 g is added to the base fuel consumption every time the engine switches on, which is captured when the ICE speed exceeds the idle speed, defined for models Alpha and Beta in Table 3.1 and Table 3.2, respectively.

3.2.3 ICE Gearbox

This vehicle model uses a 6-speed automatic gearbox to connect the ICE and the front axle. The engine speed ω_e is determined by the vehicle wheel speed ω_{wheel} , and is described as follows:

$$\omega_e = g_{ei} g_{fd} \omega_{wheel} \quad (3.6)$$

with g_{ei} being the gear ratio of the i^{th} gear and g_{fd} representing the final drive ratio. The gear ratios are specified in Table 3.3, which are changed according to the vehicle speed shown in Figure 3.5. The gearbox efficiency is assumed to be a constant value of $\eta_g=0.96$. The ICE driving power P_{ed} is described as follows:

$$P_{ed} = P_e \eta_g \quad (3.7)$$

where P_e is the ICE output power and $P_{e,d}$ is the driving power of the primary source.

Table 3.3: Gear ratio values

Gear number	Gear ratio	Vehicle velocity threshold km/h
1 st	3.20	15
2 nd	1.62	30
3 rd	1.28	52
4 th	0.91	72
5 th	0.67	100
6 th	0.53	120
Final drive ratio	4.30	-

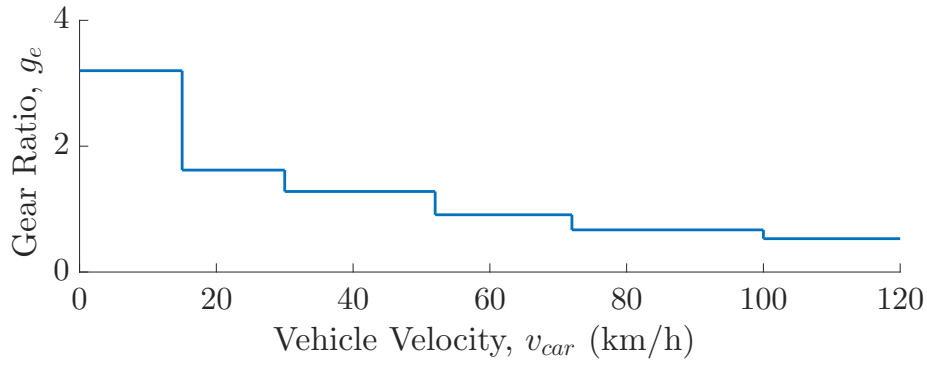


Figure 3.5: Gear ratio as a function of vehicle speed.

3.3 Secondary Source

The secondary source of this HEV is comprised of a battery, DC-DC converter, DC link, Inverter, PMSM and motor transmissions. The modelling of these components is described in this section.

3.3.1 Battery

In this HEV model, a Lithium-ion battery is used, and the battery model is built according to [113] and [114]. The battery voltage is:

$$V_b = E_b - R_b I_b \quad (3.8)$$

with I_b being the average current drawn from the battery and E_b being the open circuit voltage defined by:

$$E_b = \begin{cases} E_0 - \frac{Q_{max} K_1 Q}{Q_{max} - Q} - \frac{Q_{max} K_2 I_b^*}{Q_{max} - Q} + A \exp(-B \cdot Q), & I_b^* \geq 0 \\ E_0 - \frac{Q_{max} K_1 Q}{Q_{max} - Q} - \frac{Q_{max} K_2 I_b^*}{Q - 0.1 Q_{max}} + A \exp(-B \cdot Q), & I_b^* < 0 \end{cases} \quad (3.9)$$

where Q is the consumed charge, and i_b^* is the filtered battery current which can be expressed by:

$$I_b^* = \frac{1}{\tau_r s + 1} I_b, \quad (3.10)$$

with s being the standard Laplace variable. By defining the battery state of charge (SOC) as $SOC \triangleq 1 - Q/Q_{max}$, the battery dynamics are presented as:

$$\frac{d}{dt}(SOC) = -\frac{I_b}{Q_{max}}. \quad (3.11)$$

The battery parameters are summarised in Table 3.4.

Table 3.4: Li-on battery parameters

Parameter	Symbol	Value
Rated capacity	Q_{max}	14.4 Ah
Nominal voltage	V_{nom}	296 V
Initial state of charge	SOC_{init}	65%
Battery constant voltage	E_0	320.6795 V
Polarisation constant	K_1	0.116 V/(Ah)
Polarisation resistance	K_2	0.116 Ω
Internal resistance	R_b	0.2056 Ω
Time constant for filtered current	τ_r	10 s
Exponential zone amplitude	A	25.1477 V
Exponential zone time constant inverse	B	4.2404 (Ah) ⁻¹
Battery maximum power	$P_{b,max}$	42 kW
Battery minimum power	$P_{b,min}$	-21 kW

3.3.2 DC-DC Converter

The bidirectional DC-DC converter used in the model connects the battery to the DC link and increases the battery voltage to a higher level. The DC-DC converter dynamics have been described in [115], and its efficiency against various load powers is presented in Figure 3.6. The converter's average efficiency is approximately 96%; however, the efficiency becomes very low at low power loads and rises quickly as the load power increases. Therefore, to ensure high operation efficiency, low power loads must be avoided.

3.3.3 DC Link

The DC link comprises a capacitor $C_o=3$ mF, operated with a constant voltage $v_{dc,ref}=700$ V, using an appropriate power flow controller. The dynamics of the DC link are described as follows:

$$C_o \frac{dv_c}{dt} = I_{SS} - I_{lm} \quad (3.12)$$

where v_c is the DC link voltage, I_{SS} is the current coming from the DC-DC converter and I_{lm} is the current drawn from the inverter. In the present work, $I_{SS} < 0$ indicates a charging operation, and $I_{SS} > 0$ represents a discharging operation.

3.3.4 Inverter

The PMSM is connected to the DC link through a bi-directional inverter. The detailed model of the inverter can be found in [6]. The inverter's efficiency against various load powers is shown in Figure 3.7.

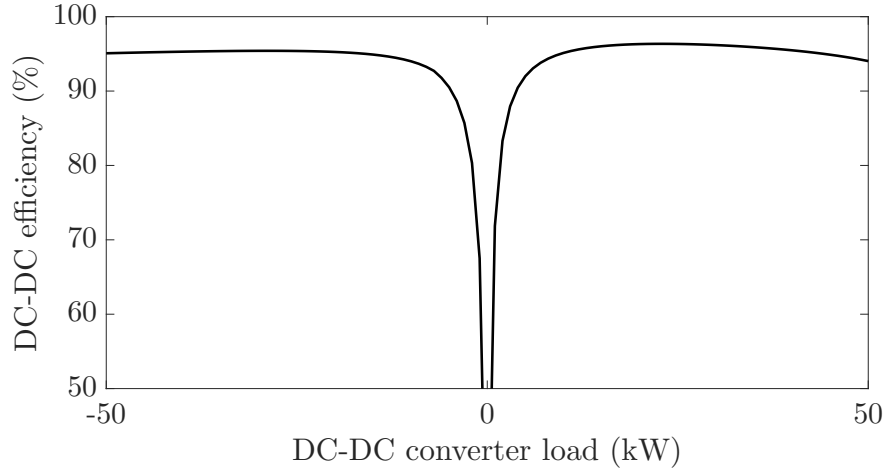


Figure 3.6: DC-DC converter efficiency for varying values of load power.

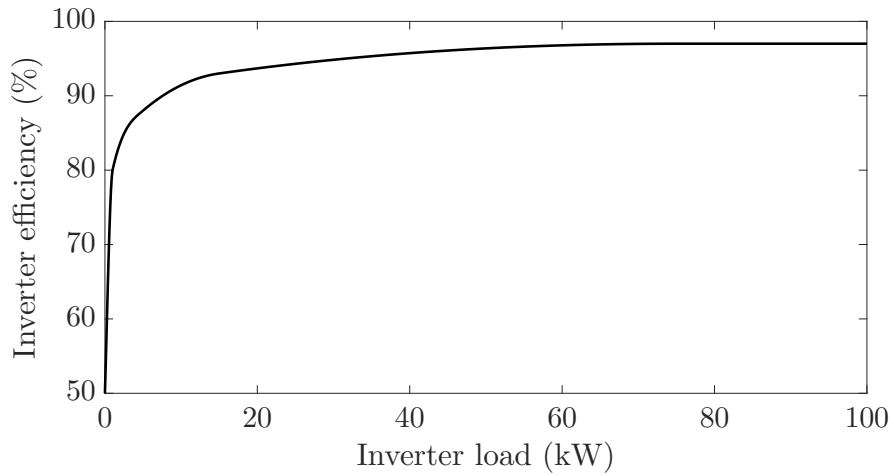


Figure 3.7: Inverter efficiency for varying values of load power.

3.3.5 Permanent Magnet Synchronous Motor (PMSM)

The PMSM model is based on the EVO Electric AFM-140 [116], and its detailed dynamics described by the standard 2-phase d-q rotating reference frame can be found in [6]. In the present work, the max-

imum speed of the PMSM is 5000 rpm, and the maximum output torque is 400 Nm. The efficiency map of the PMSM against the rotor speed ω_m and load torque T_m is shown in Figure 3.8.

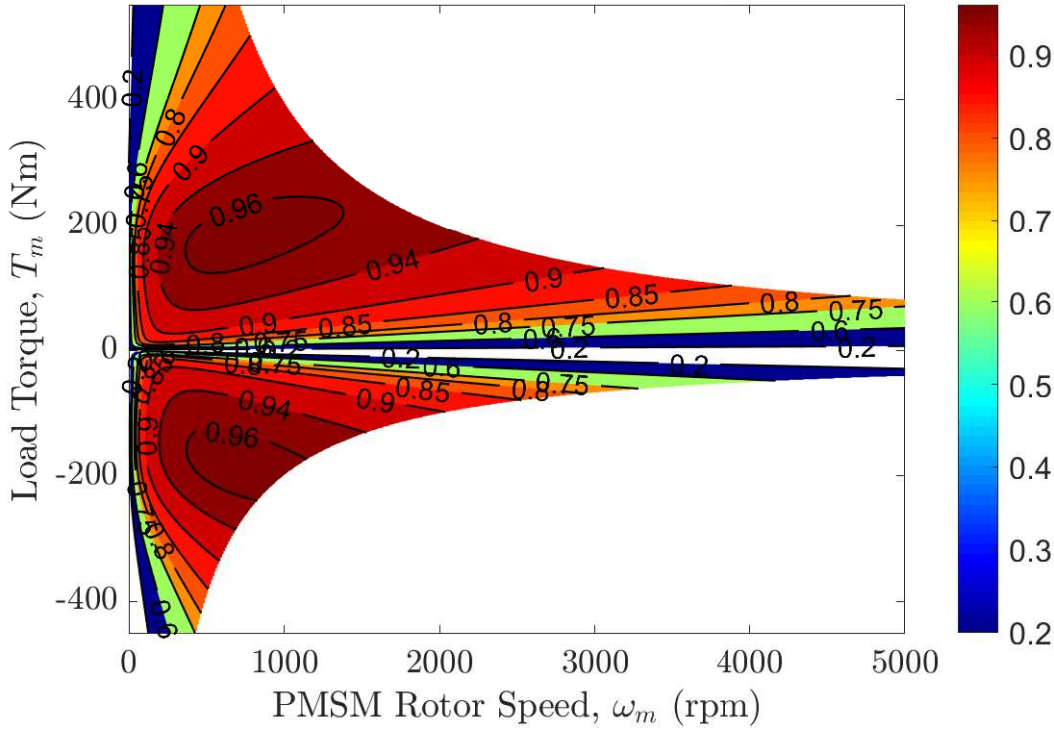


Figure 3.8: PMSM steady-state power efficiency map for variations in the load torque T_m , and rotor speed ω_m . As only forward vehicle motion is considered in this work, the rotor speed is always non-negative, and the PMSM has two modes of operation: 1) positive T_m (motoring) and 2) negative T_m (regenerating). The contours correspond to constant efficiencies in the range 75-96%.

3.3.6 PMSM Transmission

The PMSM is mechanically connected to the rear axle via a fixed-gear transmission. The motor speed ω_m , is determined by the vehicle wheel speed ω_{wheel} , and is described as follows:

$$\omega_m = g_m \omega_{wheel} \quad (3.13)$$

with $g_m=4.3$. In this HEV model, the transmission efficiency is assumed to be $\eta_t=0.96$. The following equation describes the power transmission:

$$P_{md} = P_m \eta_t^{\text{sign}(P_m)} \quad (3.14)$$

where $P_m = \omega_m T_m$ is the motor mechanical power, and P_{md} is the electrical driving power.

3.4 Driver Model

In the TTR architecture, there is no mechanical connection between the ICE and the motor. Despite both axles running at the same speed, the engine and the electric motor can provide propulsion load individually. The forward velocity of the vehicle v_{car} follows the reference velocity $v_{car,ref}$, which is given by a specific driving cycle. The mathematical form of the driver model is defined as:

$$T_{ref} = k_P(v_{car} - v_{car,ref}) + k_I \int (v_{car} - v_{car,ref}) dt \quad (3.15)$$

where $v(t) = v_{car} - v_{car,ref}$, and the PI gains are tuned by trial and error. In this work, only the longitudinal motion of the vehicle is considered; hence a PI model would suffice.

3.5 System Integration

The model used in this work captures the longitudinal vehicle dynamics and is based on the multi-body model presented in [117]. The forward and vertical translations of the main body and the pitch rotation are captured. The front wheel is connected to the engine shaft via a 6-speed automatic transmission. The rear wheel is connected to the motor shaft via a fixed-ratio gearbox. The parameters used in this model represent an average European saloon. The total mass is 1476.6 kg, the drag coefficient is 0.35, and the pitch inertia is 2152.1 kgm². The vehicle parameters and detailed multi-body dynamic model can be found in [117]. The car dynamics are implemented in Simulink using the SimMechanics toolbox.

The total propulsion load $P_{PL} = T_{ref}\omega_{wheel}$, is the sum of (3.7), and (3.14) which are the powers provided by the fuel path P_{ed} , and the electrical path P_{md} , respectively.

3.6 Chapter Summary

The modelling of the powertrain components of a high-fidelity TTR HEV model was described along with their interconnection. Emphasis was given to these components' efficiencies, performance-related core operational behaviour, and the significant changes and updates from the original series hybrid model presented in [6]. Two engine models have been introduced: Alpha and Beta. Engine model Alpha is a turbo-charged diesel engine which includes engine dynamics, whereas engine model Beta is a look-up table which evaluates fuel economy based on the engine torque demand and engine speed. The presented high-fidelity parallel TTR HEV vehicle model is used in the framework of conventional control strategies in Chapter 4 and novel heuristic methods in Chapter 5.

Chapter 4

Conventional Control Strategies for the Energy Management of HEVs

This section describes the design of the most common conventional control strategy ECMS. The SCS decides how the requested power demand for a given driving cycle is distributed between the multiple energy sources in the vehicle's powertrain. This method is implemented on the TTR vehicle model, presented in Chapter 3. The implementation of ECMS provides insights for new heuristic control strategy design, used to benchmark the developed novel heuristic strategies in section 5.1. In addition to the ECMS, a uniform evaluation rule for the fuel economy is also presented to assess different control strategies.

4.1 Design and Implementation of ECMS

As a conventional control strategy for HEVs, the ECMS has been widely studied in the literature [5, 69, 118]. The ECMS can achieve similar control performance as DP for simple vehicle models [5, 119]. The ECMS can benchmark against other energy management control strategies, especially for complex vehicle models for which the DP is unsolvable; however, ECMS may not achieve optimal global solutions.

4.1.1 Fuel Economy Evaluation

To evaluate various energy management control strategies, a uniform rule is proposed for calculating fuel economy:

$$m_{efc} = \begin{cases} m_f + S_{d,efc} \Delta SOC \frac{Q_{max} E_b}{Q_{LHV}} & \Delta SOC \geq 0 \\ m_f + S_{c,efc} \Delta SOC \frac{Q_{max} E_b}{Q_{LHV}} & \Delta SOC < 0 \end{cases}, \quad (4.1)$$

where $S_{d,efc}$ is the discharging equivalence factor, $S_{c,efc}$ is the charging equivalence factor, $\Delta SOC = SOC_{init} - SOC_{final}$, and E_b is the battery open-circuit voltage. The SCS used to derive these equivalence factors is a simple Proportional (P) control strategy according to [120], given by:

$$P_{ed,ref} = u_{efc} P_{PL} \quad (4.2)$$

where u_{efc} is a constant. A sweep is then performed for $u_{efc} \in [1 - \alpha, 1 + \alpha]$, in steps of 0.05 with $\alpha=0.5$ in this work, to obtain a wide set of power shares between the primary and secondary sources. According to the line-chart method in [120], at the end of each drive cycle, the accumulative values of the electrical energy E_e presented in Equation 4.3, and the fuel energy E_f presented in Equation 4.4, for every u_{efc} as specified in Equation 4.2 are collected and plotted against each other in Figure 4.1 and Figure 4.3, for the model Alpha and Beta, respectively. The slope of the plot for $u_{efc} \geq 1$, corresponds to the negative value of $S_{c,efc}$ and the slope of the line plotted for $u_{efc} < 1$, gives the negative value of $S_{d,efc}$. The Equivalent Fuel Consumption (EFC) factors can intuitively be regarded as the conversion factors between the fuel energy and the electrical energy for discharging (data marked as plus signs), and charging (data marked as circles), respectively.

$$E_e = \Delta SOC \ Q_{max} \quad (4.3)$$

$$E_f = m_f \ Q_{LHV} \quad (4.4)$$

The EFC equivalence factors are evaluated for every driving cycle and summarised in Table 4.1 and Table 4.2, for the model Alpha and Beta, respectively. The equivalence factors are then used to calculate the fuel economy for various energy management strategies.

Table 4.1: EFC equivalence factors for the model Alpha

Drive cycle	$S_{c,efc}$	$S_{d,efc}$
WL-L	1.4256	3.1823
WL-M	1.5176	3.1368
WL-H	1.8464	3.2806
WL-E	2.3912	3.7198

Table 4.2: EFC equivalence factors for the model Beta

Drive cycle	$S_{c,efc}$	$S_{d,efc}$
WL-L	3.3934	4.3344
WL-M	3.4386	4.0228
WL-H	3.6725	3.4379
WL-E	2.3743	3.2261

4.1.2 Equivalent Fuel Consumption Minimisation Strategy (ECMS)

This section describes the optimisation problem formulation for ECMS using the EFC equivalence factors described in subsection 4.1.1. In the ECMS, the objective is to minimise the equivalent fuel consumption m_{eq} , defined as:

$$m_{eq} = \int_0^{t_f} \dot{q}_{eq}(P_{ed}, v_{ref}, P_{md}, S_d, S_c) dt \quad (4.5)$$

with

$$\dot{q}_{eq} = \begin{cases} \dot{q}_f(P_{ed}, v_{ref}) + S_d \frac{P_{md}}{Q_{LHV}} & P_{md} \geq 0 \\ \dot{q}_f(P_{ed}, v_{ref}) + S_c \frac{P_{md}}{Q_{LHV}} & P_{md} < 0. \end{cases} \quad (4.6)$$

with \dot{q}_{eq} being the equivalent fuel consumption rate and t_f being the duration of the given drive cycle. The ECMS equivalence factors S_d and S_c are constant over each driving cycle and are used to evaluate the fuel equivalent of the positive and negative electrical energies used over the corresponding driving cycle [120]. Based on PMP, the optimisation problem can be formulated as follows:

$$\min_{\mathbf{u}} \quad \dot{q}_{eq}(P_{ed}, v_{ref}, P_{md}, S_d, S_c) \quad (4.7a)$$

$$\text{subject to : } P_{PL} = P_{ed} + P_{md} \quad (4.7b)$$

$$0 \leq P_{ed} \leq P_{edmax} \quad (4.7c)$$

$$P_{mdmin} \leq P_{md} \leq P_{mdmax} \quad (4.7d)$$

$$SOC_L \leq SOC \leq SOC_U \quad (4.7e)$$

$$q_f(0) = 0, SOC(0) = 0.65 \quad (4.7f)$$

where P_{edmax} denotes the maximum power of the primary source, P_{mdmin} and P_{mdmax} represent the minimum and maximum power of the secondary source, respectively. These values can be calculated from P_{emax} , P_{bmin} and P_{bmax} .

Thus, for each time instant t , a given driving cycle with the speed v_{ref} , propulsion load $P_{PL} = P_{ed} + P_{md}$, and the engine angular speed ω_e , an optimal power share factor solution of $u_{sf} \triangleq P_{ed}/P_{PL}$ is determined for each pair of equivalence factors S_d and S_c . To select an optimal (S_d, S_c) , the optimisation problem is repeated for various (S_d, S_c) pairs. A sweep is performed in steps of 0.1 for S_d and S_c . As the HEV model is complex, the regions where the sweep for S_d and S_c take place must be limited and well-defined. The derived EFC equivalence factors presented in Table 4.1, and Table 4.2 can be used as a guideline to appropriately select the sweep intervals for S_d and S_c ; otherwise, the computational time of this method would be too long. This means that the solution achieved by ECMS is not globally optimal. The optimal (S_d, S_c) pair is the one that minimises the equivalent fuel consumption m_{efc} . The optimal control maps for four standard drive cycles are shown in Figure 4.2 and Figure 4.4, and the corresponding optimal equivalence factors are summarised in Table 4.3 and Table 4.4 for the model Alpha and Beta, respectively.

Table 4.3: Optimal ECMS equivalence factors for the model Alpha

Driving cycle	S_c	S_d
WL-L	1.8	4.1
WL-M	1.4	3.7
WL-H	1.6	3.7
WL-E	2.4	3.4

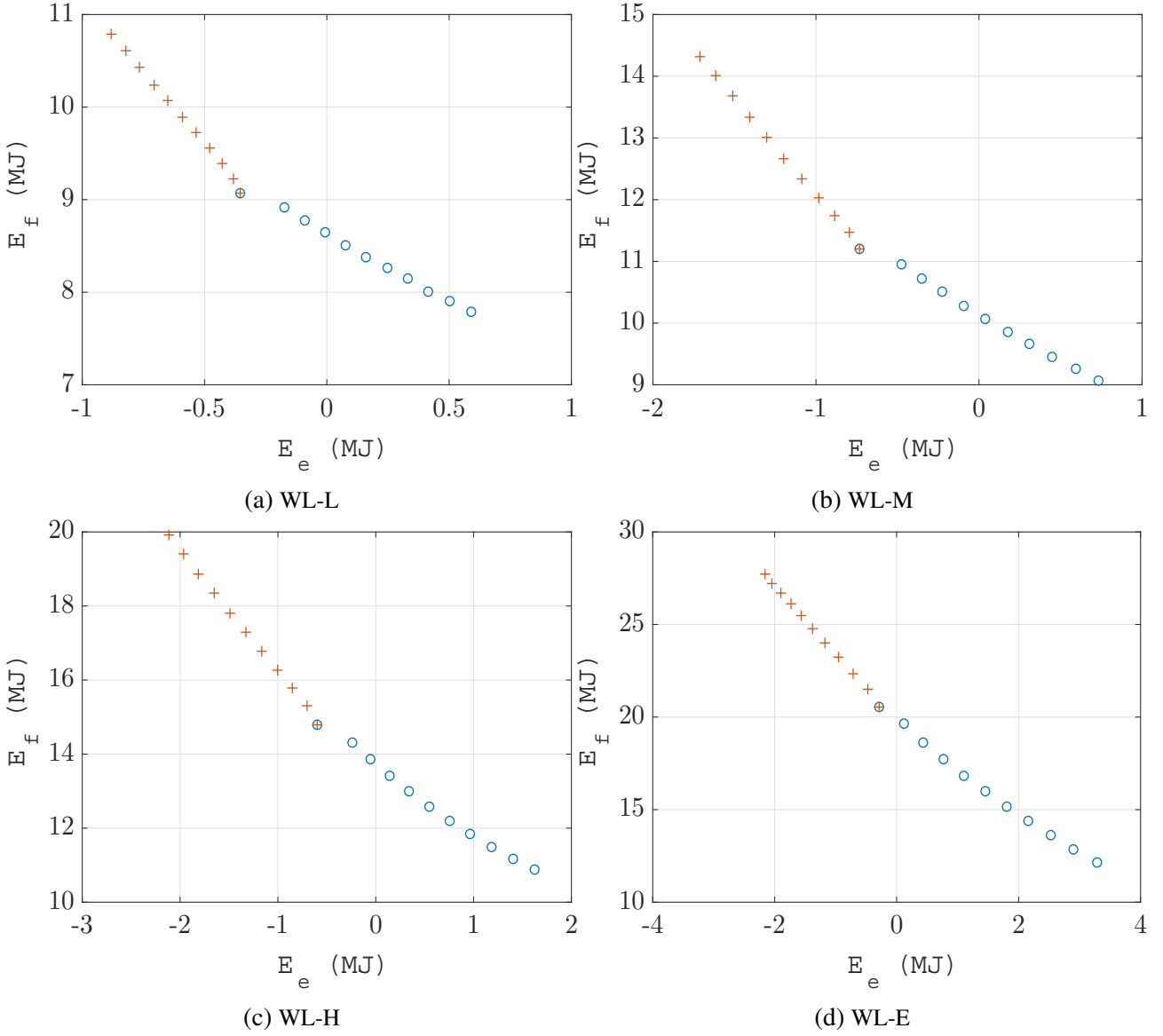


Figure 4.1: Correlation between the electrical energy E_e , and the fuel energy E_f , for driving cycles WL-L (a), WL-M (b), WL-H (c) and WL-E (d) for the model Alpha.

Table 4.4: Optimal ECMS equivalence factors for the model Beta

Driving cycle	S_c	S_d
WL-L	2.8	4.4
WL-M	2.7	4.3
WL-H	2.8	4.1
WL-E	2.6	3.6

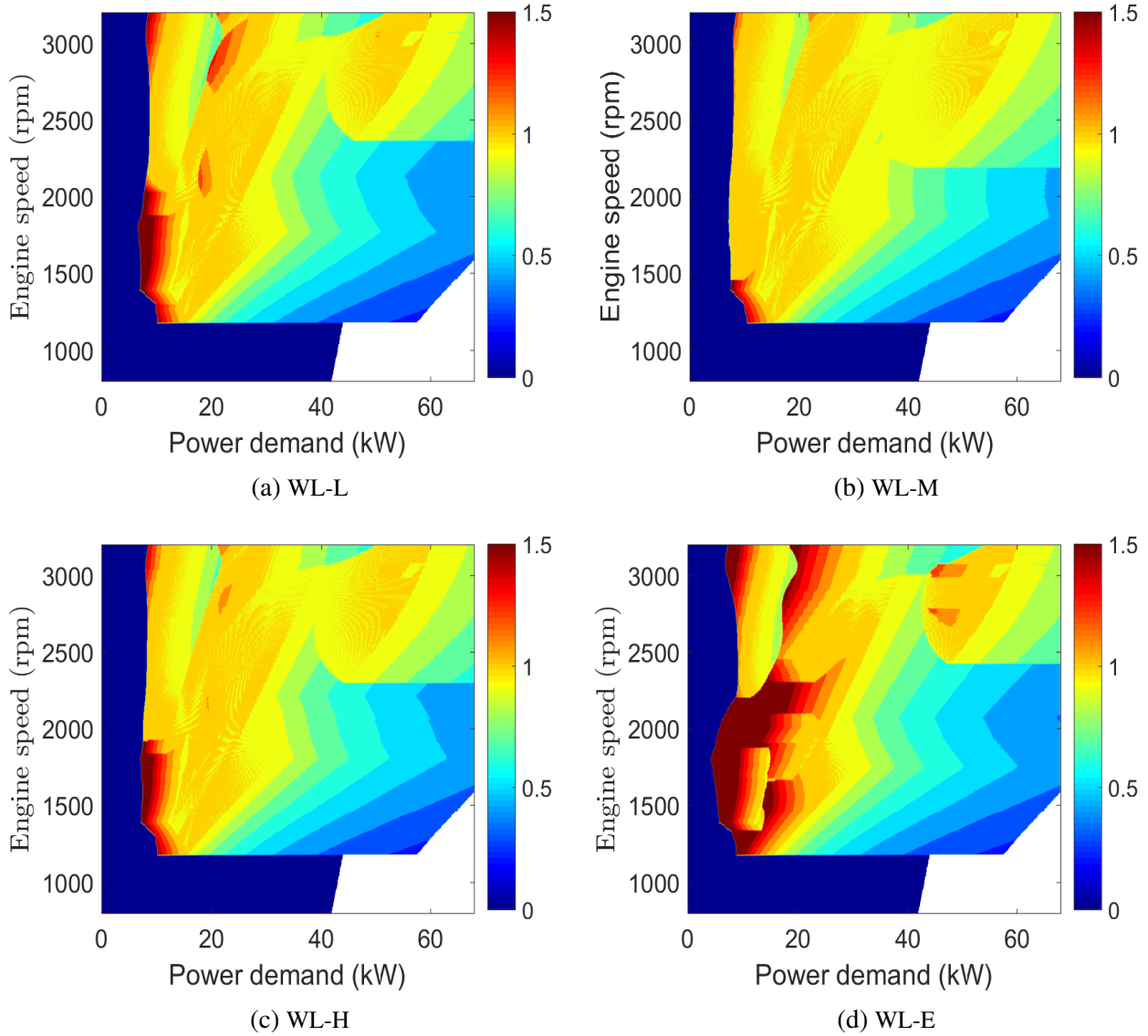


Figure 4.2: Optimal ECMS power share factor maps for the standard driving cycles for the model Alpha; dark blue corresponds to pure electric mode, and white represents the infeasible region. The maps are for driving cycles WL-L (a), WL-M (b), WL-H (c) and WL-E (d).

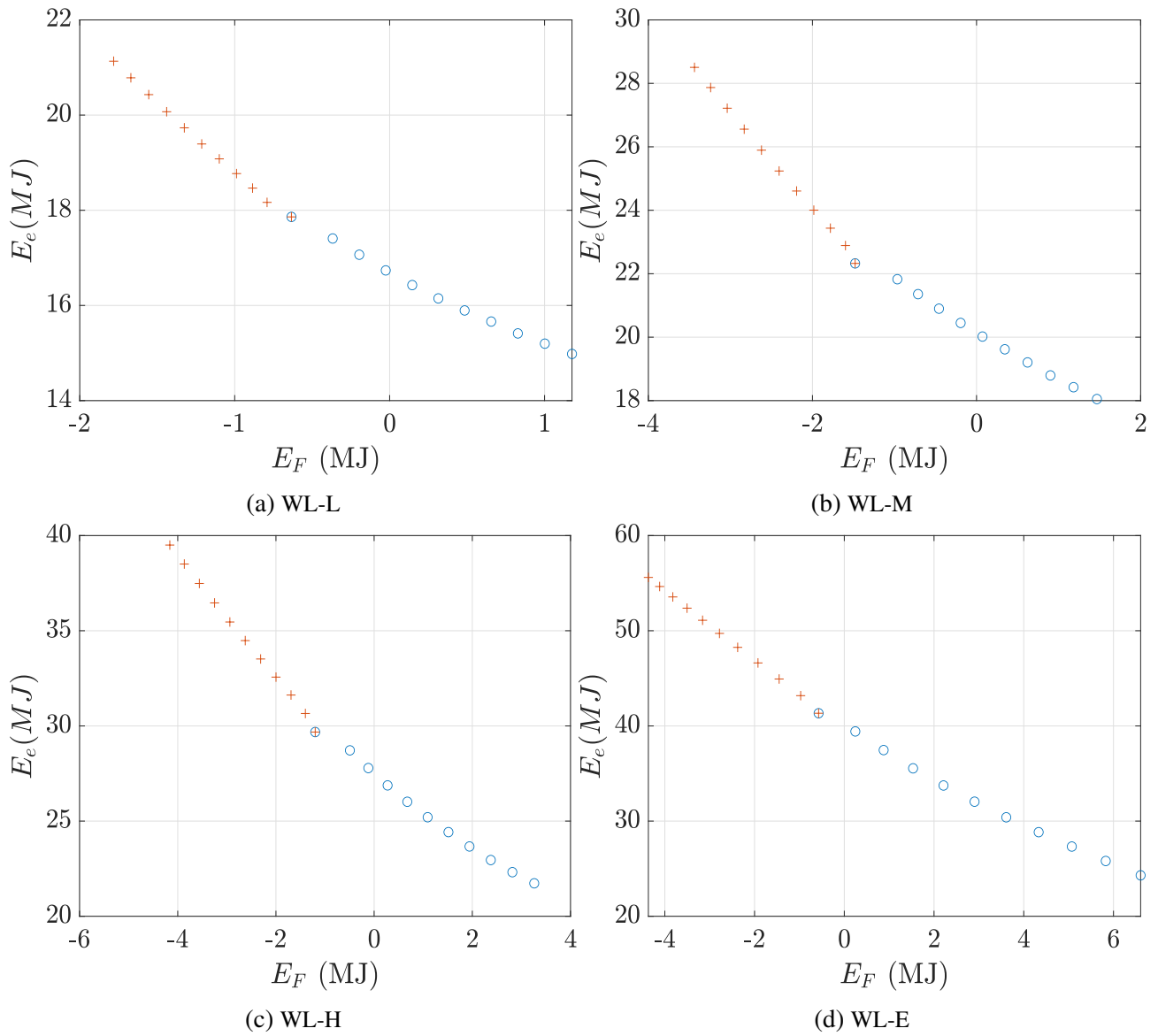


Figure 4.3: Correlation between the electrical energy E_e , and the fuel energy E_f , for driving cycles WL-L (a), WL-M (b), WL-H (c) and WL-E (d) for the model Beta.

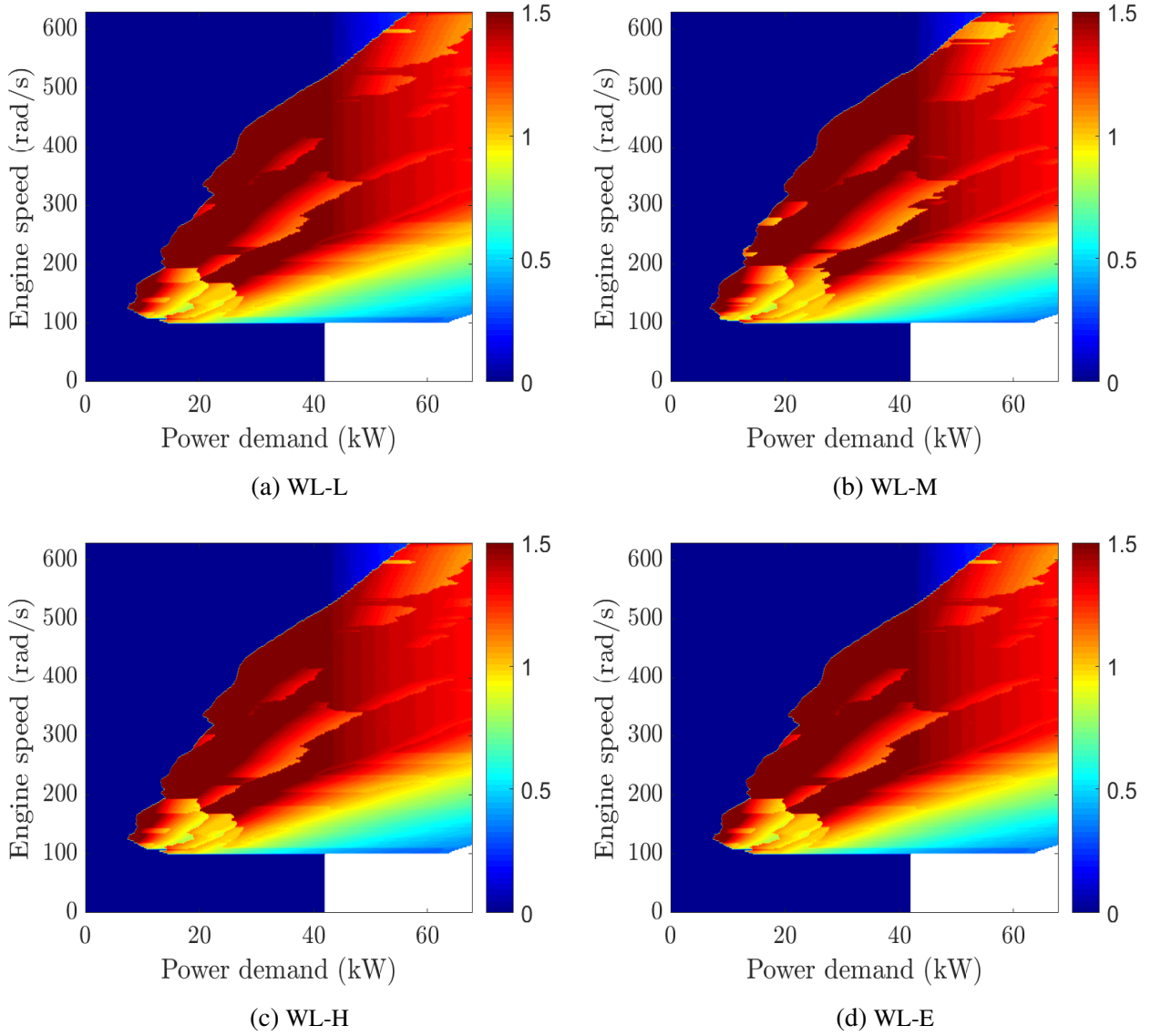


Figure 4.4: Optimal ECMS power share factor maps for the standard driving cycles for the model Beta; dark blue corresponds to pure electric mode, and white represents the infeasible region. The maps are for driving cycles WL-L (a), WL-M (b), WL-H (c) and WL-E (d).

4.2 Chapter Summary

The conventional strategy ECMS was described and implemented on the developed TTR HEV model from Chapter 3. The optimal equivalence factors were identified for two models (i.e. the model Alpha and Beta). The EFC optimal equivalence factors were then used to compute the fuel economy in four standardised drive cycles WL-L, WL-M, WL-H and WL-E. This method is used as a benchmark in the subsequent chapters of this part of the thesis to evaluate the performance of the heuristic methods implemented in Chapter 5.

Chapter 5

Heuristic Control Strategies for the Energy Management of HEVs

In this chapter, the knowledge gained from implementing the ECMS presented in Chapter 4 is utilised to develop heuristic strategies. The chapter starts with the Torque-levelling Threshold-changing Strategy (TTS) in section 5.1, followed by the simplified version, Simplified Torque-levelling Threshold-changing Strategy (STTS) in section 5.2. The real-time versions, Real-time Torque-levelling Threshold-changing Strategy (RTTS) and Real-time Simplified Torque-levelling Threshold-changing Strategy (RSTTS), are discussed in subsection 5.3.1 and subsection 5.3.2, respectively.

5.1 Torque-Levelling Threshold-Changing Strategy (TTS)

This section describes the main design principles of the TTS inspired by [112, 121].

Torque-levelling

In the load-levelling approach, the fuel energy source is operated steadily while the electric energy source acts as a buffer and is used to 'level' the load [74]. The TCS and OPSS are amongst the strategies which are based on the load-levelling principle [6]. In [72] and [82], the SCS of the parallel

HEV is based on the load-levelling concept, in which the engine's operating point is forced to be at or near the maximal efficiency point; this requires the engine power to be changed accordingly. The TCS, as well as other load-levelling methods, are usually applicable to series HEVs, in which there is no direct mechanical connection between the engine and the wheels. Thus, the engine-generator set can be operated more steadily [16].

In the TCS, the state of the engine (i.e. on/off) is controlled by the SOC of the battery. As the SOC of the battery reaches the upper limit, the engine is turned off, and the vehicle is propelled only using the electrical power source. Once the SOC of the battery hits the lower limit, the engine is turned back on again. As long as the engine is on, it is operated on its optimal curve.

In a parallel architecture, the engine speed is constrained by the wheel speed as there is a mechanical connection between them (i.e. the transmission). Therefore, there is more control over the choice of the engine rather than wheel speed. By observing the typical engine efficiency maps such as the one shown in Figure 3.3b and Figure 3.4b, it can be observed that for constant power, as the engine speed increases, the efficiency fluctuates and in most cases, decreases. The engine's operation is infeasible at high powers and low speeds due to torque saturation.

The above-mentioned issues and remarks call for a new load-levelling strategy for parallel HEVs, in which constant engine torque is applied, irrespective of the engine speed.

The new concept of 'Torque-levelling' was inspired by the power-following concept. For a constant load power, the power share factor increases as the engine speed increases (i.e. vertically). This trend can also be seen in the heuristic control maps Figure 5.1 and Figure 5.2, which will be discussed in Chapter 6. A similar torque-levelling behaviour can be observed in ECMS control maps visualised in Figure 4.2.

Threshold-changing

The HEV is operated in pure electric mode if the load power is lower than the power threshold. In this concept, power thresholds determine the activation of the engine. This mechanism has been used in the context of series HEVs in strategies such as the Efficiency Maximising Map Strategy

(EMMS), OPSS, and XOS [6, 122]; these thresholds are generally SOC-dependent; The operation of the secondary source is encouraged when SOC is high and discouraged when SOC is low; this mechanism leads to a more effective CS operation compared to the state-changing approaches such as TCS and PFCS [6]. In parallel HEVs, the threshold-changing mechanism has also been used in EACS and ECMS.

The above-mentioned design principles can now be applied to develop a novel heuristic control strategy for parallel HEVs. The power thresholds in this work are both SOC and engine speed dependent:

$$\begin{aligned} P_{edmin}(SOC, \omega_e) &= P_{th} + P_{th} \frac{SOC - SOC_{mid}}{SOC_{range}} + P_{\omega} + P_{\omega} \frac{\omega_e - \omega_{mid}}{\omega_{range}} \\ &= P_{th} \frac{SOC - SOC_{min}}{SOC_{range}} + P_{\omega} \frac{\omega_e - \omega_{min}}{\omega_{range}} \end{aligned} \quad (5.1)$$

where P_{th} and P_{ω} are the power thresholds dependent on SOC and engine speed (ω_e), respectively. $X_{mid} = \frac{X_U + X_L}{2}$, $X_{range} = \frac{X_U - X_L}{2}$ with $X \in \{SOC, \omega_e\}$, X_U being the upper limit and X_L being the lower limit and P_{edmin} being the minimum engine driving power. The control maps of the TTS for engine model Alpha and Beta are presented in Figure 5.1 and Figure 5.2, respectively, with two cross-sections at $\omega = \omega_{mid}$ and $SOC = SOC_{mid}$ taken from a 3D map of SOC , ω_e and P_{PL} . In these control maps, T_{ed} is the output torque from the primary power source, P_{edmax} is the maximum engine driving power, and P_{mdmax} is the maximum secondary source driving power.

The operating rules of the TTS are presented in Figure 5.3. The control map in Figure 5.3a is captured at the cross-section $\omega = \omega_{mid}$, in which the speed-dependent threshold P_{ω} decides whether the engine is operated with constant torque. If $P_{\omega} < P_{PL} < P_{edmax}$ and $SOC_U < SOC < SOC_L$, then the torque-levelling mechanism is applied, and the engine is operated with a constant torque $T_{ed} = T_c$ (green regions). If $SOC < SOC_L$ or $P_{PL} > P_{edmax}$, then $P_{PL} = P_{edmax}$ (blue regions). This design uses insights from rule-based strategies developed for series HEVs such as OPSS and XOS [6]. The control map in Figure 5.3b is captured at the cross-section $SOC = SOC_{mid}$, in which the SOC-dependent threshold P_{th} defines the slope of the map. The threshold-changing mechanism visualised in Figure 5.3 is similar to the engine's activation pattern at medium loads and medium to high engine speeds in the ECMS. When $P_{th} < P_{PL} < P_{edmax}$ and $\omega_L < \omega < \omega_U$, then the torque-levelling approach is applied (green

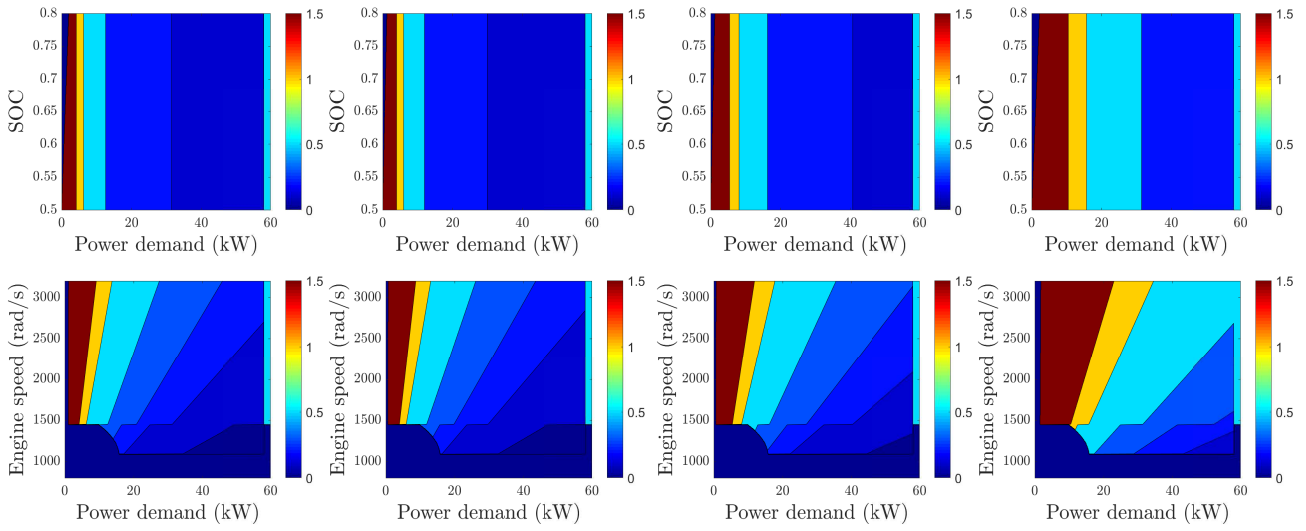


Figure 5.1: Optimal TTS power share factor for WL-L, WL-M, WL-H and WL-E, left to right, respectively; the top row consists of maps at the cross-section of $\omega = \omega_{mid}$ and the bottom row at $SOC = SOC_{mid}$. Dark blue corresponds to pure electric mode, and white represents the infeasible region. These maps are for the engine model Alpha.

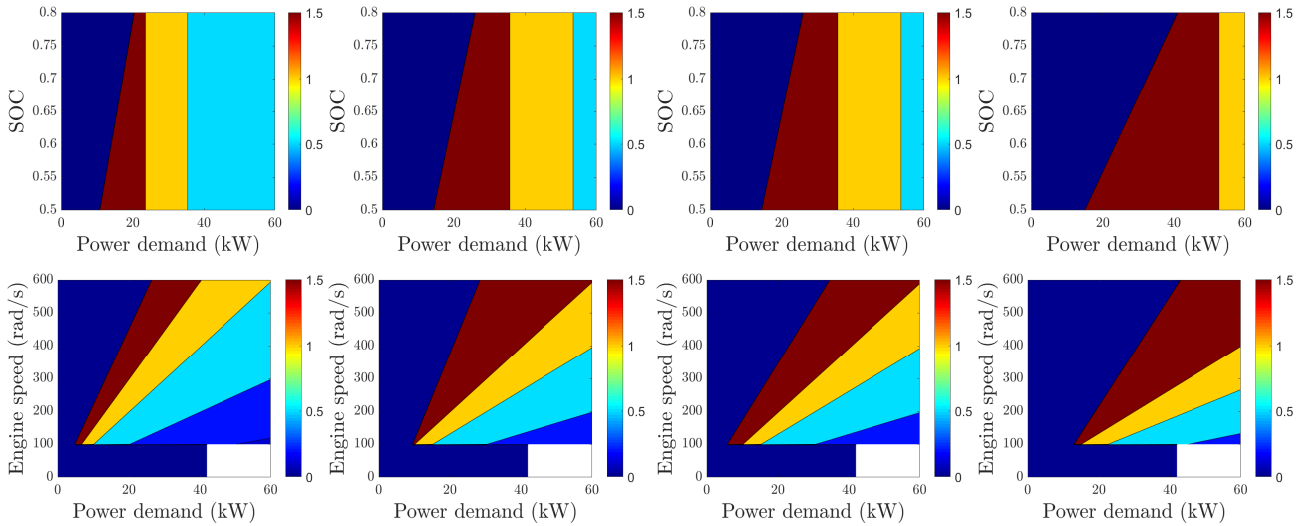
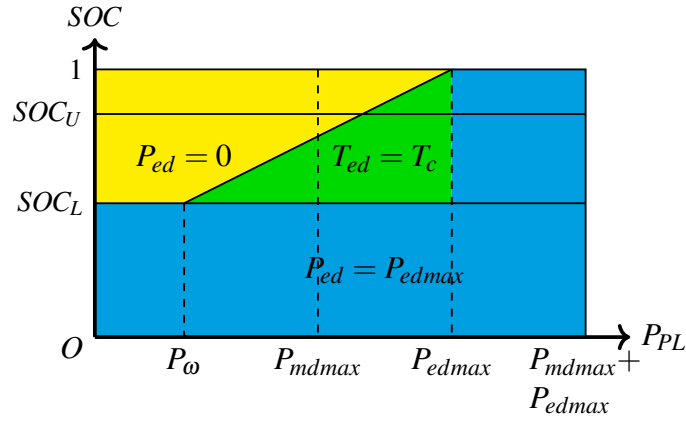


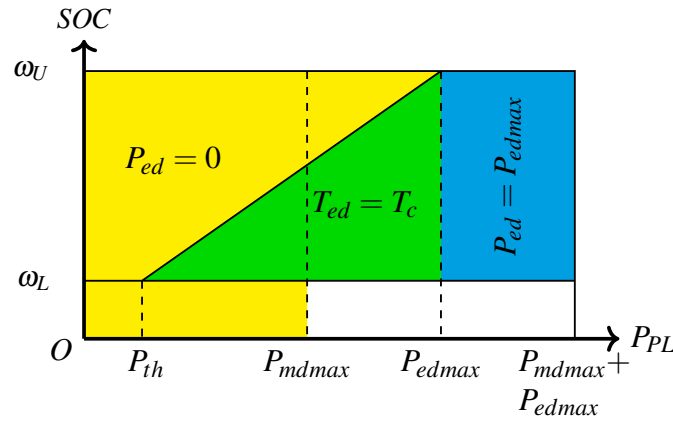
Figure 5.2: Optimal TTS power share factor for WL-L, WL-M, WL-H and WL-E, left to right, respectively; the top row consists of maps at the cross-section of $\omega = \omega_{mid}$ and the bottom row at $SOC = SOC_{mid}$. Dark blue corresponds to pure electric mode, and white represents the infeasible region. These maps are for the engine model Beta.

regions). The TTS has three tuning parameters and a reduced tuning time compared to the ECMS.

The globally tuned optimal parameters for the TTS are summarised in Table 5.1 for the model Alpha and in Table 5.2 for Beta.



(a) The cross-section of control rules at $\omega_e = \omega_{mid}$.



(b) The cross-section of control rules at $SOC = SOC_{mid}$.

Figure 5.3: The TTS operates in three distinct modes depending on the given SOC , ω_e and P_{PL} : Electric mode (yellow), constant ICE torque mode (green), maximum ICE power mode (blue). White represents the infeasible region.

5.2 Simplified Torque-levelling Threshold-changing Strategy (STTS)

The engine speed variation is not significant during all standardised driving cycles studied in this work; therefore, to eliminate a tuning parameter and to make TTS more practical, a simplified version

Table 5.1: TTS optimal parameters for the model Alpha

Driving cycle	P_{th}	P_{ω}	T_c
WL-L	0.6	0.1	41
WL-M	0.5	0.5	39
WL-H	0.5	0.5	53
WL-E	1.1	1.1	102.5

Table 5.2: TTS optimal parameters for the model Beta

Driving cycle	P_{th}	P_{ω}	T_c
WL-L	4.8	10.8	101
WL-M	9.5	9.5	152
WL-H	5.8	14.4	153
WL-E	13	15	226

is introduced, in which the design parameter P_{ω} is eliminated. The threshold equation is reduced from Equation 5.1 to:

$$P_{edmin}(SOC) = P_{th} + P_{th} \frac{SOC - SOC_{min}}{SOC_{range}} \quad (5.2)$$

The STTS modifies the threshold to be SOC-dependent only. The globally tuned optimal parameters for the STTS are summarised in Table 5.3 for the model Alpha.

Table 5.3: STTS optimal parameters for the model Alpha

Driving cycle	P_{th}	T_c
WL-L	0.3	42
WL-M	0.3	38.5
WL-H	0.3	53
WL-E	0.5	102

5.3 Novel Real-time Heuristic Control Strategies

This section aims to develop real-time versions of the TTS and STTS to facilitate practical applications. The main idea is to make the TTS and STTS causal (i.e. not relying on apriori knowledge). As discussed in section 5.1 and section 5.2, the three design parameters P_{th} , P_{ω} , and T_c in the TTS and P_{th} , and T_c in the STTS, need to be determined by an exhaustive search or global tuning for each given drive cycle. In practice, the controller has limited memory resources and computational capacity; therefore, relying on the prediction of future driving conditions and solving a deterministic

optimal control online is not suitable [79]. As a result, more computational time can be spent on modelling. From a control perspective, this corresponds to a levelling problem in which SOC shall be kept as close as possible to SOC_{init} to prevent battery overcharge or depletion [123]. In the literature, few attempts have been made to implement pattern recognition algorithms [70, 80]. This section proposes real-time updating laws to determine the TTS and STTS parameters online based on a novel Driving Pattern Recognition (DPR) approach and SOC-dependent feedback controllers to achieve CS operation.

5.3.1 Real-time Torque-levelling Threshold-changing Strategy (RTTS)

Most driving cycles (standardised or experimental) comprise low, medium, high and extra high-speed segments. Inspired by this remark, a novel DPR algorithm is proposed with four representative driving patterns (i.e. WL-L, WL-M, WL-H and WL-E). Each driving pattern is associated with a set of TTS optimal parameters presented in Table 5.1 and Table 5.2, along with real-time updating laws for the control parameters.

The main idea is to refresh the power thresholds P_{th} , P_{ω} , and the constant engine torque T_c , according to the SOC and propulsion load P_{PL} . To increase the robustness of the controllers, a feedback control system is introduced to account for unexpected events such as driver behaviour and road conditions. Each driving pattern is associated with a pre-defined maximum propulsion load P_{PL}^i , and a pre-defined maximum vehicle speed v^i , with $i \in \{L, M, H, E\}$ representing the specific driving cycle. The schematic diagram for the DPR algorithm is presented in Figure 5.4. By employing this algorithm, the driving pattern at each time instant can be recognised; therefore, the instantaneous engine torque T_c is computed, with T_c^i being the TTS optimal constant engine torque value determined by the DPR logic. The constant engine torque level for each driving cycle is the TTS optimal torque identified for every drive cycle in Table 5.1 and Table 5.2. Furthermore, to ensure a CS operation of the RTTS, a fine-tuned PI controller is incorporated along with the pattern recognition module. The real-time engine torque is determined as follows:

$$T_c(t) = T_c^i(t) + K_P^T e_{soc}(t) + K_I^T \int_0^t e_{soc}(t) dt \quad (5.3)$$

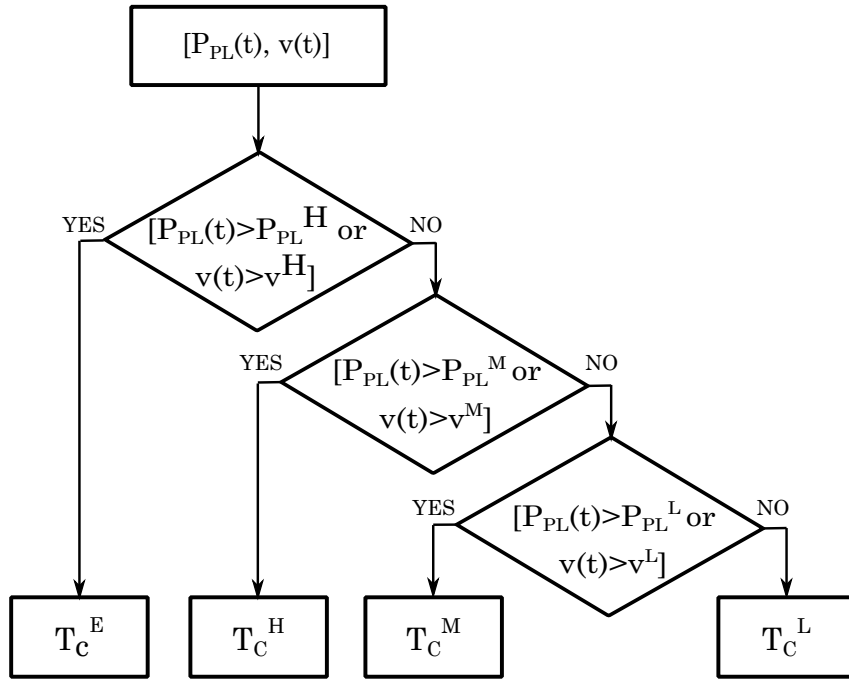


Figure 5.4: DPR block diagram.

where $e_{soc}(t) \triangleq SOC_{init} - SOC(t)$, K_P^T , K_I^T represent the proportional and integral gains of the torque-feedback PI controller, and T_c^i represents the optimal TTS constant engine torque value for each driving cycle taken from Table 5.1 and Table 5.2 for the models Alpha and Beta, respectively. To further improve efficiency, an appropriate minimum engine torque for every engine speed is also incorporated:

$$T_c(t) = \max\{T_c^i(t) + K_P^T e_{soc}(t) + K_I^T \int_0^t e_{soc}(\tau) d\tau, T_{emin}(\omega_e)\}, \quad (5.4)$$

with $T_{emin}(\omega_e)$ being the minimum speed-dependent engine torque corresponding to an ICE efficiency of 30%.

For each of the two threshold parameters P_{th} and P_ω , a PI controller is designed to make RTTS adaptive to real-time driving conditions:

$$P_{th}(t) = P_{th}^L + K_P^{th} e_{soc}(t) + K_I^{th} \int_0^t e_{soc}(\tau) d\tau \quad (5.5)$$

$$P_\omega(t) = P_\omega^L + K_P^\omega e_{soc}(t) + K_I^\omega \int_0^t e_{soc}(\tau) d\tau \quad (5.6)$$

where P_{th}^L and P_ω^L are the optimal power threshold values for WL-L since a low speed characterises most drive cycles at the very beginning; K_P^{th} and K_P^ω are the power thresholds feedback loops' pro-

portional gain factors, and K_I^{th} and K_I^ω are the power thresholds feedback loops' integral gain factors.

5.3.2 Real-time Simplified Torque-levelling Threshold-changing Strategy (RSTTS)

The RSTTS is similar to the RTTS in principle, with one less tunable power threshold parameter. The main idea is to update the control parameters P_{th} and T_c at every time instant, incorporating the DPR algorithm visualised in Figure 5.4. A PI controller is used to compute the value of the power threshold P_{th} , which is presented in Equation 5.5.

A second PI controller is used to compute the value of T_c online as in Equation 5.4 with T_c^i being the optimal STTS engine torque value for every driving cycle taken from Table 5.3.

5.4 Chapter Summary

This chapter has discussed insights gained from the ECMS presented in Chapter 4; these insights served as design principles for developing novel heuristic control strategies.

The TTS and the STTS were developed using insights from [121] and implemented on the TTR HEV model presented in Chapter 3. The TTS and STTS were benchmarked against the conventional strategy ECMS, presented in Chapter 4. With simple rules and tunable parameters, TTS is computationally-efficient and easy to implement on any parallel HEV. The two main design principles of TTS are 'Torque-levelling' and 'Threshold-changing'. The STTS uses one less tunable threshold parameter but is similar in principle.

To show the effectiveness of TTS, a novel real-time controller, RTTS, was developed based on a novel DPR algorithm. In practice, the vehicle controllers need more memory resources and computational capacity; therefore, relying on predicting future driving conditions and solving a real-time deterministic optimal control problem is unrealistic.

The TTS predefined power thresholds P_{th} and P_{ω} , and the constant torque level T_c , are updated in real-time based on SOC and the propulsion load. To increase the robustness of the controllers, three feedback control loops in the RTTS and two feedback control loops in the RSTTS were incorporated to account for unexpected events such as driver behaviour and road load and to achieve CS operation.

Chapter 6

Simulation Results for the Energy Management of HEVs

The ECMS presented in Chapter 4 and the heuristic control strategies (TTS, STTS, RTTS and RSTTS) presented in Chapter 5 have been implemented on the TTR HEV model shown in Chapter 3 to evaluate the effectiveness of the proposed control strategies. In this study, simulations are conducted on the four segments of the Worldwide Harmonised Light vehicle Test Procedure (WLTP) (WL-L (low speed), WL-M (medium speed), WL-H (high speed) and WL-E (extra-high speed)) [124], illustrated in Figure 6.1. In addition, an experimental drive cycle measured by a data acquisition device on a rural road in London [125] is used. This drive cycle is referred to as the Experimental drive cycle and is presented in Figure 6.11.

6.1 Implementation of the ECMS, TTS and STTS

In this section, the optimal control maps produced by the ECMS (as shown in Figure 4.2 and Figure 4.4) are implemented on the models Alpha and Beta. Moreover, the TTS is implemented on the same models. The STTS is only implemented on the model Alpha. The corresponding power profiles are visualised and analysed in subsection 6.1.1, SOC profiles in subsection 6.1.2 and fuel economy results in subsection 6.1.3.

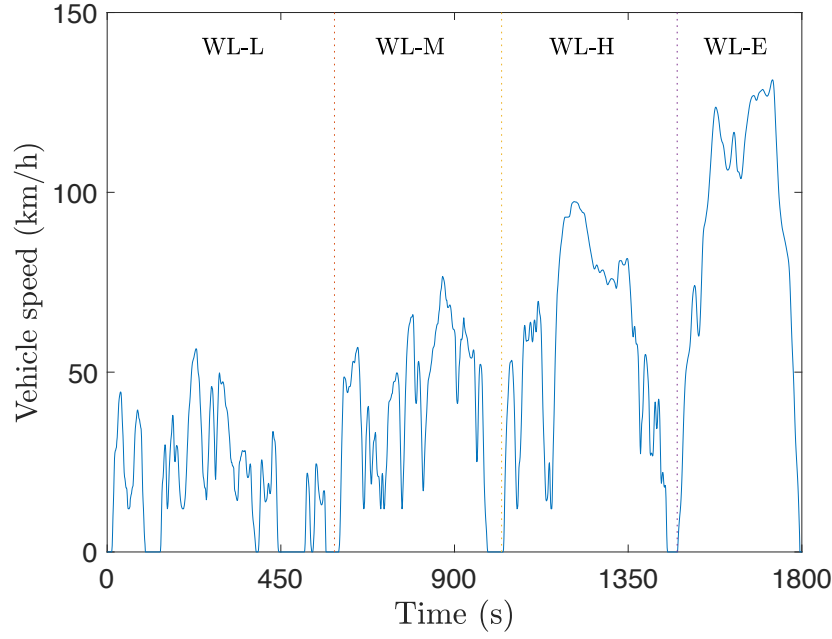


Figure 6.1: Four components of the WLTP (WL-L, WL-M, WL-H and WL-E).

6.1.1 Power Profiles

ECMS Profiles

The Model Alpha ECMS power profiles, which show the power distribution across the primary and secondary sources, are presented in Figure 6.2 for the WL-L, WL-M, WL-H, and WL-E segments of the WLTP. These power profiles show that pure electric operating mode is utilised at low power loads, which is unsurprising as the engine efficiency is relatively low in these regions. In the WL-L and the WL-E, when the engine is active, it often delivers more power than the requested load and charges the battery. During the WL-M and WL-H, the ICE works mainly with a load-following mode since the engine efficiency is generally high at such loads (as seen in the engine efficiency map presented in Figure 3.3b). In the WL-E, the ECMS often operates the powertrain with a hybrid mode as the average propulsion load demand is high. In this case, the primary and the secondary power sources drive the vehicle simultaneously, with the ICE being the primary power source. The power profiles of model Beta, presented in Figure 6.3, exhibit a similar trend to those of model Alpha, with pure electric operation at low loads and ICE activation at higher loads. In all driving cycles, the ICE generates more power than the propulsion load demand, resulting in charging the battery. This is because the

engine model Beta has a higher rated power than the engine model Alpha, as demonstrated by their efficiency maps in Figure 3.3b and Figure 3.4b, respectively. Furthermore, the engine model Beta is more efficient in the high-power region at the same speed, which eliminates the need for a hybrid mode during the WL-E when the average propulsion load demand is high.

TTS and STTS Profiles

With the globally tuned optimal parameters presented in Table 5.1 for the model Alpha, the TTS power profiles are visualised in Figure 6.4. There is a pure electric operation at low loads. The engine charges the battery in all driving cycles. Hybrid mode is observed in all drive cycles as opposed to only during the WL-E in the model Alpha ECMS profiles. The ICE is operated more steadily and with a lower average load power. Additionally, less SSS is associated with the TTS.

With the globally tuned optimal parameters presented in Table 5.2 for the model Beta, the TTS power profiles are visualised in Figure 6.5. In these profiles, similarly to the model Beta ECMS profiles, there is a pure electric operation at low loads and almost no hybrid operation. The ICE is operated more steadily compared to the ECMS and with a lower average load power.

With the globally tuned optimal parameters shown in Table 5.3, the resulting STTS power profiles are presented in Figure 6.6. The STTS power profiles follow the same trends as the TTS power profiles. For this reason, the STTS has not been implemented on the model Beta.

Key Findings

Model Alpha power profiles:

- Both strategies exhibit pure electric operation at low loads.
- The engine charges the battery more frequently in the TTS during all drive cycles compared to the ECMS, with only a few exceptions in the WL-H and the WL-E.
- Hybrid operation is observed often in the TTS during all drive cycles and only a few cases in the ECMS during the WL-L and the WL-E.

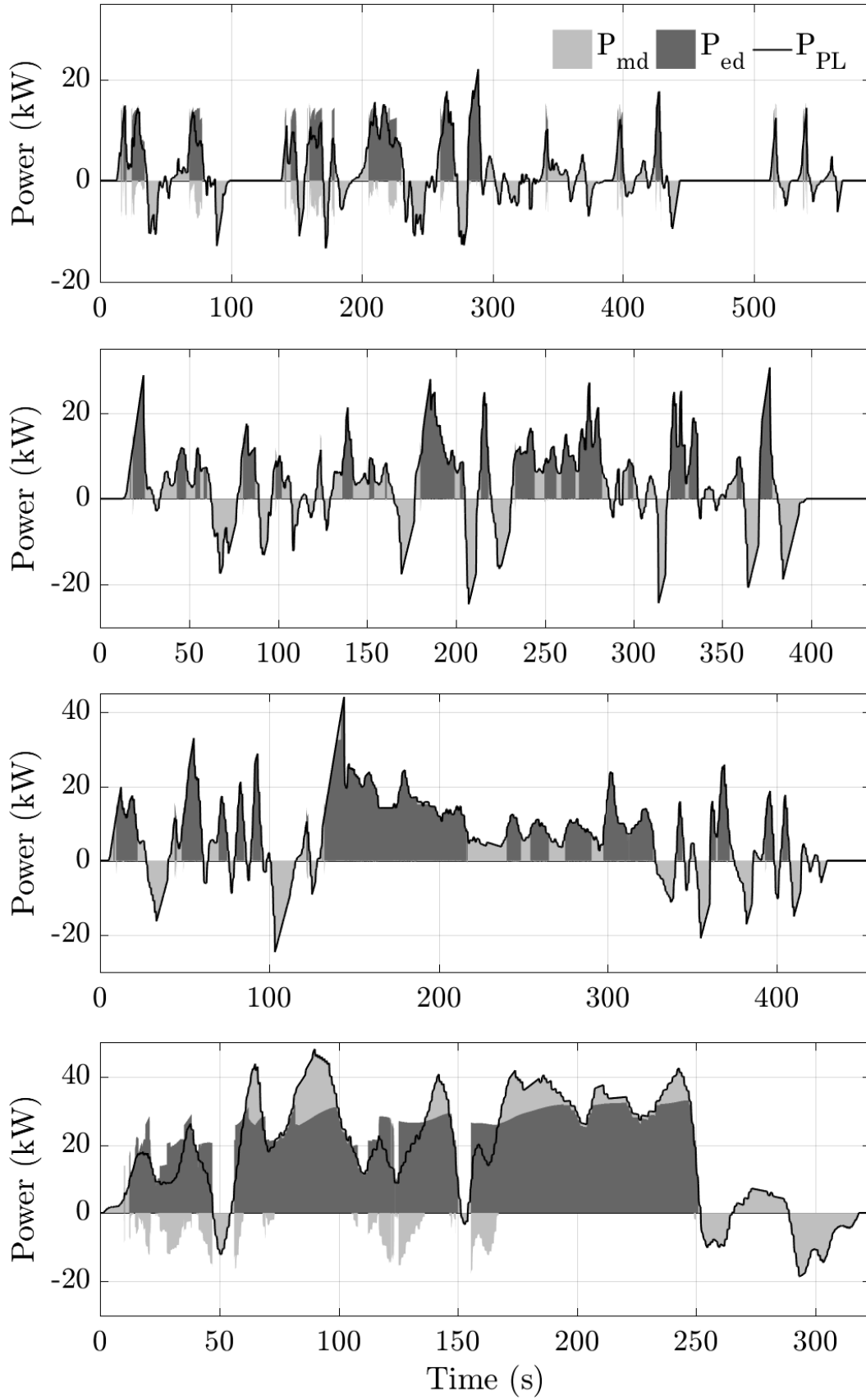


Figure 6.2: ECMS power time profiles for the engine power P_{ed} , motor/generator power P_{md} , and load power P_{PL} for the first iteration of driving cycles WL-L, WL-M, WL-H, and WL-E, top to bottom. These plots are for the model Alpha.

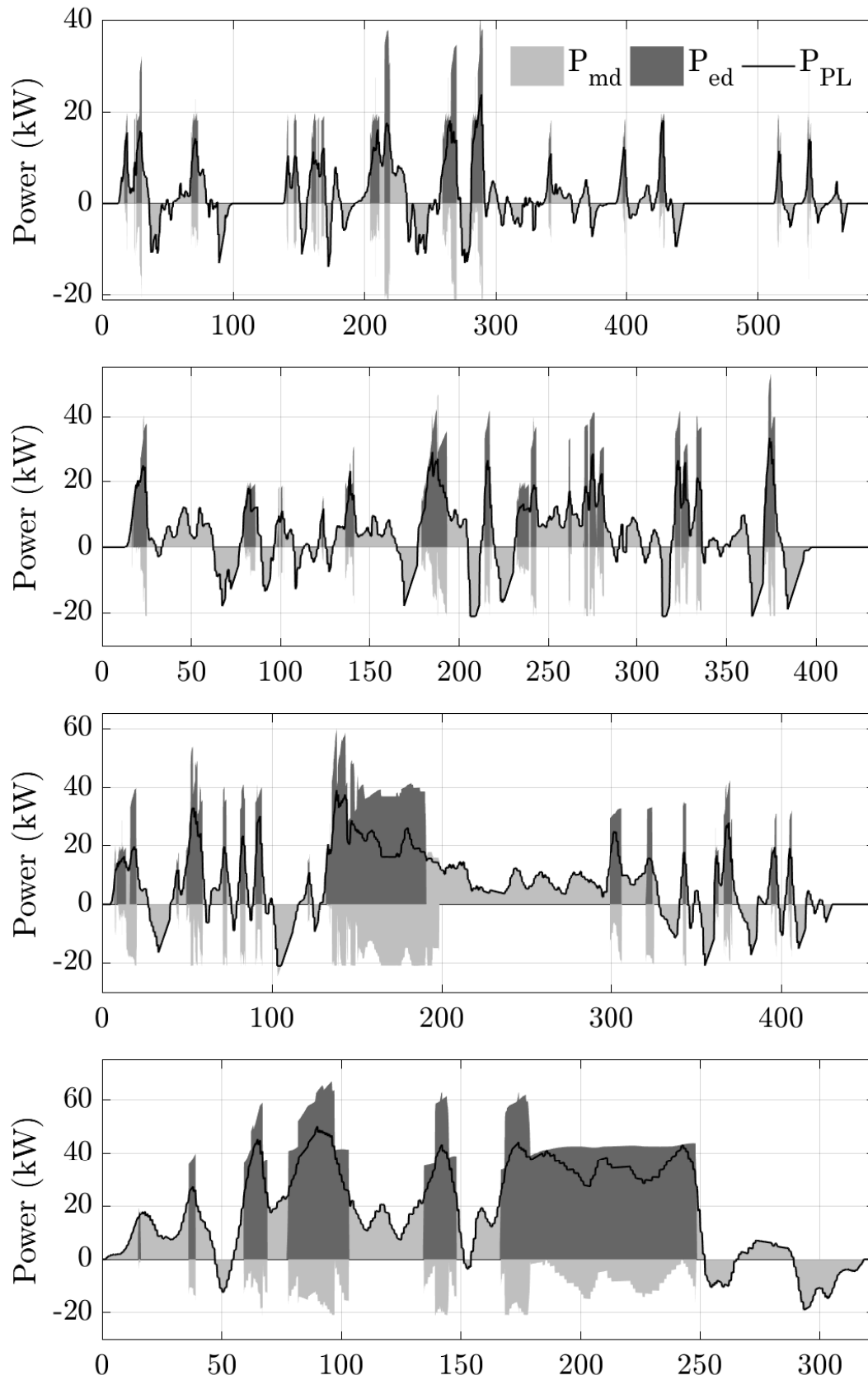


Figure 6.3: ECMS power time profiles for the engine power P_{ed} , motor/generator power P_{md} , and load power P_{PL} for the first iteration of driving cycles WL-L, WL-M, WL-H, and WL-E, top to bottom. These plots are for the model Beta.

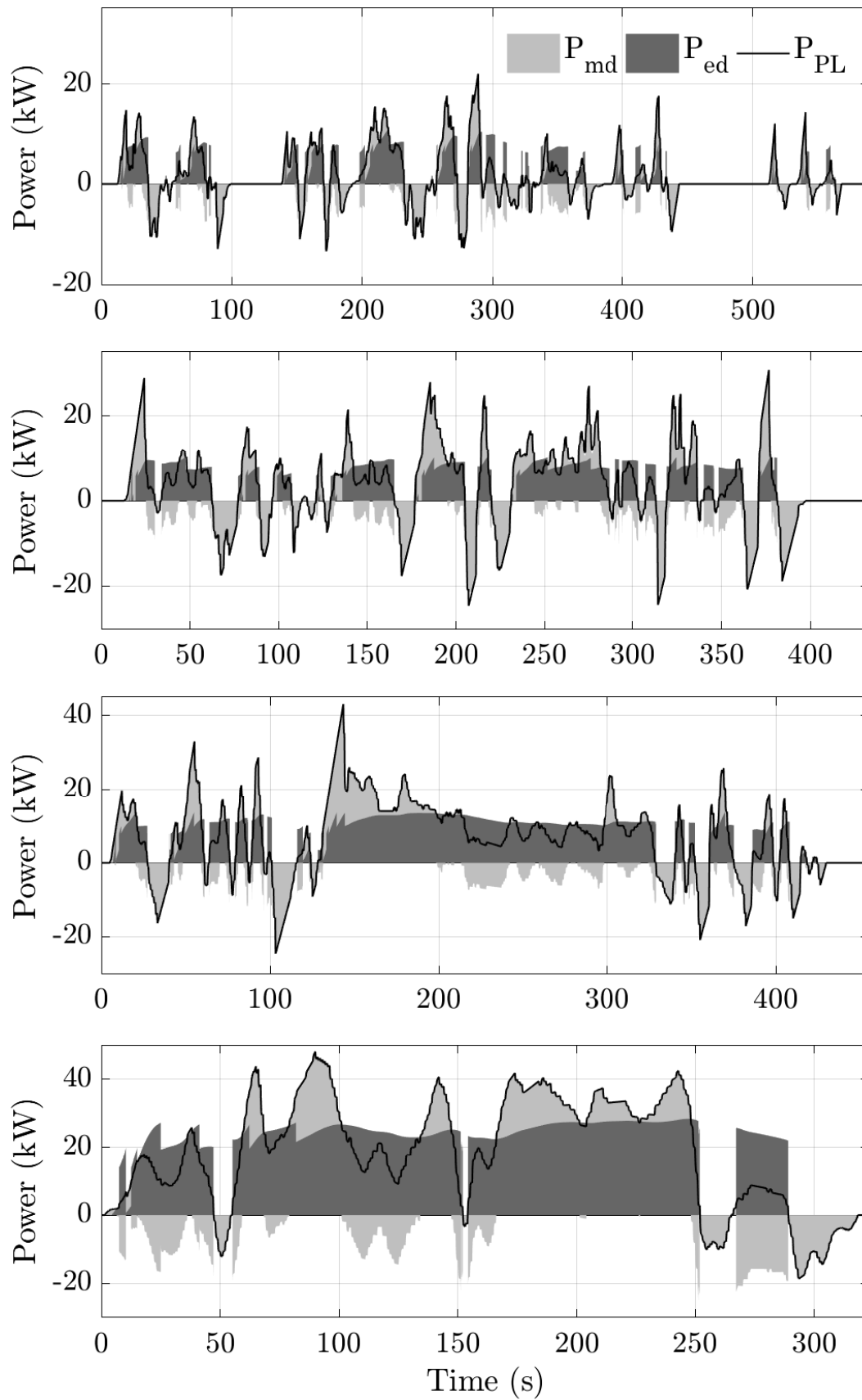


Figure 6.4: TTS power time profiles for the engine power P_{ed} , motor/generator power P_{md} , and load power P_{PL} for the first iteration of driving cycles WL-L, WL-M, WL-H, and WL-E, top to bottom. These plots are for the model Alpha.

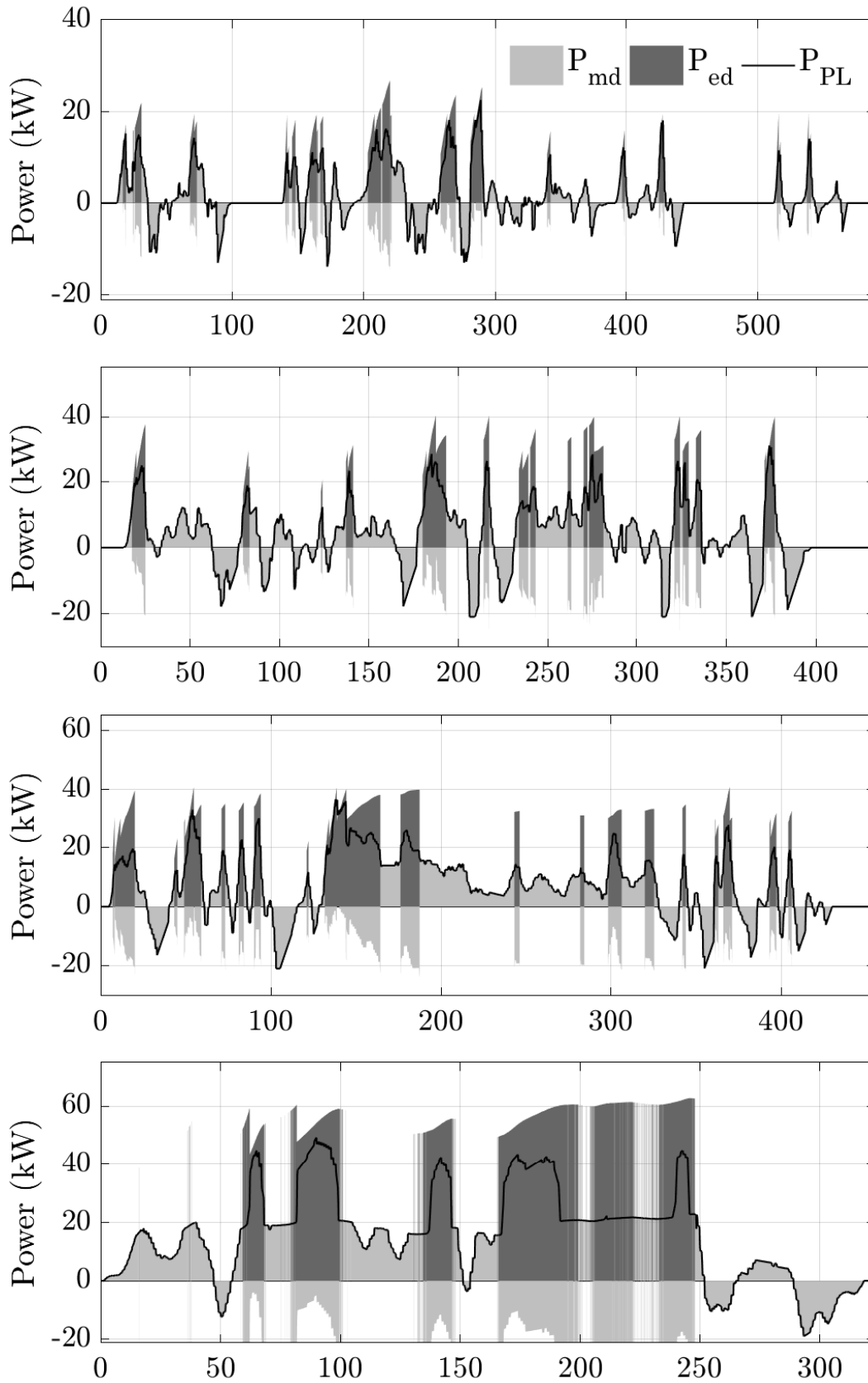


Figure 6.5: TTS power time profiles for the engine power P_{ed} , motor/generator power P_{md} , and load power P_{PL} for the first iteration of driving cycles WL-L, WL-M, WL-H, and WL-E, top to bottom. These plots are for the model Beta.

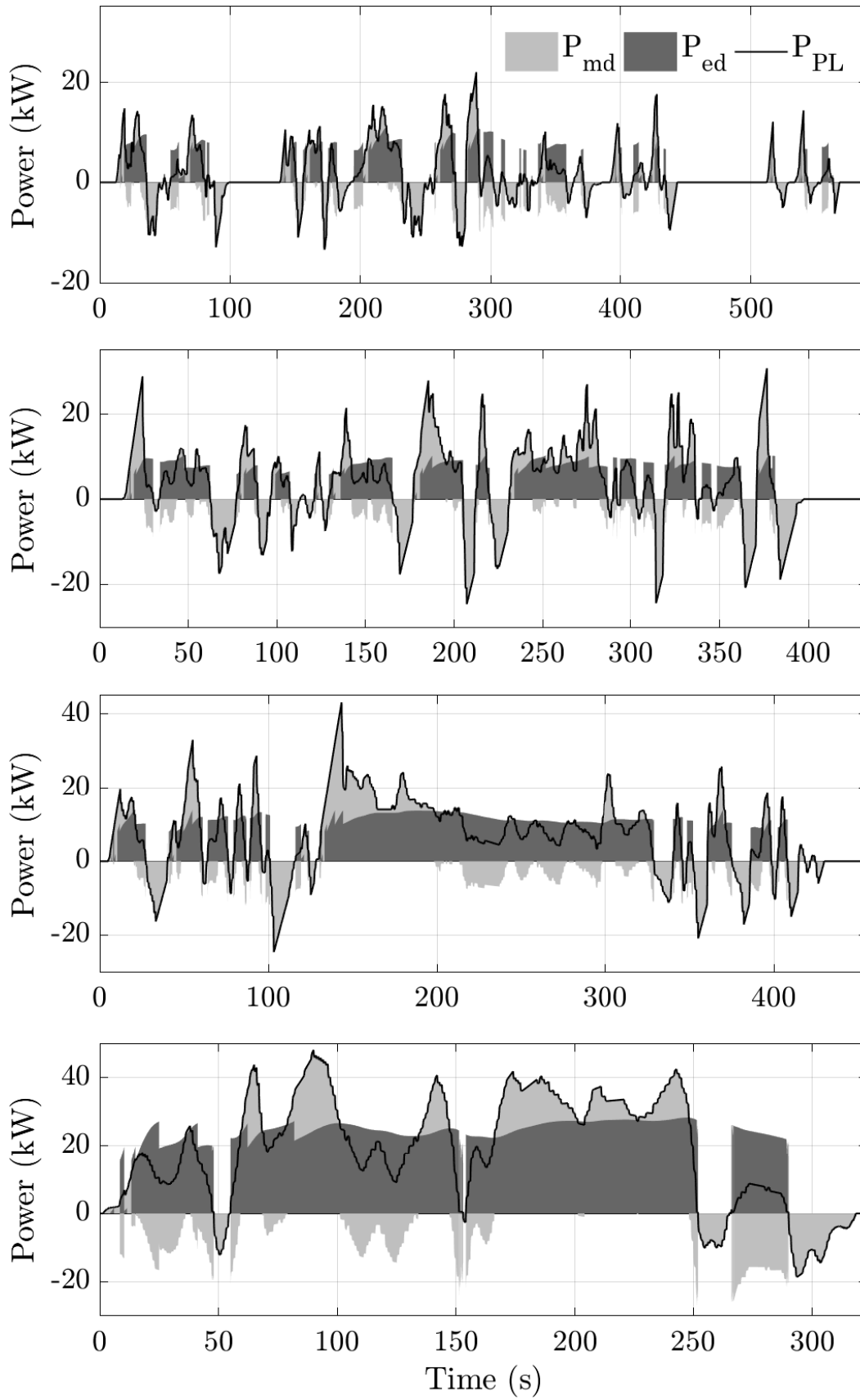


Figure 6.6: STTS power time profiles for the engine power P_{ed} , motor/generator power P_{md} , and load power P_{PL} for the first iteration of driving cycles WL-L, WL-M, WL-H, and WL-E, top to bottom. These plots are for the model Alpha.

- Less SSS is observed in the TTS compared to the ECMS.
- The engine is operated more steadily with a lower average load power in the TTS.

Model Beta power profiles:

- There is a pure electric operation at low loads in both strategies.
- The engine charges the battery during all drive cycles in both strategies.
- The average engine load power is higher in the ECMS compared to the TTS, especially in the first three drive cycles.
- Less SSS is observed in the TTS compared to the ECMS.
- Hybrid operation is rarely observed in either strategy.
- The engine is operated more steadily with a lower average load power in the TTS.

The power profiles of the RTTS are compared against the ECMS in section 6.2.

6.1.2 SOC Profiles

The SOC profiles of the ECMS, TTS, and STTS for the model Alpha in the four standard driving cycles are presented in Figure 6.7. It is evident that the CS operation is achieved for both the ECMS and the TTS in all drive cycles. The TTS SOC profiles are generally smoother due to the engine charging the battery more steadily. When comparing the TTS to the ECMS profiles, the maximum deviation of the SOC from SOC_{init} is lower in the WL-L, fairly similar in the WL-M and the WL-H, and higher in the WL-E.

In terms of the STTS, it has comparable SOC profiles to the TTS in the WL-H and WL-E drive cycles. However, it is less CS than the TTS and the ECMS for the WL-L and WL-M.

The SOC profiles for the model Beta are shown in Figure 6.8 for the ECMS, TTS, and RTTS strategies for the four standard driving cycles. It is observed that both the ECMS and TTS achieve CS operation

in all drive cycles, with the RTTS demonstrating excellent CS performance as well, which is discussed in more detail in section 6.2.

In all cases, the final SOC is approximately equal to the initial SOC, and the SOC trajectory is steady and well within the boundaries, resulting in improved fuel economy and battery life. The TTS is capable of achieving CS operation without relying heavily on regenerative braking.

In the WL-H and WL-E drive cycles, the SOC deviation is smaller in the ECMS profiles than in the TTS profiles. However, all strategies achieve CS status.

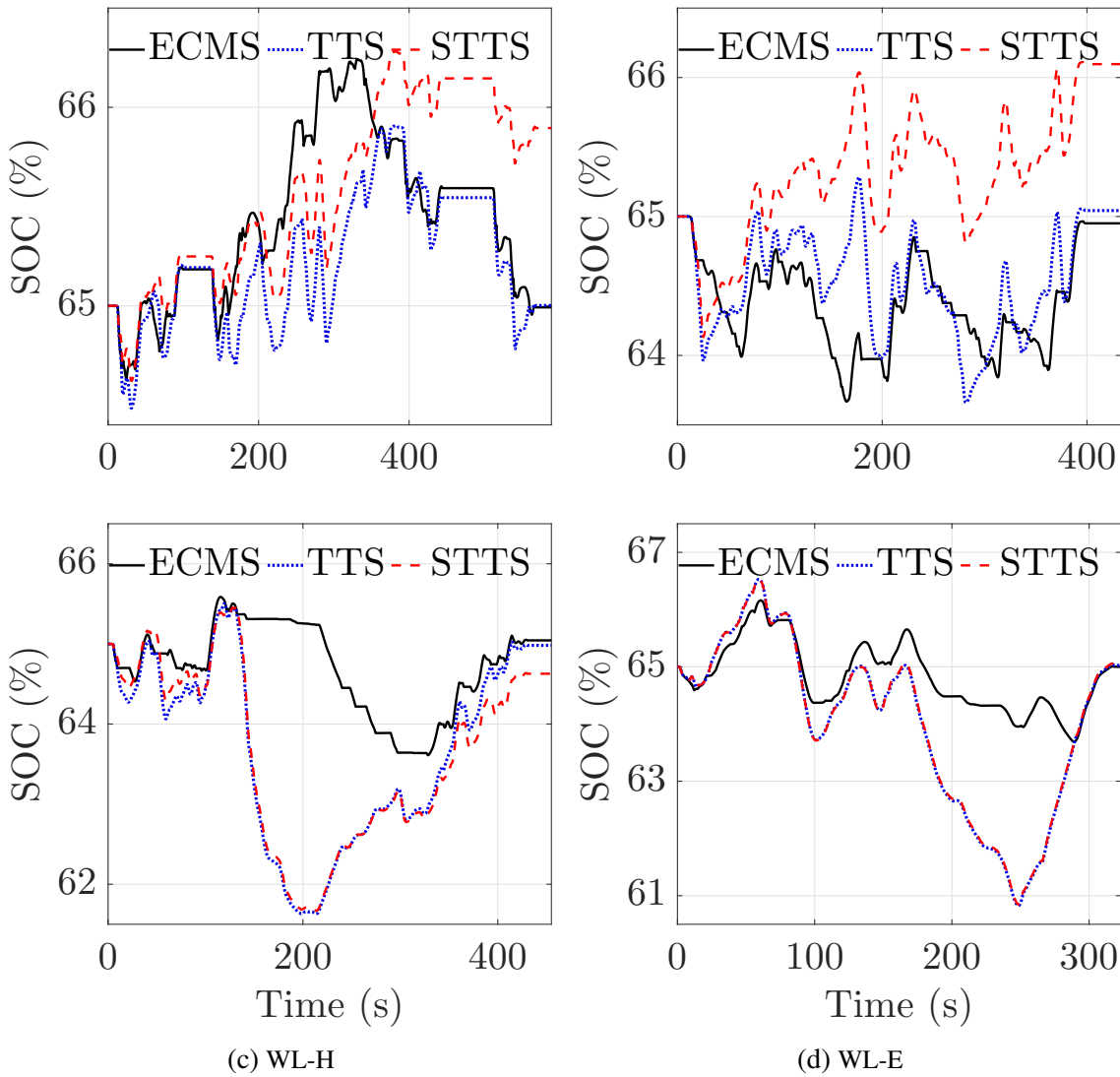


Figure 6.7: SOC time profiles of the ECMS, TTS and STTS for the first iteration of driving cycles WL-L (a), WL-M (b), WL-H (c), and WL-E (d). These plots are for the model Alpha.

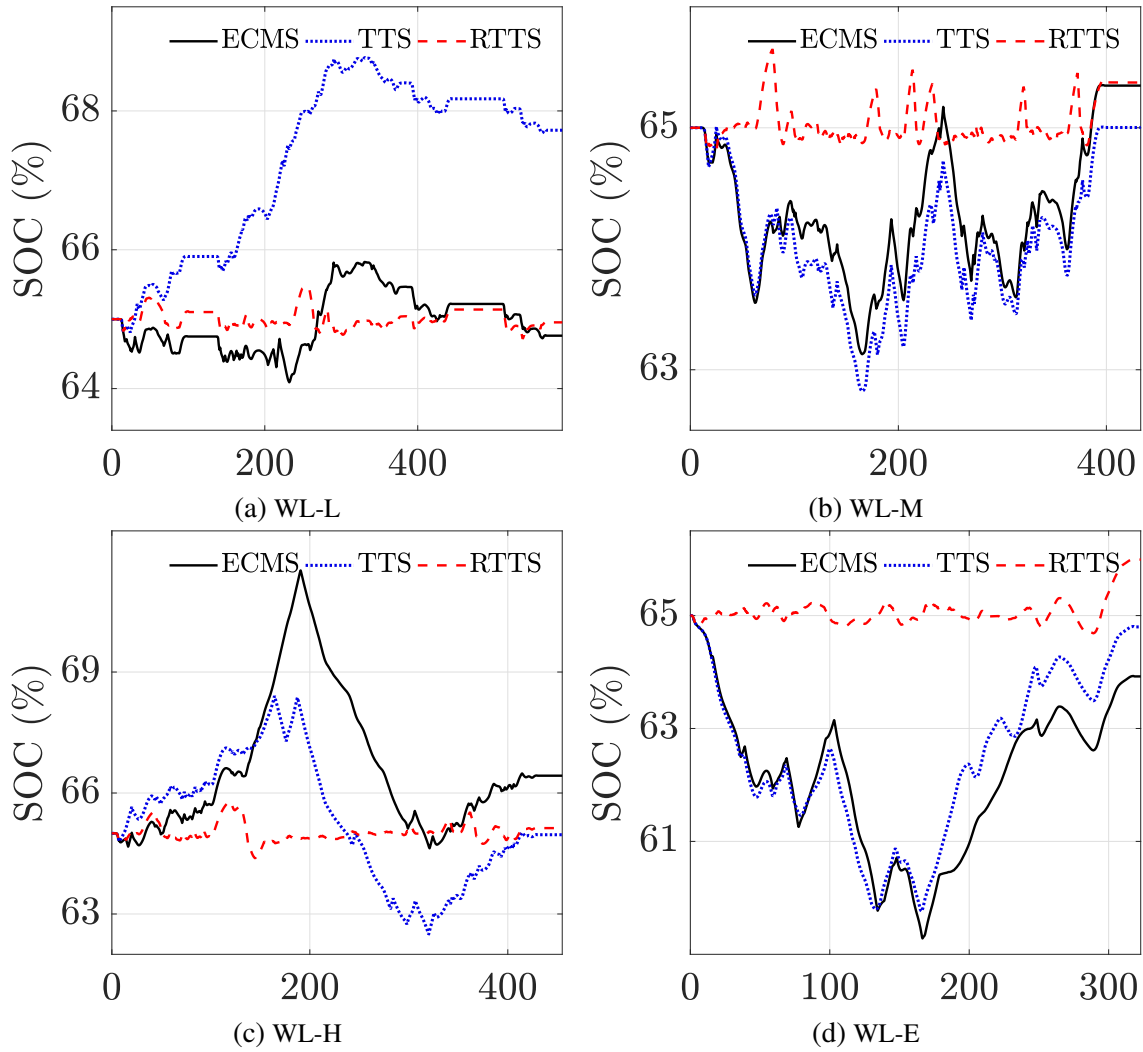


Figure 6.8: SOC time profiles of the ECMS, TTS and STTS for the first iteration of driving cycles WL-L (a), WL-M (b), WL-H (c), and WL-E (d). These plots are for the model Beta.

6.1.3 Fuel Economy

The Model Alpha fuel economy results for the ECMS, TTS and STTS are summarised in Table 6.1, Table 6.3, and Table 6.5, respectively. The model Beta economy results for the ECMS and the TTS are presented in Table 6.2 and Table 6.4, respectively.

The TTS fuel economy results are compared against the benchmark (i.e. ECMS) and visualised in Figure 6.9 and Figure 6.10.

Table 6.1: Fuel economy of the ECMS for the model Alpha

Driving cycle	$SOC_{final}(\%)$	m_f (kg)	m_{efc} (kg)	$\Delta ECMS(\%)$
WL-L	64.99	0.2073	0.2074	0
WL-M	64.99	0.2406	0.2407	0
WL-H	65.04	0.3234	0.3234	0
WL-E	65.13	0.4473	0.4460	0
WLTP	65.07	1.2176	1.2176	0

Table 6.2: Fuel economy of the ECMS for the model Beta

Driving cycle	$SOC_{final}(\%)$	m_f (kg)	m_{efc} (kg)	$\Delta ECMS(\%)$
WL-L	64.76	0.1118	0.1158	0
WL-M	65.37	0.1641	0.1591	0
WL-H	67.20	0.3088	0.2794	0
WL-E	63.97	0.4399	0.4529	0
WLTP	65.47	1.0136	1.0078	0

Table 6.3: Fuel economy of the TTS for the model Alpha

Driving cycle	$SOC_{final}(\%)$	m_f (kg)	m_{efc} (kg)	$\Delta ECMS(\%)$
WL-L	65.22	0.1971	0.1959	-5.55
WL-M	65.07	0.1619	0.1610	-8.48
WL-H	65.03	0.3060	0.3057	-4.67
WL-E	64.99	0.4455	0.4457	-0.07
WLTP	65.12	1.1788	1.1779	-3.26

Table 6.4: Fuel economy of the TTS for the model Beta

Driving cycle	$SOC_{final}(\%)$	m_f (kg)	m_{efc} (kg)	$\Delta ECMS(\%)$
WL-L	66.99	0.1152	0.1076	-7.08
WL-M	65.48	0.2231	0.2159	+3.57
WL-H	64.93	0.2771	0.2780	-0.47
WL-E	64.90	0.4431	0.4439	-1.99
WLTP	64.88	0.9976	0.9996	-3.71

Table 6.5: Fuel economy of the STTS for the model Alpha

Driving cycle	$SOC_{final}(\%)$	m_f (kg)	m_{efc} (kg)	$\Delta ECMS(\%)$
WL-L	64.93	0.1999	0.2007	-3.23
WL-M	65.04	0.2223	0.2220	-7.77
WL-H	65.00	0.3083	0.3083	-4.66
WL-E	65.05	0.4465	0.4461	+0.22
WLTP	65.08	1.1790	1.1784	-2.92

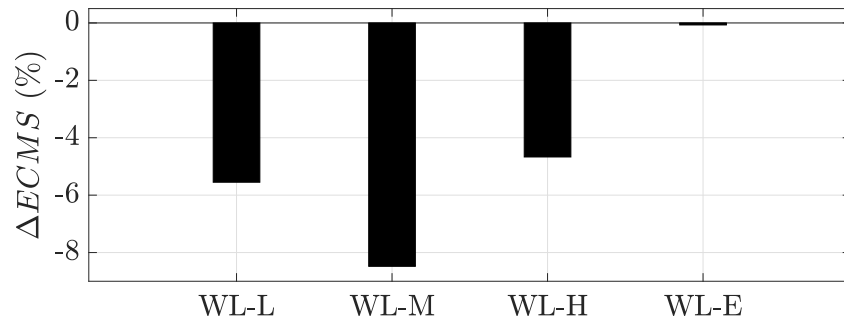


Figure 6.9: Comparison of the fuel economy of the TTS relative to the performance of the ECMS for the WL-L, WL-M, WL-H and WL-E drive cycles for the model Alpha.

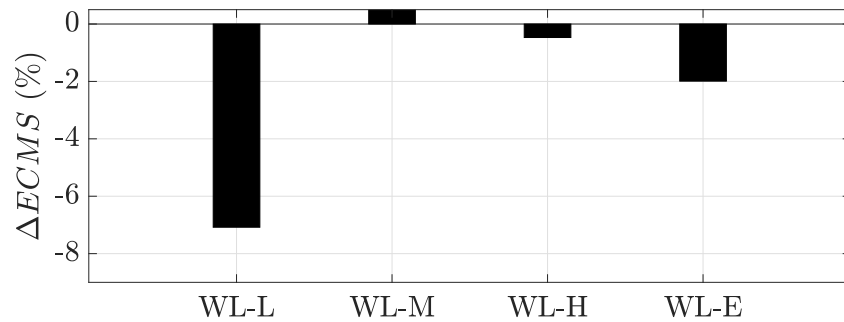


Figure 6.10: Comparison of the fuel economy of the TTS relative to the performance of the ECMS for the WL-L, WL-M, WL-H and WL-E drive cycles for the model Beta.

The results are encouraging as the design rules of the TTS are straightforward, and the tuning time is approximately 1.5 times faster than the ECMS. The TTS outperforms the ECMS by 0.07-8.48% in terms of the equivalent fuel consumption (m_{efc}) for the model Alpha and 0.47-3.71% for the model Beta. When considering the four drive cycles together (WLTP), the TTS achieves a 4.12% and 3.71% improvement over the ECMS for the model Alpha and model Beta, respectively.

6.2 Implementation of the RTTS and RSTTS

To demonstrate the effectiveness of the proposed RTTS, this method is implemented on the TTR HEV model Alpha and Beta over the WLTP (WL-L, WL-M, WL-H and WL-E) as well as over a drive cycle measured experimentally by a data acquisition device [125], representing a real-driving cycle in a rural road in London presented in Figure 6.11. The RTTS is implemented on the Alpha and Beta models and then benchmarked against the ECMS. The RSTTS is only implemented on the model Alpha as it was realised in subsection 6.1.3 that the TTS achieved a better fuel economy as well as 1.5 times less tuning and implementation time compared to the ECMS; Therefore, the trade-off of tuning-time and fuel economy was in favour of the TTS over the ECMS.

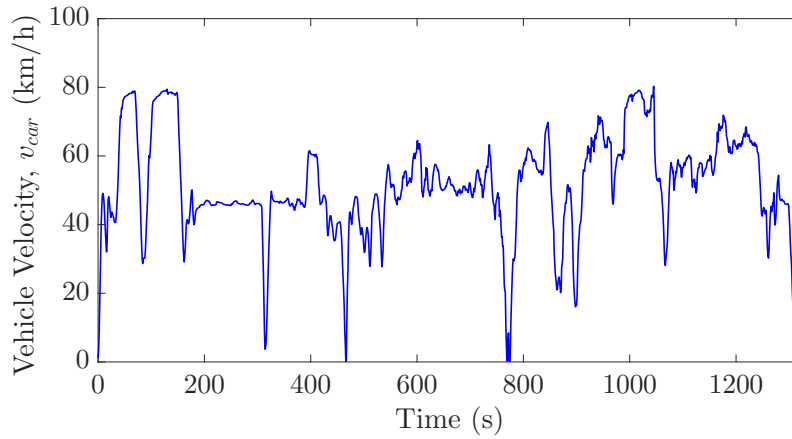


Figure 6.11: The Experimental drive cycle collected in London.

6.2.1 Power Profiles

The resulting power profiles of the ECMS and the RTTS for both models over the WLTP and the Experimental drive cycle are presented in Figure 6.12 and Figure 6.13. Only the power profiles of the ICE and the propulsion load are visualised since the power in the motor branch is determined by the given ICE power. The power profiles of the ECMS and the RTTS for model alpha are shown in Figure 6.14, which exhibits very similar performance to RTTS. The operation of the RTTS and RSTTS are generally similar to the TTS. The only difference in the real-time versions is the slightly higher average engine power over the WL-H and WL-E drive cycles. The engine activation pattern is fairly similar in both cases.

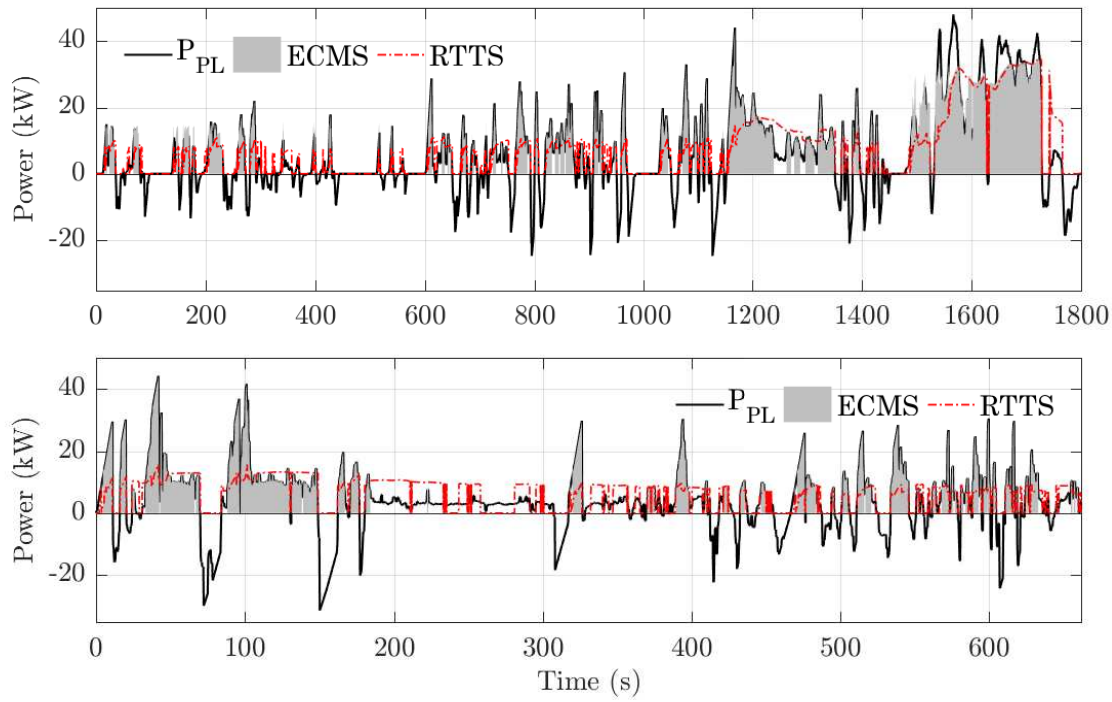


Figure 6.12: Power profiles of the engine and the propulsion load of the ECMS and the RTTS over the WLTP (top) and the Experimental drive cycle (bottom) for the model Alpha.

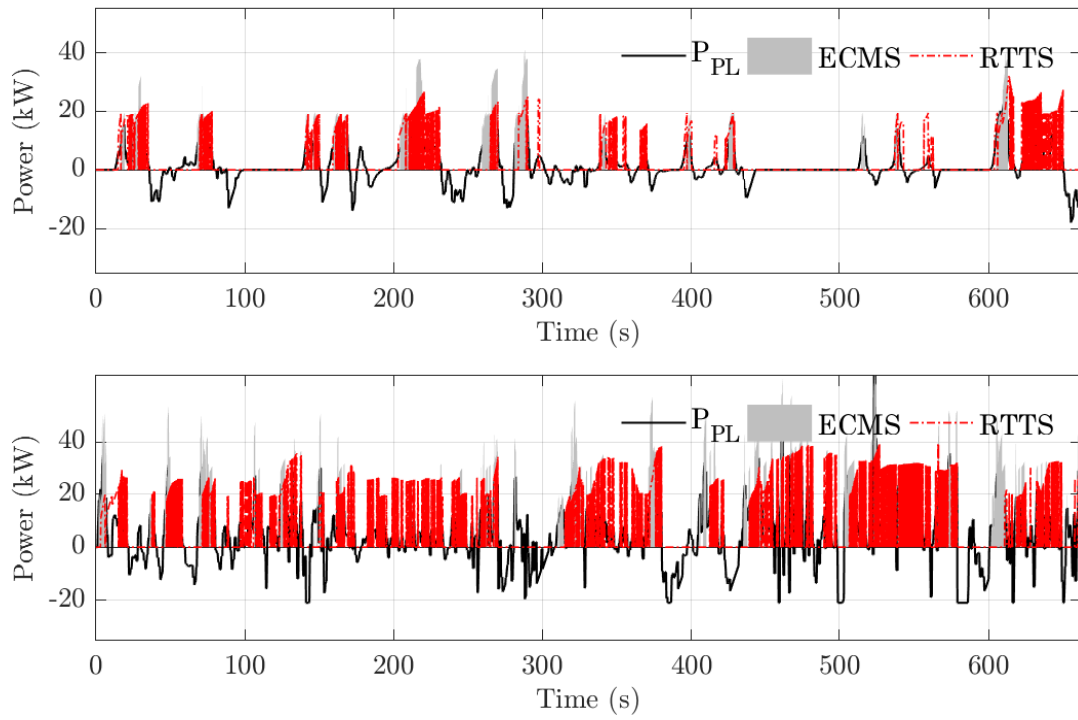


Figure 6.13: Power profiles of the engine and the propulsion load of the ECMS and the RTTS over the WLTP (top) and the Experimental drive cycle (bottom) for the model Beta.

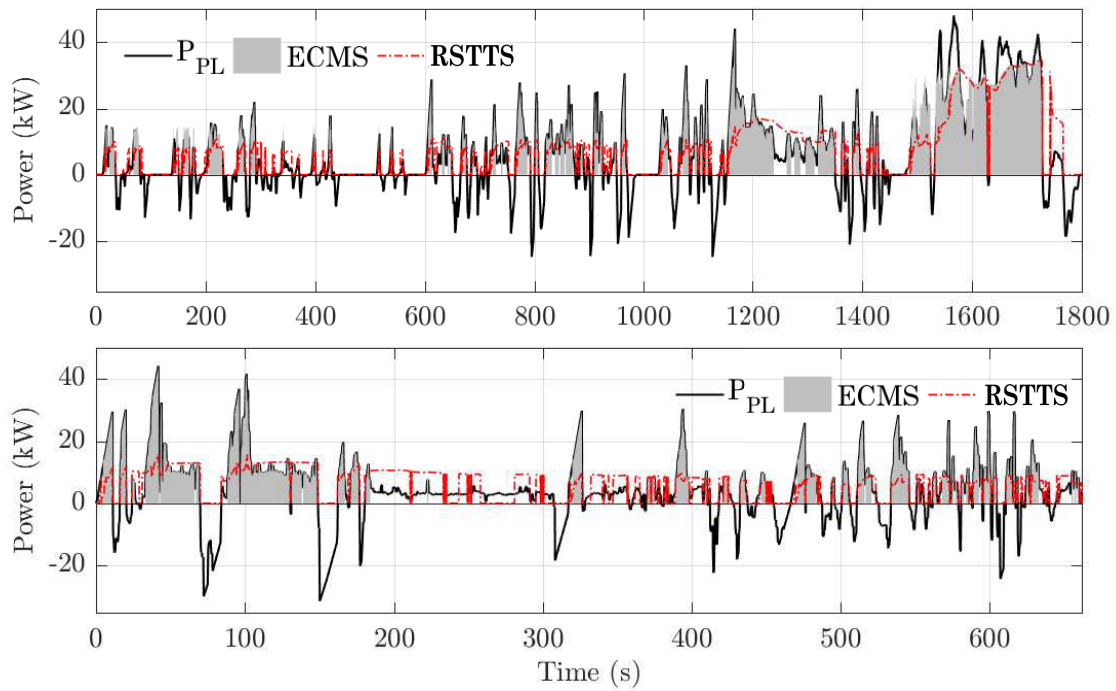


Figure 6.14: Power profiles of the engine and the propulsion load of the ECMS and the RSTTS over the WLTP (top) and the Experimental drive cycle (bottom) for the model Alpha.

6.2.2 Torque Profiles

The RTTS engine torque over the WLTP and the Experimental driving cycle can be seen in Figure 6.15 and Figure 6.16 for models Alpha and Beta, respectively. For both models, it is observed that the engine torque value does not deviate more than approximately 5 Nm from the corresponding T_e^{pr} in Equation 5.3.1, and the various torque levels are visible. The Experimental driving cycle is treated as a combination of the WL-M and WL-H drive cycles, which was expected since the average velocity in the Experimental drive cycle is between the average velocities of the WL-M and WL-H. The ICE activation frequency exceeds the ECMS case over the Experimental driving cycle. However, the average engine power is lower, and the ICE is operated more continuously. The engine torque variation is very smooth and includes relatively constant torque levels, which seem more effective than frequent spikes of high magnitude. The RSTTS engine torque variation over the WLTP and the Experimental driving cycle for model Alpha is visualised in Figure 6.17, which exhibits reasonably similar operation to the RTTS.

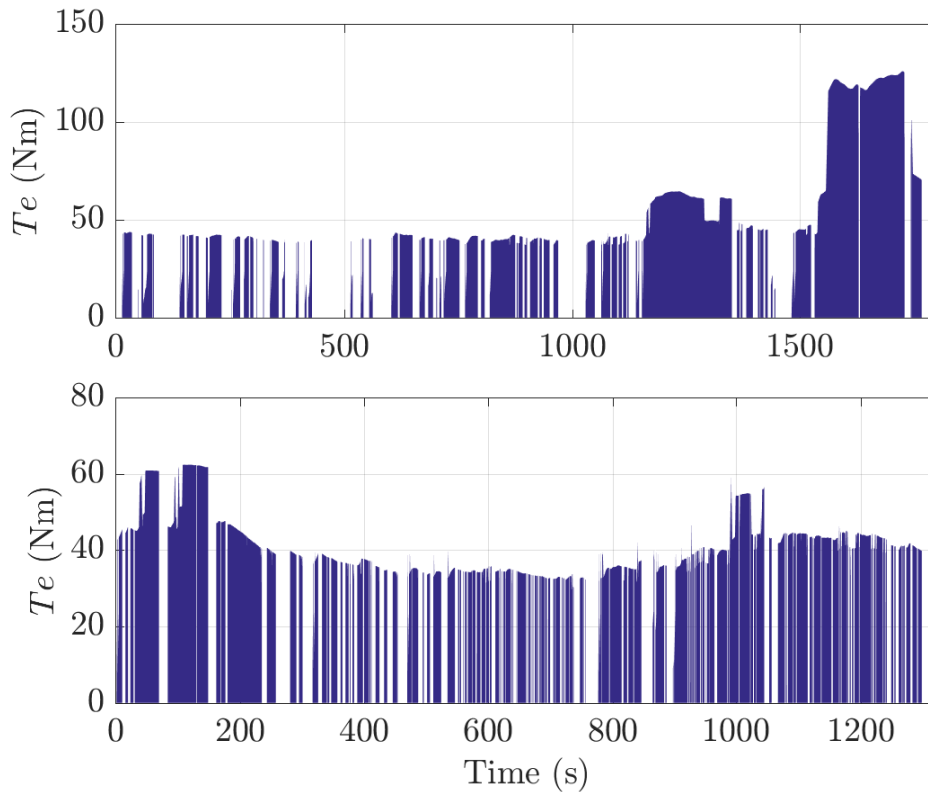


Figure 6.15: RTTS engine torque T_e , over the WLTP (top) and the Experimental drive cycle (bottom) for the model Alpha.

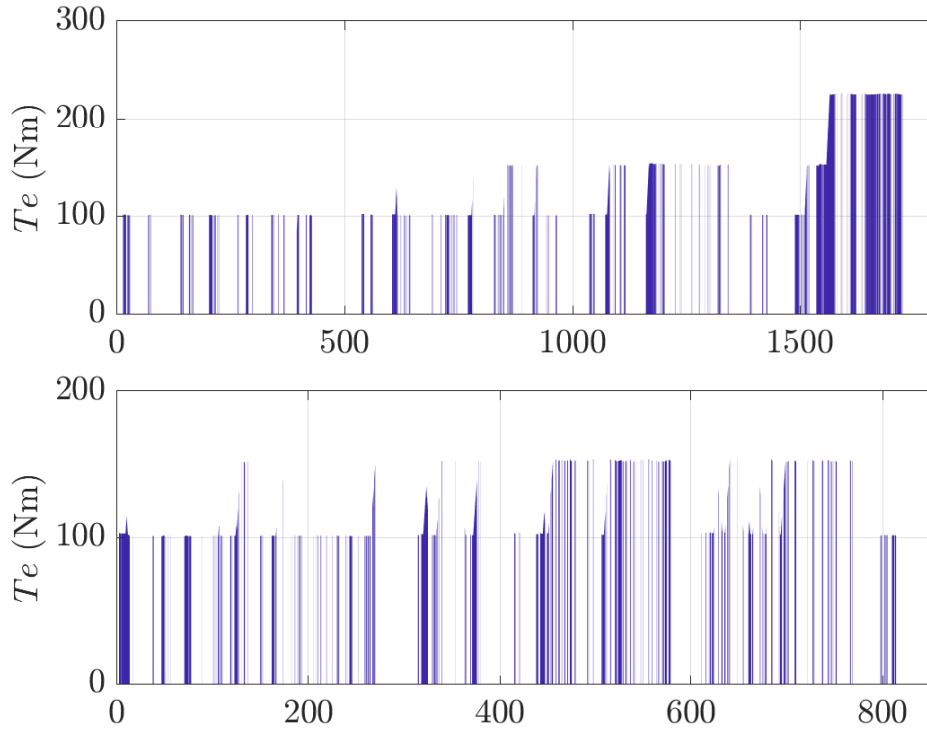


Figure 6.16: RTTS engine torque T_e , over the WLTP (top) and the Experimental drive cycle (bottom) for the model Beta.

6.2.3 SOC Profiles

The SOC profiles of the ECMS, RTTS, and RSTTS for model Alpha are shown in Figure 6.18, while the SOC profiles of the ECMS and RTTS for model Beta are displayed in Figure 6.19. When driving the WLTP with both models, it can be seen that during the first half of the drive cycle, the SOC profiles' variations for the ECMS and the RTTS are quite similar. However, during the second half of the drive cycles, the RTTS SOC variation is greater than that of the ECMS because the RTTS average engine power is lower, and a hybrid mode operation is often adopted. Nonetheless, since the RTTS ICE activation frequency is higher than the ECMS, the CS operation is still achieved by the RTTS.

The SOC profile of the RSTTS exhibits a similar trend to the ECMS for the WLTP drive cycle. However, the RSTTS SOC profile for the Experimental drive cycle demonstrates a more significant SOC deviation compared to the RTTS. Overall, the RTTS achieved a better CS operation than the RSTTS.

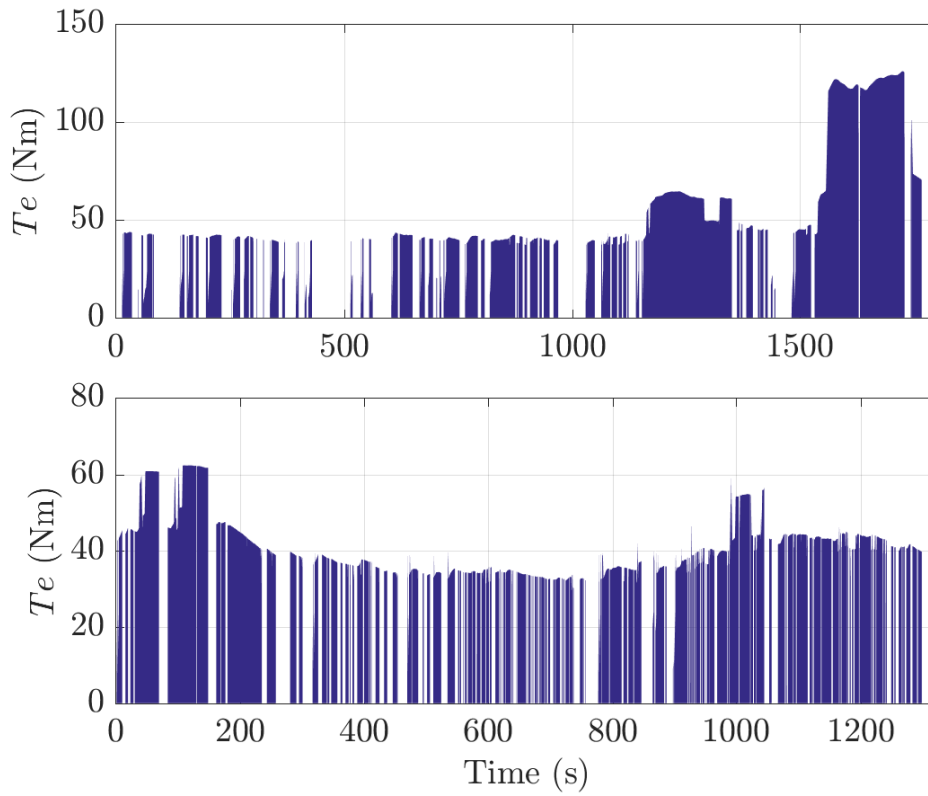


Figure 6.17: RSTTS engine torque T_e , over the WLTP (top) and the Experimental drive cycle (bottom) for the model Alpha.

6.2.4 Fuel Economy

The fuel economy and final SOC results of the ECMS and the RTTS for both the model Alpha and the model Beta over the WLTP and the Experimental drive cycle are summarised in Tables 6.6-6.10. In the model Alpha, the RTTS outperforms the ECMS by 2.80% and 5.82% in terms of the equivalent fuel consumption (m_{efc}) over the WLTP and the Experimental drive cycle, respectively. For the model Beta, the RTTS outperforms the ECMS by 2.68% and 2.26% during the WLTP and the Experimental drive cycle, respectively. These results demonstrate the effectiveness of the proposed RTTS in achieving improved fuel economy while maintaining the final SOC of the battery. The fuel economy and final SOC results of the ECMS and the RSTTS for the model Alpha over the WLTP and the Experimental drive cycle are summarised in Table 6.8, which demonstrates a 2.57% and 6.47% improvement over the ECMS during the WLTP and the Experimental drive cycle, respectively.

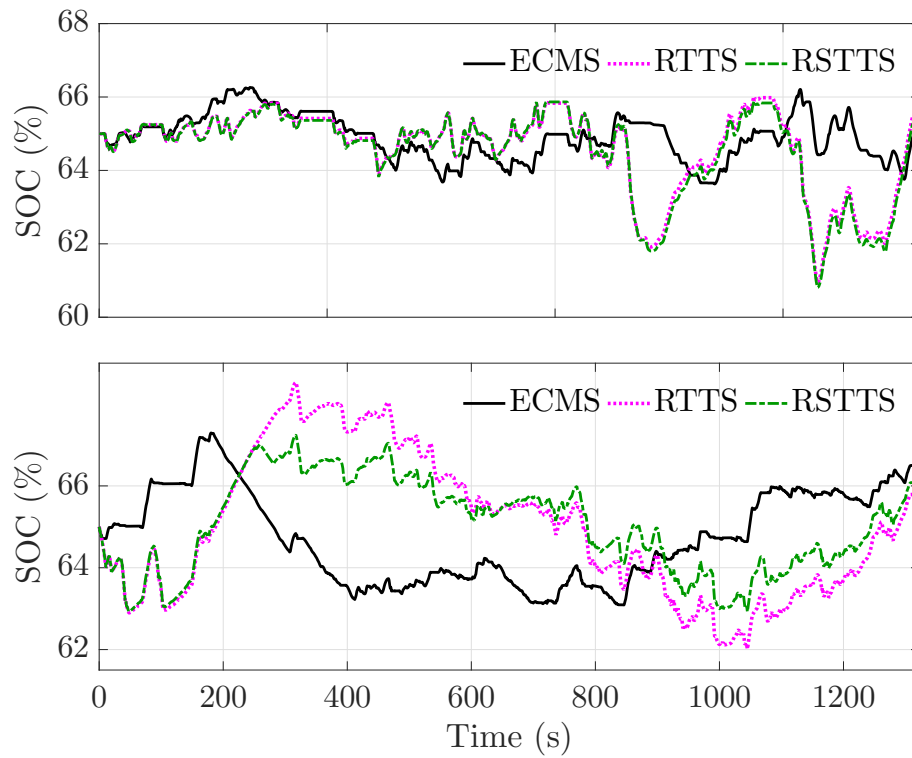


Figure 6.18: SOC profiles of the ECMS, RTTS and the RSTTS over the WLTP (top) and the Experimental drive cycle (bottom) for the model Alpha.

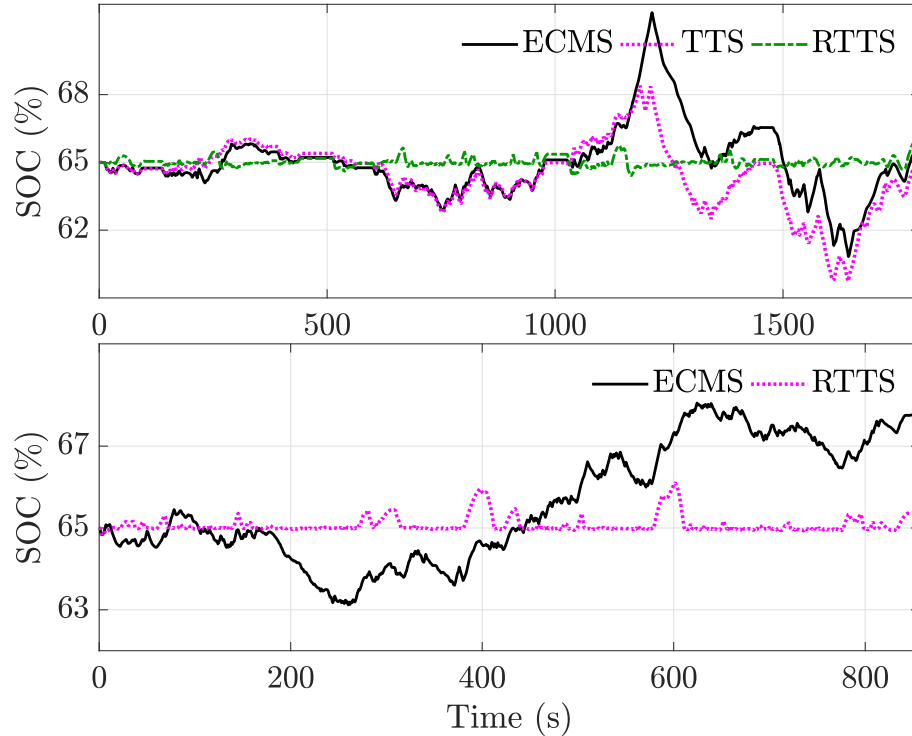


Figure 6.19: SOC profiles of the ECMS and the RTTS over the WLTP (top) and the Experimental drive cycle (bottom) for the model Beta.

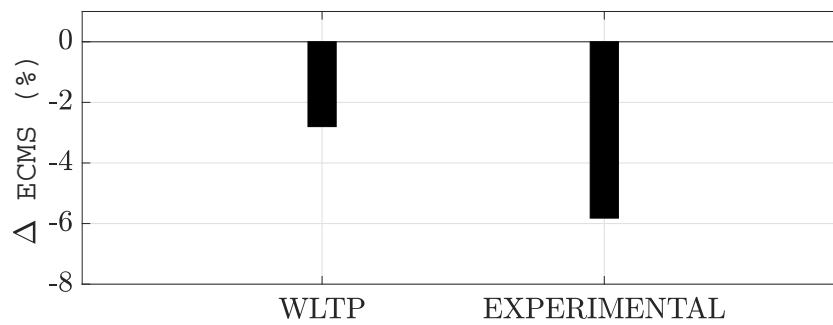


Figure 6.20: Comparison of the fuel economy of the RTTS relative to the performance of the ECMS over the WLTP and the Experimental driving cycles for the model Alpha.

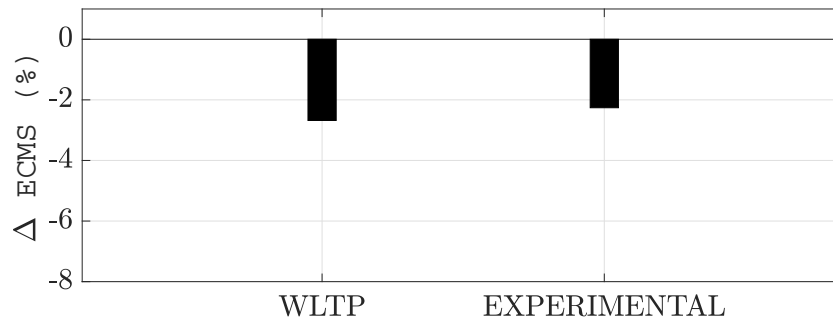


Figure 6.21: Comparison of the fuel economy of the RTTS relative to the performance of the ECMS over the WLTP and the Experimental driving cycles for the model Beta.

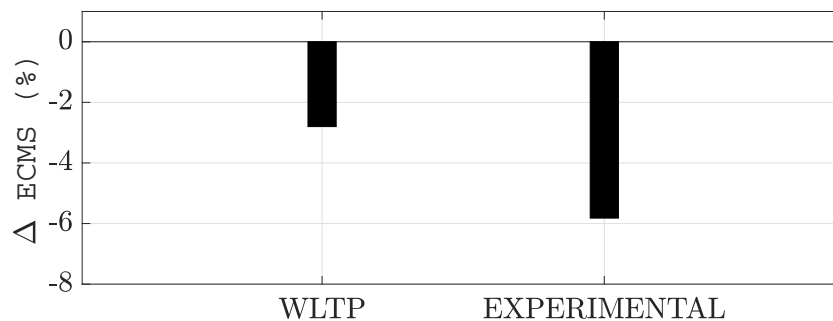


Figure 6.22: Comparison of the fuel economy of the RSTTS relative to the performance of the ECMS over the WLTP and the Experimental driving cycles for the model Alpha.

Table 6.6: Fuel economy of the ECMS over the WLTP and the Experimental drive cycle for the model Alpha

Driving cycle	$SOC_{final}(\%)$	m_f (kg)	m_{efc} (kg)	$\Delta ECMS(\%)$
WLTP	65.07	1.2176	1.2176	0
Experimental drive cycle	66.41	0.8972	0.8894	0

Table 6.7: Fuel economy of the RTTS over the WLTP and the Experimental drive cycles for the model Alpha

Driving cycle	$SOC_{final}(\%)$	m_f (kg)	m_{efc} (kg)	$\Delta ECMS(\%)$
WLTP	65.58	1.1790	1.1835	-2.80
Experimental drive cycle	65.94	0.8376	0.8324	-5.82

Table 6.8: Fuel economy of the RSTTS over the WLTP and the Experimental drive cycles for the model Alpha

Driving cycle	$SOC_{final}(\%)$	m_f (kg)	m_{efc} (kg)	$\Delta ECMS(\%)$
WLTP	65.61	1.1910	1.1863	-2.57
Experimental drive cycle	65.61	0.8359	0.8319	-5.47

Table 6.9: Fuel economy of the ECMS over the WLTP and the Experimental drive cycles for the model Beta

Driving cycle	$SOC_{final}(\%)$	m_f (kg)	m_{efc} (kg)	$\Delta ECMS(\%)$
WLTP	65.47	1.0136	1.0077	0
Experimental drive cycle	67.06	0.4156	03809	0

Table 6.10: Fuel economy of the RTTS over the WLTP and the Experimental drive cycles for the model Beta

Driving cycle	$SOC_{final}(\%)$	m_f (kg)	m_{efc} (kg)	$\Delta ECMS(\%)$
WLTP	65.58	1.1790	1.1835	-2.68
Experimental drive cycle	65.922	0.3752	0.3723	-2.26

6.3 Chapter Summary

In this chapter, the conventional optimisation-based method ECMS was implemented on both TTR models (Alpha and Beta). The ECMS fuel economy was then used as a benchmark to evaluate the performance of the heuristic method TTS. It was realised that the TTS outperformed the ECMS over all four segments of the WLTP (i.e. WL-L, WL-M, WL-H, and WL-E) in the model Alpha's simulations, ranging from 0.07% to 8.48%, and over the WLTP by 3.26%. The model Beta's simulations showed that the TTS outperformed the ECMS in three out of the four components of the WLTP and outperformed the ECMS over the WLTP by 3.71%. The SOC profiles in Figure 6.8 demonstrated that the TTS achieved a more consistent CS operation and a better fuel economy than the ECMS.

Since the performance of the TTS was found to be more reliable and robust compared to the STTS, the STTS was not implemented on the model Beta. The STTS outperformed the ECMS for all drive cycles in the model Alpha simulations apart from the WL-E; the STTS outperformed the ECMS over the WLTP by 2.92%.

To demonstrate the effectiveness of the proposed RTTS, this strategy was implemented on the TTR HEV models Alpha and Beta when driving the WLTP and a drive cycle measured experimentally in London.

The RTTS outperformed the ECMS by 2.80% over the WLTP and by 5.82% over the Experimental drive cycle for the model Alpha. The RTTS outperformed the ECMS by 2.68% over the WLTP and by 2.26% over the Experimental drive cycle for the model Beta.

Additionally, it was deduced from the ECMS and the RTTS power profiles over the WLTP and the Experimental drive cycle that the operation of the RTTS was generally similar to the TTS. The only difference in the RTTS was the slightly higher average engine power in the WL-H and WL-E drive cycles.

The RSTTS exhibited similar operation to RTTS with relatively similar fuel economy and CS operation. However, the RTTS outperformed RSTTS, showing more robustness while having only slightly longer tuning time compared to the RTTS, especially over the Experimental driving cycle.

Part III

Energy Management of EVs

Chapter 7

Electric Vehicle Model

This chapter describes the development of a low-fidelity dual-motor EV, later used in the DP framework in Chapter 8. The thermal dynamics of the PMSMs are also modelled and described in this chapter. The Baseline and Thermal models are presented in section 7.1 and section 7.2, respectively. The Thermal model includes the thermal dynamics of the PMSMs, which is not present in the Baseline model.

In the subsequent parts of this work, the subscript F refers to the front axle (e.g. front motor) and the subscript R refers to the rear axle (e.g. rear motor).

The overall architecture of the dual-motor EV is depicted in Figure 7.1.

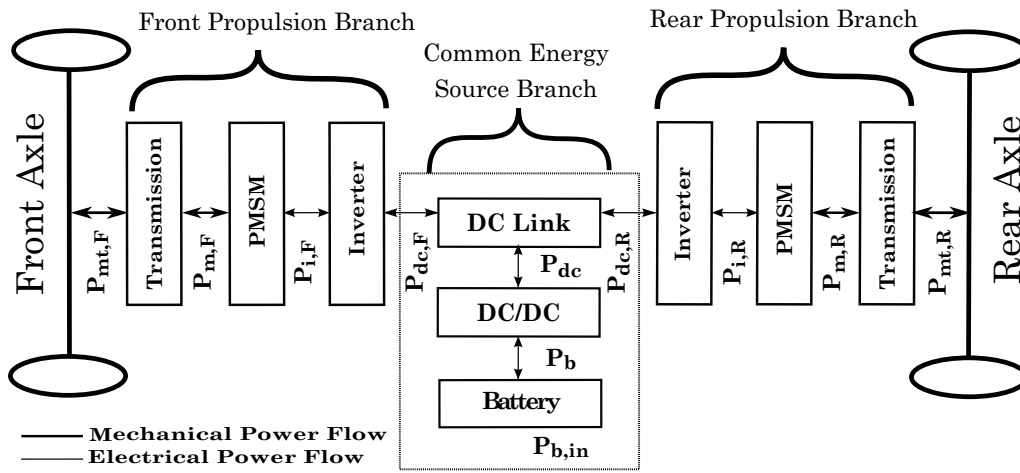


Figure 7.1: Overall architecture of the dual-motor EV.

7.1 Baseline EV Model

The Baseline battery model is presented in this section according to [120,126]. A novel feature of this EV model is the utilisation of two electric motors with different power ratings in the powertrain instead of one. The energy consumption of this dual-motor EV can be well-captured using a quasi-static discrete-time model. Specifically, the PMSMs are modelled using electric-power maps derived from detailed simulations and dyno tests conducted by the industrial partner. The battery is modelled as a voltage source with a resistance in series, and the vehicle model includes air drag, rolling friction, and inertial forces. Additionally, the transmission system is a two-speed gearbox model with a constant efficiency of 95%, which does not account for gear change transient response.

7.1.1 Battery Model

An equivalent circuit model has been used for the battery. The battery voltage is:

$$V_b = E_b - R_b I_b \quad (7.1)$$

with I_b being the average current drawn from the battery, R_b being the internal resistance and E_b being the open circuit voltage.

The battery power is defined as:

$$P_b = V_b I_b, \quad (7.2)$$

By replacing Equation 7.1 in Equation 7.2:

$$(E_b - R_b I_b) I_b = P_b, \quad (7.3)$$

where the open circuit voltage E_b is a tabulated function of the SOC. By solving I_b with respect to E_b , R_b , and P_b we have:

$$I_b = \frac{E_b - \sqrt{E_b^2 - 4P_b R_b}}{2R_b} \quad (7.4)$$

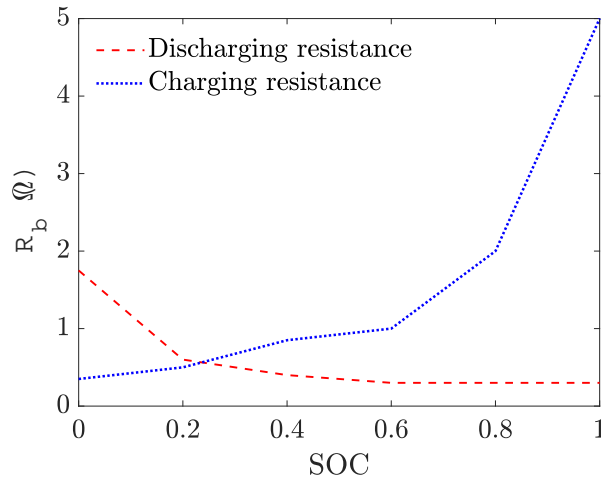


Figure 7.2: Internal battery resistance as a function of SOC.

The battery's internal power is defined as:

$$P_{b,in} = E_b I_b \quad (7.5)$$

The battery SOC represents the only state in the DP method used in section 8.2 and one of the three states in subsection 8.3.1, governed by:

$$\frac{d}{dt}(SOC) = -\frac{I_b(SOC, P_b)}{Q_{max}}. \quad (7.6)$$

The battery parameters are summarised in Table 7.1.

Table 7.1: Li-on battery parameters

Parameter	Symbol	Value
Rated capacity	Q_{max}	60 Ah
Nominal voltage	V_{nom}	375 V
Initial state of charge	SOC_{init}	80%
Battery constant voltage	E_0	320 V
Nominal Internal resistance	$R_{b,nom}$	0.356 Ω
Battery maximum power	$P_{b,max}$	56 kW
Battery minimum power	$P_{b,min}$	-41 kW

The battery internal resistance R_b , and the open-circuit voltage E_b , are not constant; both vary as a function of SOC. These data are provided by the industrial partner and are depicted in Figure 7.2 and Figure 7.3, respectively.

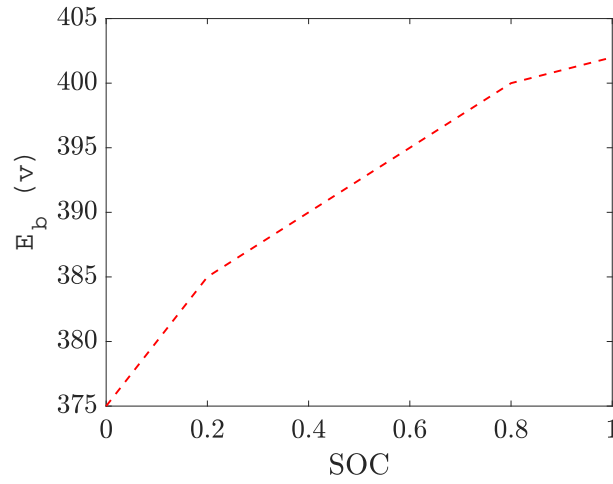


Figure 7.3: Battery open circuit voltage as a function of SOC.

7.1.2 DC-DC Converter

The bidirectional DC-DC converter used in the model connects the battery to the common DC link between the two PMSMs and increases the battery voltage to a higher level. This backward-facing modelling approach does not address the high-frequency dynamics of the DC-DC converter. The power flow in the DC-DC converter is as follows:

$$P_{dc} = \sum_{j \in [F, R]} \eta_{dc}^{\text{sign}(P_{dc,j})} P_b \quad (7.7)$$

where $P_{dc,j}$ is the axle-specific input power, which flows into the DC link and $\eta_{dc}=0.96$ is the constant discharging efficiency for the front and the rear axles.

7.1.3 DC Link

The front and the rear PMSMs are both connected to a common 370V DC link, each through a bi-directional inverter:

$$P_{dc} = P_{dc,F} + P_{dc,R} \quad (7.8)$$

7.1.4 Inverter

For simplification purposes, the inverter efficiency across various load powers is assumed to be a constant efficiency of $\eta_i=0.96$ for both motors.

$$P_{i,j} = \eta_i^{\text{sign}(P_{dc,j})} P_{dc,j}, \quad (7.9)$$

where $P_{i,j}$ is the output power of the respective inverter (i.e. front or rear).

7.1.5 Permanent Magnet Synchronous Motor (PMSM)

In the present work, the maximum speed of both PMSMs is 8700 rpm, and the maximum output torque of the front and the rear PMSMs are 200 Nm and 350 Nm, respectively.

The PMSM model is a 3-phase star-connected motor. The detailed dynamics described by the standard 2-phase d - q rotating reference frame, [6], are as follows:

$$\frac{di_{d,j}}{dt} = (v_{d,j} - R_{m,j} i_{d,j} + p_{m,j} \omega_{m,j} L_{q,j} i_{q,j}) / L_{d,j} \quad (7.10)$$

$$\frac{di_{q,j}}{dt} = (v_{q,j} - R_{m,j} i_{q,j} + p_{m,j} \omega_{m,j} (L_{d,j} i_{d,j} + \lambda_{m,j})) / L_{q,j} \quad (7.11)$$

where $\omega_{m,j}$ is the axle-specific rotor speed, $v_{d,j}$ and $v_{q,j}$ are the direct and quadrature components of the stator voltage, $i_{d,j}$ and $i_{q,j}$ are the direct and quadrature components of the stator current, $L_{d,j}$ and $L_{q,j}$ are the direct and quadrature components of the stator inductance, $R_{m,j}$ is the stator resistance, and $p_{m,j}$ is the number of pole pairs. The inertia torque is described by:

$$J_{m,j} \frac{d\omega_{m,j}}{dt} = T_{em,j} + T_{m,j} + T_{dm,j} \quad (7.12)$$

where J_m is the rotor inertia, $T_{dm,j}$ is the dissipation torque, $T_{em,j}$ is the electromagnetic torque, and $T_{m,j}$ is the load torque [110]. The electromagnetic torque is given by:

$$T_{em,j} = \frac{3}{2} p_{m,j} (\lambda_{m,j} i_{q,j} + (L_{d,j} - L_{q,j}) i_{d,j} i_{q,j}) \quad (7.13)$$

and the dissipation torque T_{dm} is described as:

$$T_{dm,j} = -1 - 2 \times 10^{-5} \omega_{m,j}^2 \quad (7.14)$$

The electrical power $P_{i,j}$ and the mechanical power $P_{m,j}$ are:

$$P_{i,j} = \frac{3(V_{q,j}i_{q,j} + v_{d,j}i_{d,j})}{2} \quad (7.15)$$

$$P_{m,j} = T_{m,j}\omega_{m,j} \quad (7.16)$$

Since the inertia torque $J_{m,j}\frac{d\omega_{m,j}}{dt}$ is relatively small compared to the load torque $T_{m,j}$, and the currents have fast dynamics, Equations 7.10, 7.11 and 7.12 are only considered in steady-state. It is assumed that $L_{d,j} = L_{q,j}$ and $i_{d,j} = 0$. Therefore, the electrical power can be expressed as:

$$P_{i,j} = -\omega_{m,j}(T_{m,j} + T_{dm,j}) + \frac{2}{3}R_{m,j}\frac{(T_{m,j} + T_{dm,j})^2}{p_{m,j}^2\lambda_j^2} \quad (7.17)$$

which equates the motor efficiency to:

$$\eta_{m,j}(T_{m,j}\omega_{m,j}) = \left(\frac{P_{m,j}}{P_{i,j}}\right)^{\text{sign}(P_{i,j})} \quad (7.18)$$

where the motor efficiency depends on $T_{m,j}$ and $\omega_{m,j}$. These parameters are visualised for the front and rear motors in Figure 7.4. The front and rear max continuous motor powers are 39 kW and 88 kW, with a maximum torque of 200 Nm and 350 Nm, respectively. The maximum speed is 8700 rpm for both motors. The front and rear PMSM parameters are presented in Table 7.2.

Table 7.2: Front and Rear PMSM parameters

Parameter	Axle	Symbol	Value
Maximum torque	Front	$T_{mmax,F}$	200 Nm
Maximum power	Front	$P_{mmax,F}$	39 kW
Maximum Speed	Front	$\omega_{mmax,F}$	8700 rpm
Moment of Inertia	Front	$J_{m,F}$	0.037 kgm ²
Stator resistance	Front	$R_{m,F}$	0.029 Ω
Number of pole pairs	Front	$p_{m,F}$	6
Rotor magnetic flux	Front	$\lambda_{m,F}$	0.125 Wb
Maximum torque	Rear	$T_{mmax,R}$	350 Nm
Maximum power	Rear	$P_{mmax,R}$	88 kW
Stator resistance	Rear	$R_{m,R}$	0.029 Ω
Maximum Speed	Rear	$\omega_{mmax,R}$	8700 rpm
Moment of Inertia	Rear	$J_{m,R}$	0.14 kgm ²
Number of pole pairs	Rear	$p_{m,R}$	6
Rotor magnetic flux	Rear	$\lambda_{m,R}$	0.125 Wb

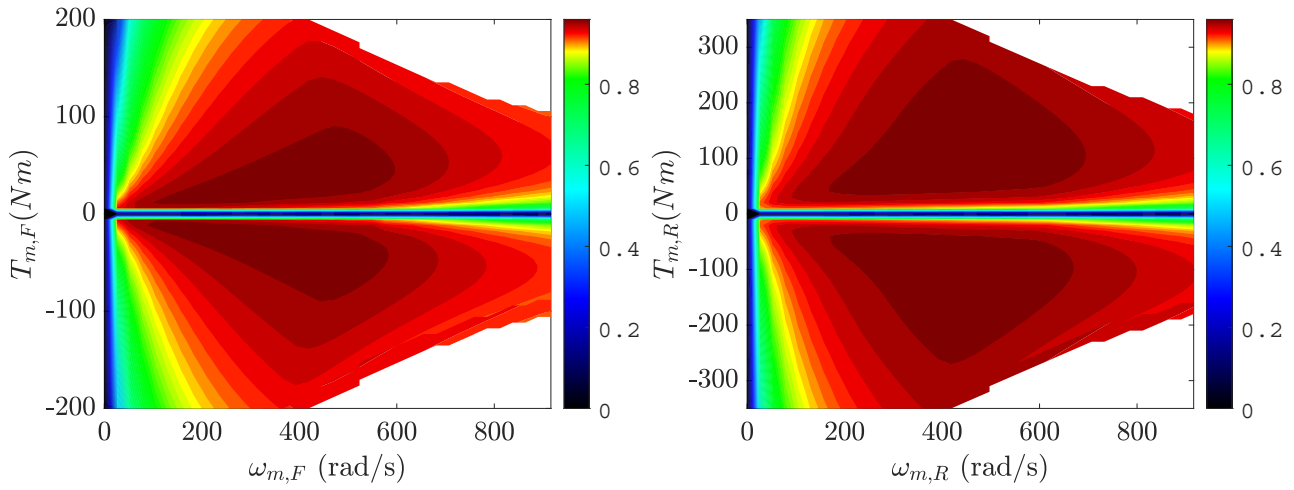


Figure 7.4: PMSM steady-state power efficiency maps for the variations in the front PMSM load torque $T_{m,F}$, and the front rotor speed $\omega_{m,F}$ (left); the rear PMSM load torque $T_{m,R}$, and the rear rotor speed $\omega_{m,R}$ (right). As only the forward vehicle motion is considered in this work, the rotor speed is always non-negative, and the PMSM has two modes of operation: 1) positive torque (motoring) and 2) negative torque (regenerating). The contours correspond to constant efficiencies.

Motor Transmission

The rear and front PMSMs are mechanically connected to the rear and front axles via a two-speed transmission. The transmission systems at the front and rear axles are identical. The motor's angular speed (ω_m) is determined by the vehicle wheel speed (ω_{wheel}) according to the following formula:

$$T_{mt,j} = \frac{T_{m,j}}{g_m} \quad (7.19)$$

$$\omega_{m,j} = g_m \omega_{wheel} \quad (7.20)$$

with $j \in [F, R]$ denoting the front and rear axles, respectively, $g_m = [12.49 \ 9.58]$ with the shifting speed threshold being 50 km/h. The gear changes through the drive cycle used in this work are visualised in Figure 8.1. The gear ratios and the fixed gearbox efficiency are identical for both front and rear transmissions. In this EV model, the transmission efficiency is assumed to be $\eta_t = 0.96$ for both axles. The following equation describes the power transmission:

$$P_{mt,j} = P_{m,j} \eta_t^{\text{sign}(P_{m,j})} \quad (7.21)$$

where $P_{m,j} = \omega_{m,j} T_{m,j}$ is the mechanical motor power, and $P_{mt,j}$ is the electrical driving power of the specific axle.

7.2 Thermal EV Model

This section describes the model incorporating the thermal dynamics of the PMSMs, used in subsection 8.3.1 for executing the Thermal DP. The battery, DC-DC converter, DC link, Inverter, and motor transmission models are identical between the Baseline and Thermal models. The main difference between these two models is the added thermal dynamics of the PMSMs in the EV model.

7.2.1 Thermal Dynamic Modelling of the PMSMs

The internal temperature rise strongly influences the performance of the PMSMs. This is mainly because the resistance of the stator windings and the magnet remanence depend on the temperature. In cases where the temperature rise is significant, it can lead to irreversible demagnetisation of the permanent magnet. Therefore, it is essential to monitor/estimate the temperature of the different nodes of electric motors to ensure safety and reasonable efficiency [127]. The efficiency maps provided by the industrial partner at six different temperatures are visualised in Figure 7.5 and Figure 7.6, for the front and rear PMSMs, respectively. It can be seen that the efficiency maps at various temperatures are different; exploiting this characteristic, the temperature is considered as a state in the optimal control formulation in Chapter 8.

According to [12], the battery loss is negligible compared to the losses in the electric motors. The energy demand from the SOC does not change significantly at different temperatures. For this reason, a fixed non-temperature-dependent efficiency has been chosen for the battery model in subsection 3.3.1; however, since SOC is dependent on the front and rear motor powers, it is indirectly affected by temperature. The total power losses for both PMSMs have been computed according to [12]:

$$P_{L,j} = P_{Cu,j} + P_{Fe,j} \quad (7.22)$$

where $P_{Cu,j}$ is the axle-specific copper loss and $P_{Fe,j}$ denotes the axle-specific rotor iron loss.

$$P_{Cu,j} = 3R_{ph,j}I_{rms,j}^2 \text{ with } R_{ph,j} = \rho_{Cu,j} \frac{l_{w,j}}{S_{w,j}} \quad (7.23)$$

where $I_{rms,j}$ is the axle-specific motor RMS current, θ_0 is the ambient temperature, and $R_{ph,j}$ is the winding resistance, which is proportional to the temperature-dependent copper resistivity [12]:

$$\rho_{Cu,j} = \rho_{Cu,j,\theta_0}(1 + \alpha_{Cu,j}(\theta_{Cu,j} - \theta_0)) \quad (7.24)$$

where $\theta_{Cu,j}$ is the axle-specific stator windings' temperature, $l_{w,j}$ is the wire length, and $S_{w,j}$ is the wire cross section. The rotor iron loss has been estimated by:

$$P_{Fe,j} = P_{hy,j} + P_{cl,j} + P_{ex,j} \quad (7.25)$$

where $P_{hy,j}$ denotes the axle-specific hysteresis loss, $P_{cl,j}$ denotes the classical losses, and $P_{ex,j}$ denotes the excess losses. All these losses are dependent on the flux density B , and the frequency f :

$$P_{Fe,j} = afB_j^\alpha + bf^2B_j^2 + cfB(\sqrt{(1 + efB_j)} - 1) \quad (7.26)$$

where B_j is the flux density of either motor (Front or Rear). The coefficients a , b , c , and e are estimated according to [128], where $b = \frac{\sigma d^2}{12}$, with d being the lamination thickness and σ being the steel conductivity. Since the front and rear PMSMs have the same material and geometry, these coefficients are the same for both PMSMs. The magnet, bearings and additional stator losses are neglected in this work as they form an insignificant fraction of the overall losses and do not vary significantly with temperature. Copper losses for the front and rear motors for both Baseline and Thermal scenarios are visualised in Figure 8.14 and Figure 8.15. For the front and rear motors, the total PMSM losses are visualised in Figure 8.18 and Figure 8.19, respectively. The copper and rotor energy losses are defined in Equation 7.27 and Equation 7.28, respectively.

$$W_{Cu,j} = \int_{t=0}^{t_f} P_{Cu,j} \quad (7.27)$$

$$W_{Fe,j} = \int_{t=0}^{t_f} P_{Fe,j} \quad (7.28)$$

where t_f is the duration of the drive cycle in seconds. A second-order LPTN thermal model was introduced in [129] to monitor long-duration transients and steady-state temperatures in an electric

motor. This model looks at the motor's dominant heat paths, making it computationally efficient and suitable for the DP framework. The thermal equivalent circuit is depicted in Figure 7.7.

The corresponding state-space system is as follows:

$$\begin{bmatrix} C_{Cu,j} & 0 \\ 0 & C_{Fe,j} \end{bmatrix} \begin{bmatrix} \frac{d\theta_{Cu,j}}{dt} \\ \frac{d\theta_{Fe,j}}{dt} \end{bmatrix} = \begin{bmatrix} -\frac{1}{R_{Cu,j}} - \frac{1}{R_{Fe,j}} & \frac{1}{R_{Fe,j}} \\ \frac{1}{R_{Fe,j}} & \frac{-1}{R_{Fe,j}} \end{bmatrix} \begin{bmatrix} \theta_{Cu,j} \\ \theta_{Fe,j} \end{bmatrix} + \begin{bmatrix} \frac{1}{R_{Cu,j}} & 1 & 0 \\ 0 & 0 & 1 \end{bmatrix} \begin{bmatrix} \theta_0 \\ P_{Cu,j} \\ P_{Fe,j} \end{bmatrix} \quad (7.29)$$

where $\theta_{Cu,j}$ is the axle-specific stator temperature, $\theta_{Fe,j}$ is the rotor temperature, θ_0 is the ambient temperature, $R_{Cu,j}$ and $R_{Fe,j}$ are the axle-specific thermal resistances, $C_{Cu,j}$ and $C_{Fe,j}$ are the thermal capacitance, and $P_{Cu,j}$, $P_{Fe,j}$ are the heat sources. To facilitate the acquisition of the rotor temperature $\theta_{Fe,j}$, a PT100 temperature sensor is situated on the windings [130], with the data visualised in Figure 8.7. The industrial partner uses this sensor to measure the rotor temperature. They have conducted various tests to develop an accurate fit screening model for $\theta_{Fe,j}$, used in this work. The method is as follows:

1. Soak motor until the stator temperature is stabilised within 2 °C of the inlet cooling temperature
2. Run test point at steady state for ten minutes
3. Record the rotor temperature at the end of the ten minutes
4. Operate the machine in both clockwise and anti-clockwise quadrants

The most significant factors were found to be the inlet temperature, the motor speed and the RMS current. The model correlation is quite accurate, with an R-square value of 99.6%:

$$\theta_{Fe,j} = -6.03\theta_{inlet,j} + 0.005913\omega_{m,j} + 0.01696I_{rms,j} \quad (7.30)$$

where $\theta_{inlet,j}$ is the axle-specific inlet coolant temperature. As coolant flows, it absorbs thermal energy and rises in temperature with a flow rate of 1.5 L/min, leading to a linear rise of inlet temperature over time [131]. As $\theta_{Fe,j}$ is known through the PT100 sensor, the non-coupled state-space system in Equation 7.29 is reduced to the following first-order system:

$$C_{Cu,j} \frac{d\theta_{Cu,j}}{dt} = -\left(\frac{1}{R_{Cu,j}} + \frac{1}{R_{Fe,j}}\right)\theta_{Cu,j} + \frac{1}{R_{Fe,j}}\theta_{Fe,j} + \frac{\theta_0}{R_{Cu,j}} + P_{Cu,j} + P_{Fe,j} \quad (7.31)$$

A Motor-CAD model is developed by the R&D department of the industrial partner, in which a hairpin motor model in Simulink is implemented, based directly on the Motor-CAD exports. This process allows new motor concepts and updates, to be quickly pushed to the vehicle/thermal models, using the Motor-CAD model as a source of truth. Following the same method in [132], [133] and [134], an NN model is developed by the industrial partner to accurately estimate the temperature of the multiple nodes of the PMSMs used in this work. An NN model is a computational model inspired by biological processes within brains, comprising interconnected processing elements (also known as neurons) that combine to establish a response as a function of one or more inputs [135]. Training data is required to build the NN model to predict motor losses (Iron, Copper and Magnet) and the phasor component of armature current (I_q and I_d), along with their associated fluxes B_D and B_Q . The training data is directly obtained as steady operating maps of the motor (acquired directly from the Motor-CAD model) as a function of the following variables:

1. DC Bus Voltage (varied between 250, 290, 330, 370, 410 V)
2. Magnet Temperature (varied between -30, 0, 30, 60, 90, 120, 150 °C)
3. Winding Temperature (varied between -30, 0, 30, 60, 90, 120, 150 °C)
4. Speed (rpm)
5. Torque (Nm)

For all the combinations of the first three variables, speed-torque maps are generated for the losses, armature current components and associated fluxes. The neural network is trained on this data set and the trained NN blocks for each output are embedded within the loss model. The NN blocks are a combination of mathematical operations and a set of weights and biases that allow the creation of a transfer function between the inputs and the outputs without apriori knowledge of the inputs and outputs. For this work, the industrial partner has developed a two-layer feed-forward NN (with ten neurons in each layer) and trained over the steady-state training data. A dedicated NN is generated for each of the outputs, namely:

1. Magnet Loss (W)
2. Copper Loss (W)
3. Iron Loss (W)
4. I_q Peak (A)
5. I_d Peak (A)
6. B_D (mVs)
7. B_Q (mVs)

The model is developed in MATLAB and Simulink with the following advantages:

- Reliance on look-up maps, which helps simplify the inverter control
- Dynamic loss modelling for the thermal motor model
- Mimicking the results of the Motor-CAD model with the minimum computational expense
- Very accurate correlation between the trained dataset for all the modelled responses

The collaboration with the industrial partner led to accurate temperature estimation of the different nodes and heat paths in the PMSMs. The sensor measurement points were also available and used to validate the identified thermal parameters in Equation 7.29.

The second-order PMSM thermal dynamics parameters are identified using the curve fitting method based on the acquired experimental data for the front and rear PMSMs. The temperature data are visualised in Figure 7.8, Figure 7.9, for the front and rear motors, respectively. The validation test case assumes a constant ambient temperature of 40 °C and a single load point of 3000 rpm speed and 200 Nm torque. The identified parameters are visualised in Table 7.3. The temperature node of interest in this work is the stator windings' temperature θ_{Cu} , which is used as a state in the optimal control problem formulation, outlined in Equation 8.9. The motor efficiency maps visualised in Figure 8.12 and Figure 8.13 are dependent on the stator windings' temperature (θ_{Cu}).

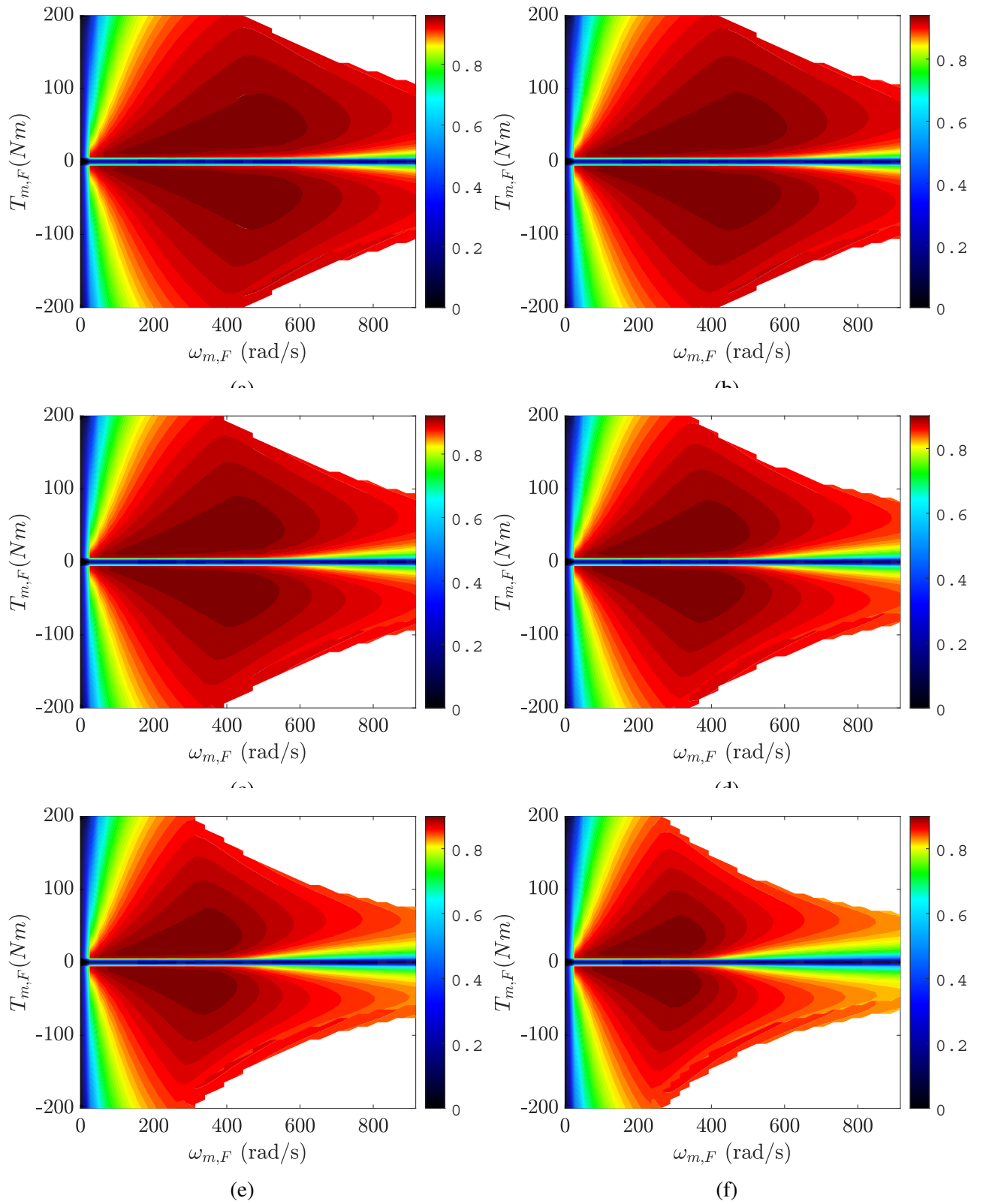


Figure 7.5: The front PMSM steady-state power efficiency maps for variations in the load torque $T_{m,F}$, and the front rotor speed $\omega_{m,F}$, for six different motor stator windings' temperatures. As only forward vehicle motion is considered in this work, the rotor speed is always non-negative, and the PMSM has two modes of operation: 1) positive $T_{m,F}$ (motoring) and 2) negative $T_{m,F}$ (regenerating). The contours correspond to constant efficiencies. The depicted efficiencies correspond to temperatures of -40 °C (a), 0 °C (b), 40 °C (c), 80 °C (d), 120 °C (e) and 165 °C (f).

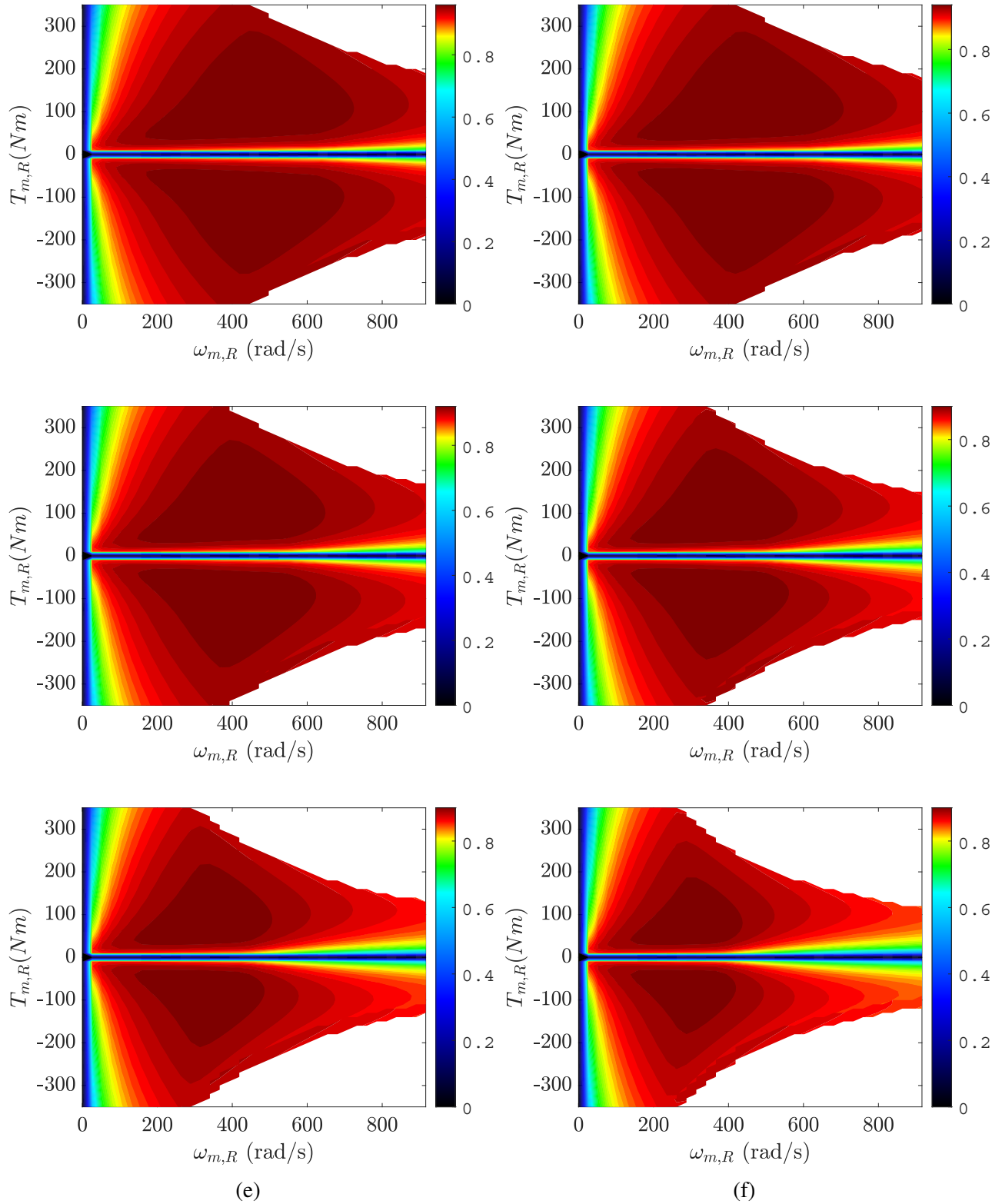


Figure 7.6: The rear PMSM steady-state power efficiency maps for variations in the load torque $T_{m,R}$, and the rear rotor speed $\omega_{m,R}$, for six different motor stator windings' temperatures. As only forward vehicle motion is considered in this work, the rotor speed is always non-negative, and the PMSM has two modes of operation: 1) positive $T_{m,R}$ (motoring) and 2) negative $T_{m,R}$ (regenerating). The contours correspond to constant efficiencies. The depicted efficiencies correspond to temperatures of -40 °C (a), 0 °C (b), 40 °C (c), 80 °C (d), 120 °C (e) and 165 °C (f).

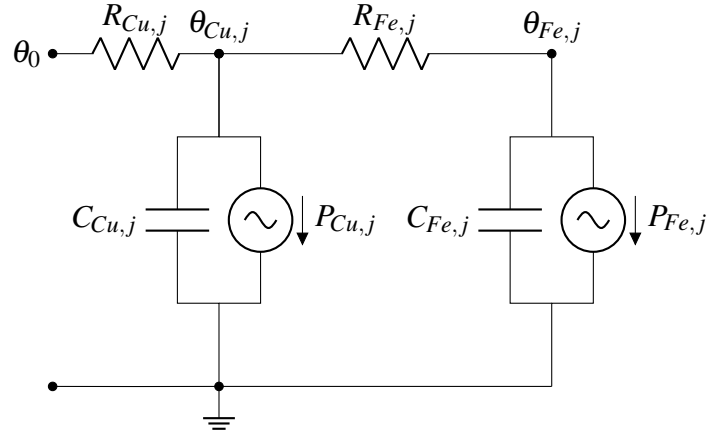


Figure 7.7: Thermal equivalent circuit of the PMSM.

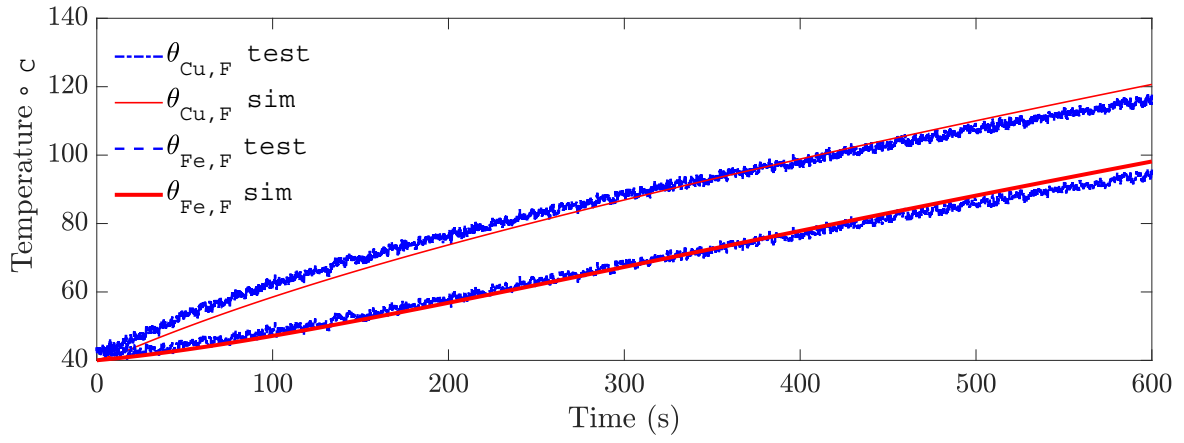
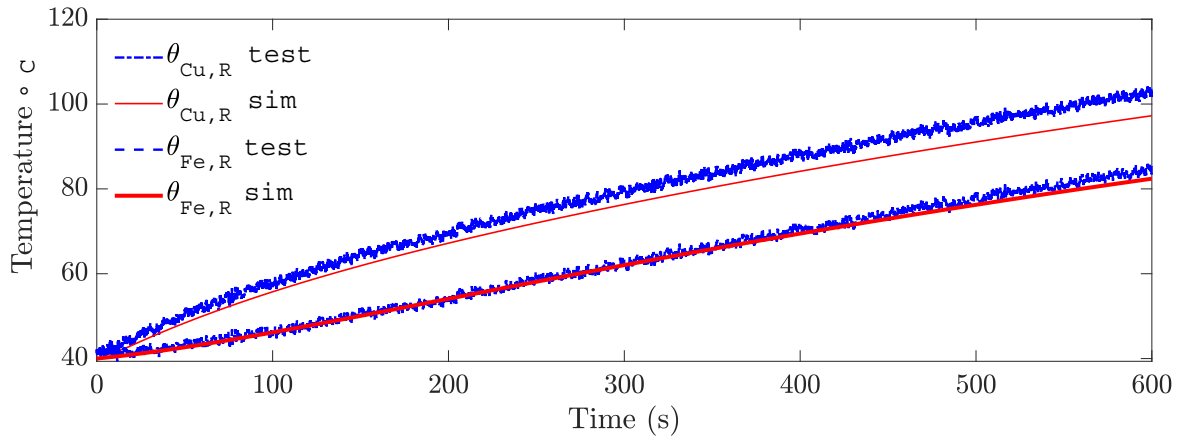
Figure 7.8: The testing (test) and simulation (sim) temperatures of the front PMSM stator windings $\theta_{Cu,F}$, and the front PMSM rotor temperature $\theta_{Fe,F}$.Figure 7.9: The testing (test) and simulation (sim) temperatures of the rear PMSM stator windings $\theta_{Cu,R}$, and the rear PMSM rotor temperature $\theta_{Fe,R}$.

Table 7.3: Front and Rear PMSM second-order thermal dynamics parameters

Parameter	Axle	Symbol	Value
Copper thermal resistance	Front	$R_{Cu,F}$	0.1086 °C/W
Copper thermal capacitance	Front	$C_{Cu,F}$	2196.823 J/°C
Copper thermal resistance	Rear	$R_{Cu,R}$	0.538 °C/W
Copper thermal capacitance	Rear	$C_{Cu,R}$	3982.056 J/°C
Iron thermal resistance	Front	$R_{Fe,F}$	0.5069 °C/W
Iron thermal capacitance	Front	$C_{Fe,F}$	3847.074 J/°C
Iron thermal resistance	Rear	$R_{Fe,R}$	0.1022 °C/W
Iron thermal capacitance	Rear	$C_{Fe,R}$	7547.038 J/°C

7.3 System Integration

A backward vehicle model based on the vehicle's longitudinal dynamics is established to perform DP. The system integration is the same for the Baseline and Thermal models. The required driving force is as follows:

$$F_v = m_v \frac{dv}{dt} + F_r + F_d \quad (7.32)$$

where the non-negative vehicle speed v , is an exogenous input to the vehicle model derived from the given drive cycle. m_v is the vehicle mass, F_r is the rolling resistance force, and $F_d = \rho v^2$ is the aerodynamic drag force, in which ρ is the drag resistance coefficient. In this work $m_v=3600$ kg, $\rho=0.32$ kg/m, and $F_r = 144$ N. The wheel speed is derived from the vehicle speed:

$$\omega_{wheel} = v/R_{wheel}, \quad (7.33)$$

where $R_{wheel} = 325$ mm is the wheel radius. The total required driving power P_{PL} is computed as follows:

$$P_{PL} = F_v v, \quad (7.34)$$

which equates to the total transmission power ($P_{mt,F} + P_{mt,R} \geq 0$), and the total braking power ($P_{mt,F} + P_{mt,R} + P_{Br} < 0$):

$$P_{PL} = P_{mt,F} + P_{mt,R} + P_{Br}. \quad (7.35)$$

$$T_{Tot} = T_{m,F} + T_{m,R} + T_{Br} + T_{F0} + T_{R0}. \quad (7.36)$$

where $T_{m,F}$ is the front motor driving torque, $T_{m,R}$ is the rear motor driving torque, T_{Br} is the mechanical brake torque, $T_{F0} = J_{m,F} \frac{d\omega}{dt}$ and $T_{R0} = J_{m,R} \frac{d\omega}{dt}$ are the torques due to the front and rear motors' inertia, respectively; with $J_{m,F}$ being the front PMSM rotor inertia and $J_{m,R}$ being the rear PMSM rotor inertia. The values for these parameters are summarised in Table 7.2. The brake force distribution method in this work incorporates the strategy in [136], which is an approximation of the optimal brake force distribution described below:

$$P_{Br} = \begin{cases} 0, & P_{PL} \geq 0 \\ \min(\lambda P_{PL}, P_{PL} - (P_{mtmin,F} + P_{mtmin,R})), & P_{PL} < 0 \end{cases} \quad (7.37)$$

where $P_{mtmin} < 0$ is the minimum charging power of the secondary source and $\lambda=1/3$. Regenerative braking generates approximately 70% of the braking force, while the remaining 30% is provided by the friction brake. This is subject to the availability of the regenerative torque at every operating point, and if there is insufficient regenerative torque, the friction brake meets the rest of the braking torque demand. In this work, mechanical and regenerative braking can be performed on both axles. The braking force can be regenerated up to the maximum battery charging power.

7.4 Chapter Summary

Two EV models were presented in this chapter: Baseline and Thermal, comprising the following components:

- Battery
- DC-DC Converter
- DC Link and Inverter
- PMSM
- Motor Transmission
- Thermal Dynamics of the PMSM

The Thermal model was similar to the Baseline model except for the added thermal dynamics of the PMSMs. The industrial partner provided both model parameters. The optimal solution gained from the Baseline DP in section 8.2 is based on the Baseline model outline in section 7.1. The optimal solution gained from the Thermal DP in subsection 8.3.1 is based on the Thermal model described in section 7.2. The EV models presented in this chapter were backward-facing models, unlike the forward-facing HEV model in the first part of the thesis. These EV models are used in Chapter 8 to implement the DP energy management strategy. As DP is an optimal control strategy, a forward-facing model would be unsuitable due to the high computational load.

Chapter 8

Optimal Control Problem & Results for the Energy Management of EVs

8.1 Optimal Control Problem Formulation

The main objective of the Supervisory Control System (SCS) in this work is to determine the optimal power split between the front and rear motors of a dual-motor Electric Vehicle (EV) for a predetermined driving cycle. This is done to minimise the cost function defined for the control problem. Knowing the optimal solution can be beneficial when developing sub-optimal controllers, as optimal solutions are often used as benchmarks and guidelines to extract rules for heuristic methods [137].

Dynamic Programming (DP) is a conventional optimisation-based control strategy for EVs and HEVs that can provide optimal global solutions for backward-facing vehicle models, which are simplified representations of vehicle dynamics. Such models are helpful because they allow for efficient computation of control solutions [138]. This section describes the problem formulation and the implementation of two optimal control problems. In section 8.2, DP is implemented and solved for the Baseline EV model described in section 7.1. In subsection 8.3.1, DP is implemented and solved for the Thermal EV model in section 7.2, wherein the temperature of the front and rear motors varies over time as opposed to remaining constant as in the Baseline model.

Once the optimal torque split (i.e. between the front and rear motors) is acquired, this solution is fed as input into the DP framework, in which the Permanent Magnet Synchronous Motor (PMSM) thermal dynamics presented in subsection 7.2.1 are included. This scenario is referred to as the **Baseline DP** case study, while the optimisation performed on the Thermal model with the thermal dynamics is referred to as the **Thermal DP** case study.

8.2 Baseline DP

In this section, DP is implemented on the low-fidelity vehicle model introduced in section 7.1. The power flow of this EV model is outlined in subsection 8.2.1, and the optimal control problem is formulated in subsection 8.2.2.

8.2.1 Baseline Model System Integration

The integrated powertrain of the Baseline EV model under investigation has two independent power sources (without any thermal dynamics included): $P_{mt,F}$ and $P_{mt,R}$, where $P_{mt,F}$ is the front motor driving power, and $P_{mt,R}$ is the rear motor driving power. The vehicle power flow can be summarised by combining Equations 7.7, 7.9, 7.21, and 7.5 as follows:

$$\begin{cases} P_{PL} = \sum_{j \in \{F,R\}} P_{mt,j} + P_{Br}, \\ P_b = \sum_{j \in \{F,R\}} (\eta_{dc} \eta_i \eta_{m,j} (T_{m,j}, \omega_{m,j}) \eta_t)^{\text{sign}(-P_{mt,j})} P_{mt,j} \\ P_{b,in} = E_b \times \frac{E_b - \sqrt{E_b^2 - 4P_b R_b}}{2R_b} \end{cases} \quad (8.1)$$

where $j \in F, R$ stands for the front and rear axles, respectively. $P_{mt,j}$ is the respective motor's operating power, and $P_{mtmin,j}$ and $P_{mtmax,j}$ are the minimum and maximum operating powers for the motors. P_{Br} is the power used to brake the vehicle, and P_{PL} is the total power loss. P_b is the battery power, and $P_{b,in}$ is the power entering the battery. η_{dc} , η_i , $\eta_{m,j}$, η_t , $T_{m,j}$, and $\omega_{m,j}$ are efficiency factors, motor torque and speed, respectively.

The power flow is subject to the following constraints:

$$\begin{cases} P_{mtmin,j} \leq P_{mt,j} \leq P_{mtmax,j} \\ I_{bmin} \leq I_b \leq I_{bmax} \end{cases} \quad (8.2)$$

I_{bmin} and I_{bmax} are the battery current limits. To prevent damage to the battery, the charging current is limited to 125 A, and the discharging current is constrained to 100 A.

The rate of change of State of Charge (SOC) of the battery can be expressed as:

$$\frac{d}{dt}(SOC) = -\frac{I_b(SOC, P_{mt,F}, P_{mt,R}, v)}{Q_{max}} \quad (8.3)$$

where I_b is the battery current, and Q_{max} is the maximum battery charge. The optimal control problem is solved in the discrete-time framework in DP, so SOC dynamics are discretized using Euler's method with a sampling period of 1s [137].

8.2.2 Baseline Optimal Control Problem Formulation

According to [137], the EV model equations described in section 7.1 can be summarised in the discretized format as:

$$x_{k+1} = f(x_k, u_k, v_k, a_k, i_k) + x_k \quad (8.4)$$

Here, $x_k \in X_k$ is the state variable vector, which, in this optimal control problem, is $x_k = SOC$; $u_k \in U_k$ is the control variable vector, which is defined as $u = \frac{T_{m,F}}{T_{Tot}}$, where $T_{m,F}$ is the front driving torque, and T_{Tot} is the total driving torque demand demonstrated in Equation 7.36. The model assumptions are as follows:

- The PMSMs, as well as other components, stay at a constant pre-defined temperature
- The PMSM efficiency maps are captured at a temperature of 10 °C

- There are no energy losses during gear shifting

Since the drive cycle is known apriori, v_k , a_k and i_k at instant k are included in the model function to form the time-variant model:

$$x_{k+1} = f(x_k, u_k) + x_k, \quad k = 0, 1, \dots, N-1 \quad (8.5)$$

The cost function J is defined as:

$$J = \sum_{k=0}^{N-1} P_{b,in}(u_k, k) \cdot T_s \quad (8.6)$$

The optimisation problem of minimising the total electrical energy consumed for the Baseline dual-motor EV model over the Japanese 10-15 drive cycle (JN1015) can be formulated as the following discrete-time optimal control problem:

$$\min_{u_k \in U_k} \sum_{k=0}^{N-1} P_{b,in}(u_k, k) \quad (8.7a)$$

$$\text{subject to : } x_{k+1} = f(x_k, u_k) + x_k \quad (8.7b)$$

$$x_0 = 0.8 \quad (8.7c)$$

$$x_k \in [0.1, 0.9] \quad (8.7d)$$

$$N = \frac{660}{T_s} + 1 \quad (8.7e)$$

where $T_s = 1$ s is the time step, x_0 is the initial state, and $N=661$ is the number of time steps in the problem. DP is used to solve the optimal control in Equation 8.7b, in which 61 grid points have been allocated to the SOC and 21 for the input. The two-point DP boundary method is implemented according to [22]. The DP algorithm solves a discrete-time optimal control backwards from the final state to the initial state in MATLAB with the **dpm** function as described in [137]; this is performed by decomposing the problem into a sequence of simpler discrete sub-problems [5].

8.3 Thermal DP

In this section, DP is implemented on the vehicle model introduced in section 7.2. In section 8.2, the temperature of the PMSMs was assumed to stay constant. In this section, the thermal dynamics of the PMSMs are taken into account. The goal is to compare the Thermal DP energy management optimal solution with that of the Baseline DP. The power flow of the Thermal EV model is described in subsection 8.3.1, with the optimal discrete-time control problem formulated in subsection 8.3.2.

8.3.1 Thermal Model System Integration

The integrated powertrain of the EV model under investigation has two independent temperature-dependent power sources: $P_{mt,F}$ and $P_{mt,R}$, where $P_{mt,F}$ is the front motor driving power and $P_{mt,R}$ is the rear motor driving power. Combining Equations 7.7, 7.9, 7.21, and 7.5, the vehicle power flow is summarised as follows:

$$\begin{cases} P_{PL} = \sum_{j \in \{F,R\}} P_{mt,j} + P_{Br}, \\ P_b = \sum_{j \in \{F,R\}} (\eta_{dc} \eta_i \eta_{m,j}(T_{m,j}, \omega_{m,j}, \theta_{Cu,j})) \eta_t^{sign(-P_{mt,j})} P_{mt,j} \\ P_{b,in} = E_b \times \frac{E_b - \sqrt{E_b^2 - 4P_b R_b}}{2R_b} \end{cases} \quad (8.8)$$

where $j \in [F,R]$, stands for front and rear axles, respectively. The PMSMs' power and battery limits are defined in Equation 8.2. $\theta_{Cu,F}$ and $\theta_{Cu,R}$ denote the front and rear motor stator windings' temperatures, respectively.

The SOC dynamics, as well as the front and rear PMSM stator windings' temperatures, are defined as:

$$\frac{d}{dt} \begin{pmatrix} SOC \\ \theta_{Cu,F} \\ \theta_{Cu,R} \end{pmatrix} = \begin{pmatrix} -\frac{I_b(SOC, P_{mt,F}, P_{mt,R}, v)}{Q_{max}} \\ -(\frac{1}{R_{Cu,F}C_{Cu,F}} + \frac{1}{R_{Fe,F}C_{Cu,F}})\theta_{Cu,F} + \frac{1}{R_{Fe,F}C_{Cu,F}}\theta_{Fe,F} + \frac{\theta_0}{R_{Cu,F}C_{Cu,F}} + \frac{P_{Cu,F}}{C_{Cu,F}} + \frac{P_{Fe,F}}{P_{Cu,F}} \\ -(\frac{1}{R_{Cu,R}C_{Cu,R}} + \frac{1}{R_{Fe,R}C_{Cu,R}})\theta_{Cu,R} + \frac{1}{R_{Fe,R}C_{Cu,R}}\theta_{Fe,R} + \frac{\theta_0}{R_{Cu,R}C_{Cu,R}} + \frac{P_{Cu,R}}{C_{Cu,R}} + \frac{P_{Fe,R}}{P_{Cu,R}} \end{pmatrix} \quad (8.9)$$

with the detailed explanation of the temperature dynamics presented in section 7.2 of Chapter 7. The

optimal control problem is formulated to implement the Thermal DP in the following section.

8.3.2 Thermal Optimal Control Problem Formulation

The optimisation problem of minimising the total electrical energy consumed for the thermal dual-motor EV model over the Japanese 10-15 drive cycle (JN1015) can be formulated as the following discrete-time optimal control problem:

$$\min_{u_k \in U_k} \sum_{k=0}^{N-1} P_{b,in}(u_k, k) \quad (8.10a)$$

$$\text{subject to : } x_{k+1} = f(x_k, u_k) + x_k \quad (8.10b)$$

$$x_{1,0} = 0.8 \quad (8.10c)$$

$$x_{2,0} = 10 \quad (8.10d)$$

$$x_{3,0} = 10 \quad (8.10e)$$

$$x_{1,k} \in [0.1, 0.9] \quad (8.10f)$$

$$x_{2,k} \in [-100, 300] \quad (8.10g)$$

$$x_{3,k} \in [-100, 300] \quad (8.10h)$$

$$N = \frac{660}{T_s} + 1 \quad (8.10i)$$

Here, $x_k \in X_k$ is the state variable vector, which, in this optimal control problem, is $x_k = \{SOC, \theta_{Cu,F}, \theta_{Cu,R}\}$, as opposed to one state (i.e. SOC) in the Baseline DP problem (outlined in Equation 8.9); $u_k \in U_k$ is the control variable vector, which, in this problem, is $u = \frac{T_{m,F}}{T_{Tot}}$, with $T_{m,F}$ being the front driving torque, and T_{Tot} the total driving torque demand, defined in Equation 7.36. $x_{1,0}, x_{2,0}$ and $x_{3,0}$ denote the initial state values. Similarly to the Baseline DP, 61 grid points have been used for the SOC, 31 for each temperature state and 21 for the input.

8.4 Dynamic Programming Solutions and Simulation Results

The drive cycle used in the simulations in this chapter is the Japanese 10-15 (JN1015), which is visualised in Figure 8.1. The JN1015 drive cycle has a distance of 4.16 km, an average speed of 22.7 km/h, and a duration of 660 s [139]. This is a suitable drive cycle for the vehicle of interest in this work, as it is a delivery van. Furthermore, the efficiencies of the PMSMs are calculated at different temperature points by interpolating the six efficiency maps described in section 7.2 for the front and rear PMSMs.

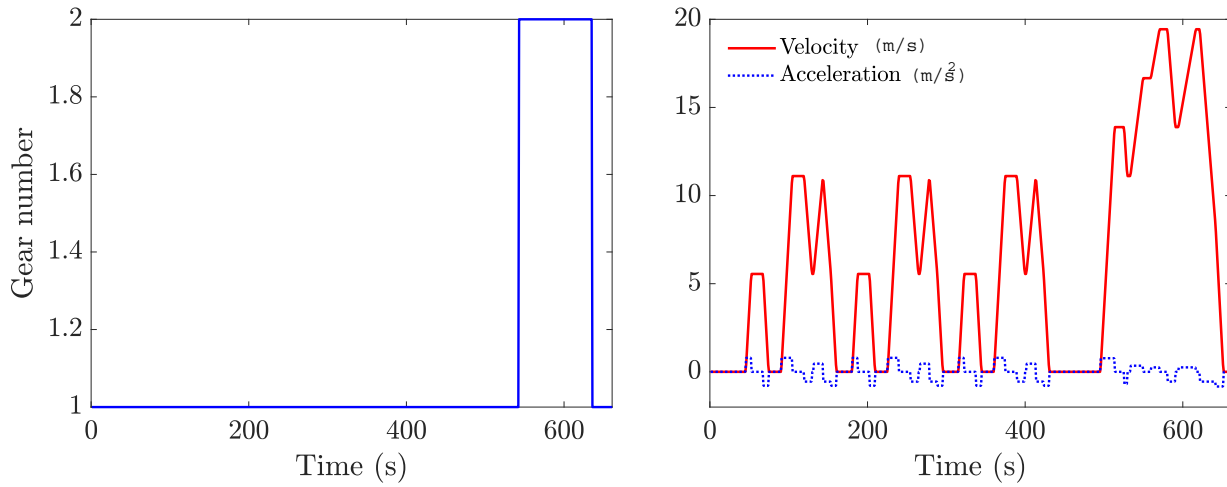


Figure 8.1: Velocity and acceleration profiles of the JN1015 drive cycle (right), Gear number used over the JN1015 drive cycle (left).

8.4.1 Torque and Power Split Profiles

The efficiency of the PMSM becomes poor with the increase of the internal motor temperature due to the rise of motor losses. This temperature effect is more significant in full-load cases. In the torque split and power split profiles shown in Figures 8.2, 8.3, 8.4, and 8.5, it can be observed that the Thermal DP (drive profile) uses both motors evenly and frequently in hybrid mode during the motoring phase, compared to the Baseline DP. This strategy is implemented to avoid full-load cases that could cause unfavourable temperature effects.

Moreover, since regenerative braking also affects the temperature rise in the PMSMs, the Thermal DP aims to limit the regenerative braking performed by the front motor, as it has smaller thermal

capacitance than the rear motor, which would have a higher impact on its temperature rise.

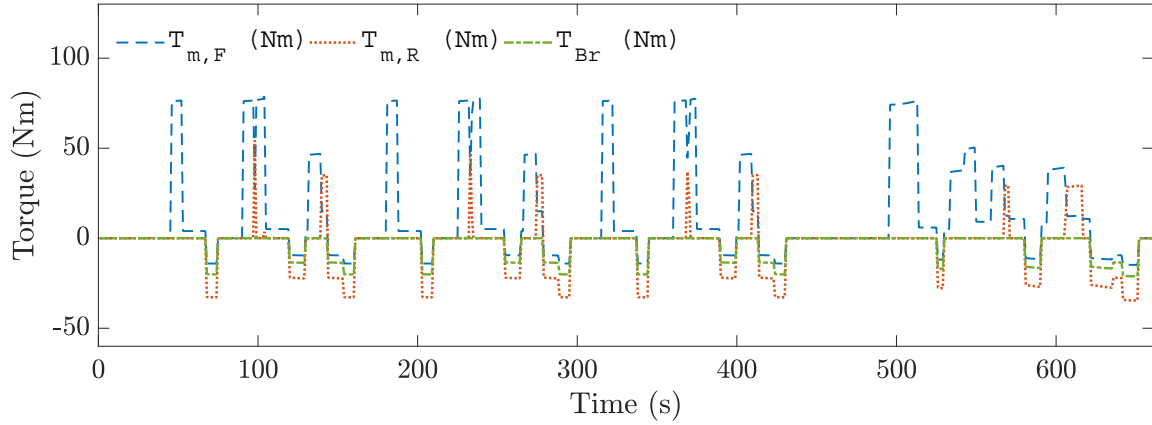


Figure 8.2: The Baseline DP optimal torque split between the front and rear motors over the JN1015 drive cycle. $T_{m,F}$ and $T_{m,R}$ denote the front and rear motor driving torques and T_{Br} denotes the mechanical braking torque.

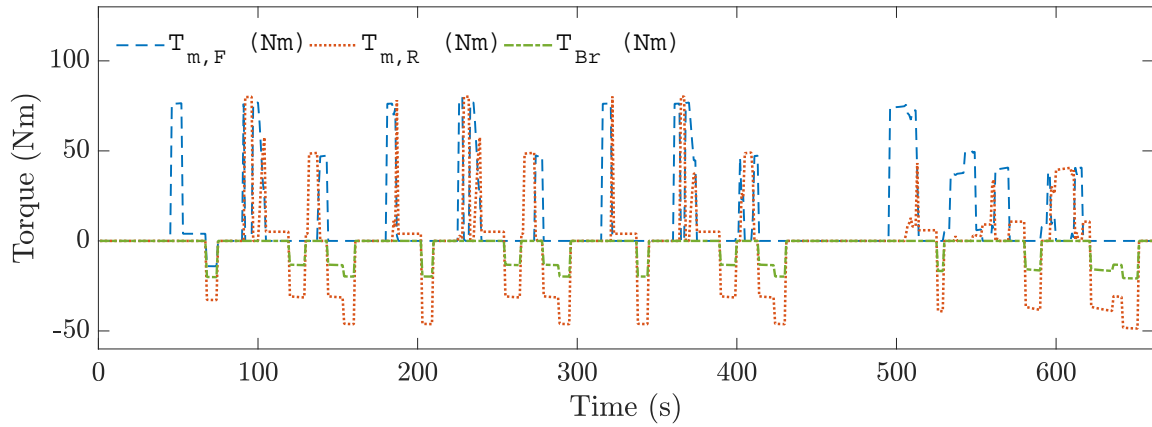


Figure 8.3: The Thermal DP optimal torque split between the front and rear motors over the JN1015 drive cycle. $T_{m,F}$ and $T_{m,R}$ denote the front and rear motor driving torques and T_{Br} denotes the mechanical braking torque.

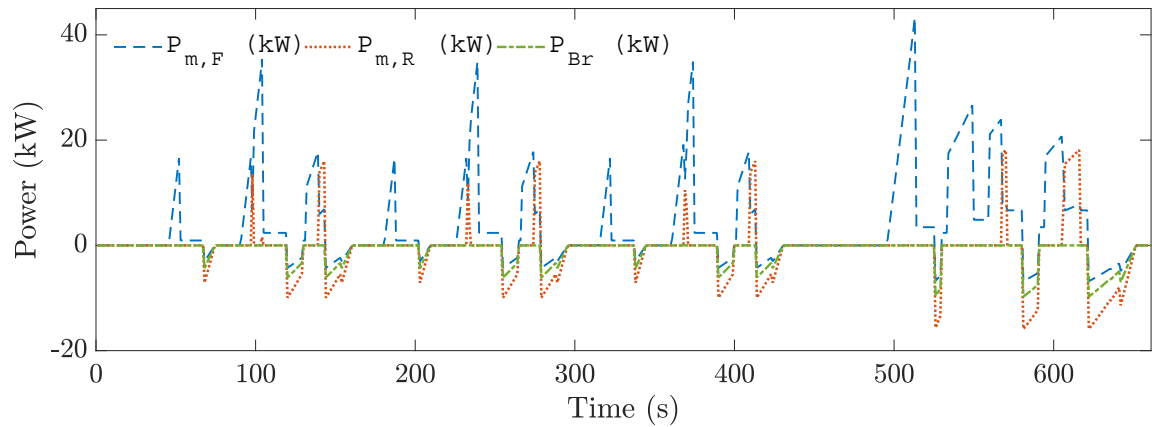


Figure 8.4: The Baseline DP optimal power split between the front and rear motors over the JN1015 drive cycle. $P_{m,F}$ and $P_{m,R}$ denote the front and rear motor driving torques and P_{Br} denotes the mechanical braking torque.

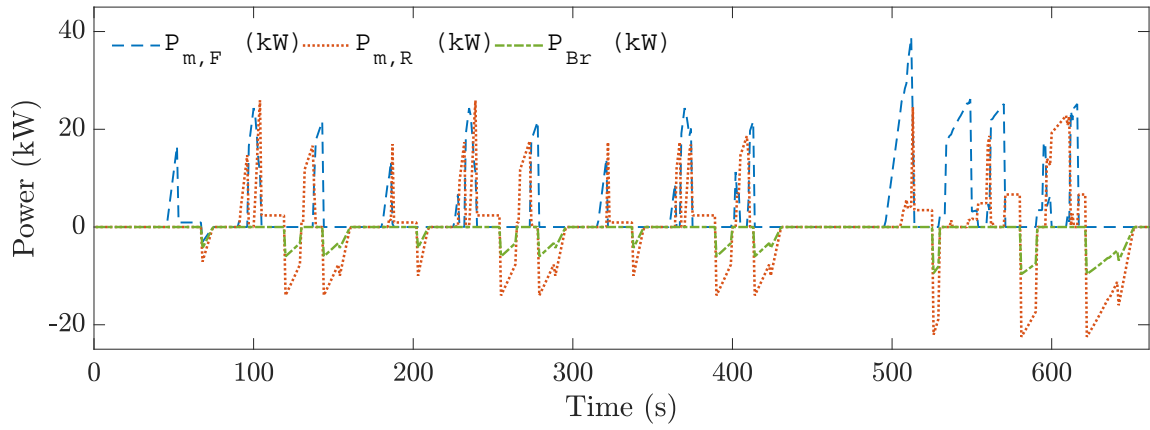


Figure 8.5: The Thermal DP optimal power split between the front and rear motors over the JN1015 drive cycle. $P_{m,F}$ and $P_{m,R}$ denote the front and rear motor driving torques and P_{Br} denotes the mechanical braking torque.

8.4.2 Temperature Profiles

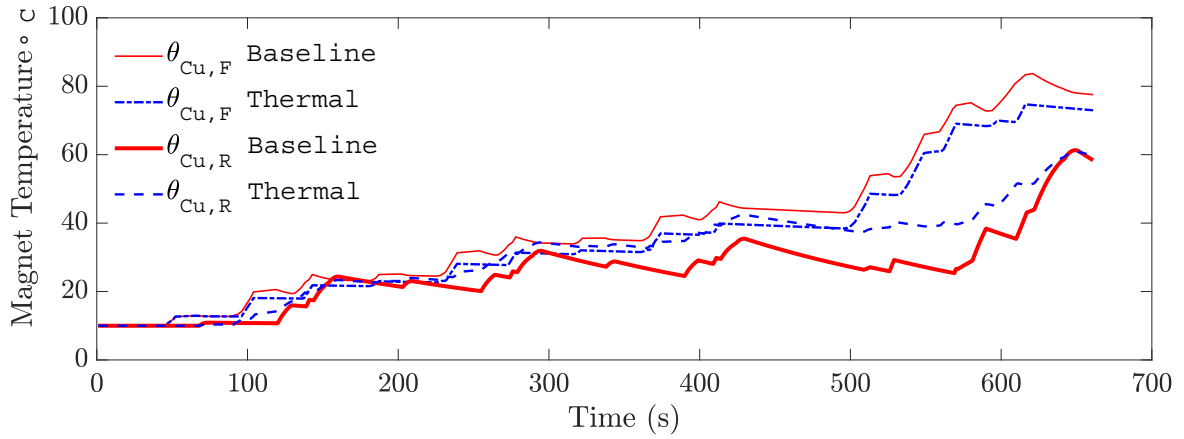


Figure 8.6: Time histories of the front and rear motors' stator windings' temperatures for the Baseline and Thermal DP case studies over the JN1015 drive cycle.

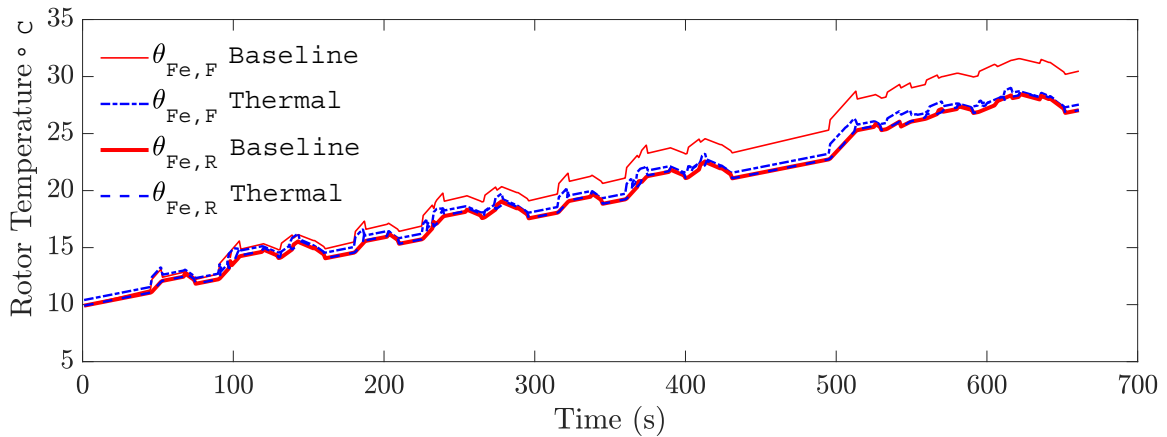


Figure 8.7: Time histories of the front and rear motors' rotor temperatures for the Baseline and Thermal DP case studies over the JN1015 drive cycle.

In Figure 8.6, the stator windings' temperature profiles for the front and rear motors show that the Thermal DP case study attempts to maintain similar temperatures for both motors, preventing one from overheating more than the other. The lower gap between the front and rear temperature profiles in the Thermal DP case study compared to the Baseline DP case study indicates this.

Further insights into the thermal operation of the motors can be gained from Figure 8.7. The sum of the final front and rear rotor temperatures, as well as the final stator windings' temperatures in Figure 8.6, is lower in the Thermal DP case study than in the Baseline DP case study. It is important to note that the estimated temperature may be higher in reality because the thermal dynamics of other powertrain components, such as the inverter and DC-DC converter, as well as environmental conditions, were not considered. This suggests that the advantages of the Thermal DP are likely more significant in practice.

8.4.3 Torque, Speed and Temperature Operating Points

The torque/speed operating points of the Baseline and Thermal DP case studies are visualised in Figure 8.8 and Figure 8.9 for the front and rear PMSMs, respectively. It can be observed that the optimal operating points of the Baseline and Thermal case studies are different.

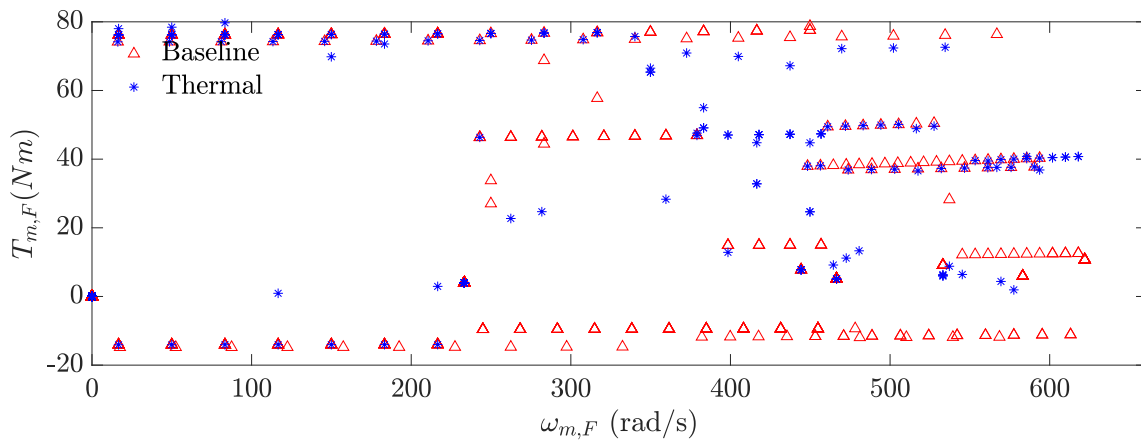


Figure 8.8: Torque versus angular speed of the front motor for the Baseline and Thermal DP case studies, over the JN1015 drive cycle.

The torque and speed operating points are superimposed over the efficiency contours of the front and rear PMSMs for the Baseline DP in Figure 8.10 and Figure 8.11, for the front and rear PMSMs, respectively. The optimal torque split between the two motors for every speed depends on the operating

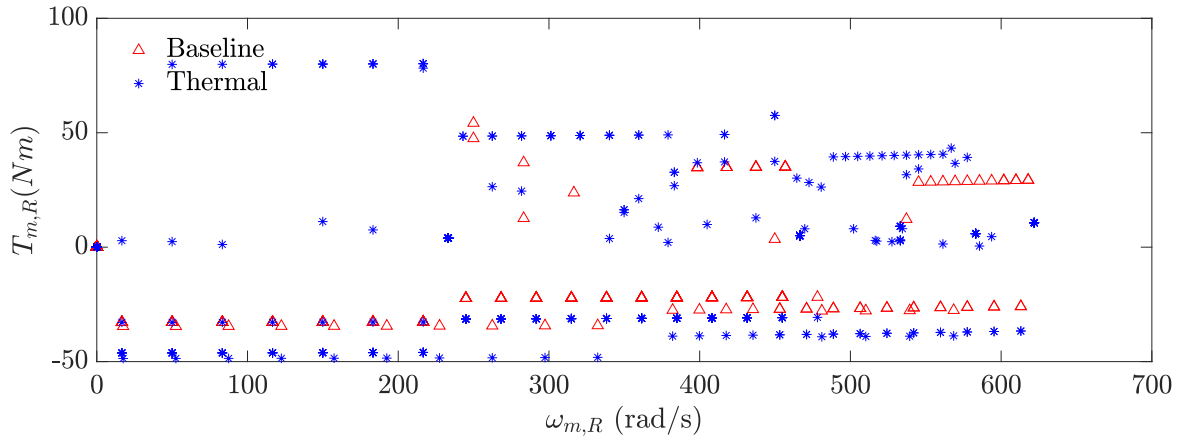


Figure 8.9: Torque versus angular speed of the rear motor for the Baseline and Thermal DP case studies, over the JN1015 drive cycle.

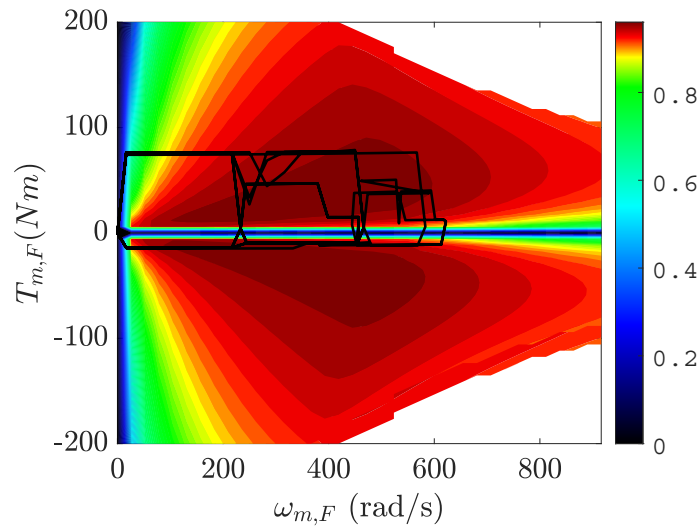


Figure 8.10: Torque versus angular speed Baseline DP operating points of the front motor over the JN1015 drive cycle, superimposed on the front motor efficiency map at a constant temperature of 10 °C.

PMSM efficiency. In the Baseline DP, the motor's efficiency depends on the torque and angular speed but not the motor temperature. This is because the stator windings' temperatures of both PMSMs have been assumed constant throughout the drive cycle. However, in the Thermal DP case study, the thermal dynamics of the PMSMs are modelled, and hence, temperature estimates of the front and rear PMSMs' stator windings' over the drive cycle are available. Consequently, the efficiency of both motors in the Thermal DP depends on the motor torque, angular speed, and temperature.

For visualisation purposes, the temperature range has been divided into four intervals. The interpolated efficiencies of each interval at the average interval temperature of the respective torque and speed operating points are displayed in Figure 8.12 and Figure 8.13 for the front and rear PMSMs,

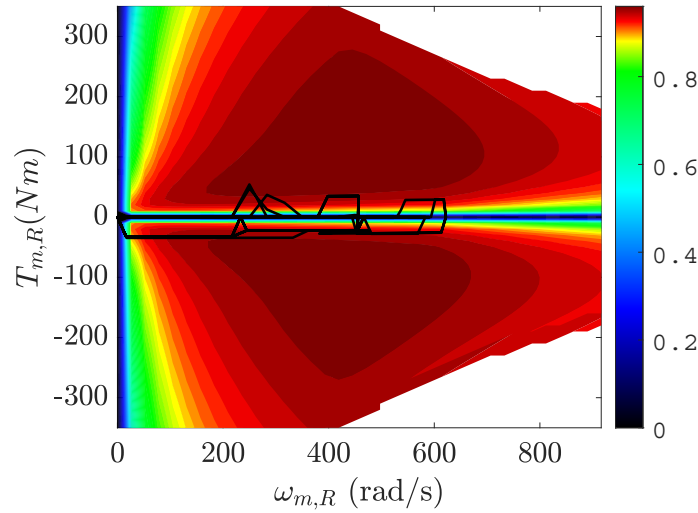


Figure 8.11: Torque versus angular speed Baseline DP operating points of the rear motor over the JN1015 drive cycle, superimposed on the rear motor efficiency map at a constant temperature of 10 °C.

respectively.

8.4.4 Powertrain Efficiency and Losses

This vehicle is a delivery van mainly used in low-speed, low-torque regions. In this region, copper losses are dominant, which means with rising temperatures, the losses increase and the efficiency drops. In the high-speed, low-torque area, the opposite trend is seen as iron loss is dominant. The conductivity of the laminates decreases with temperature rise [12]. This contrary behaviour of the loss and temperature correlations leads to the existence of the energy-optimal motor temperature at which the losses are minimal, and hence the efficiency is maximal. Additionally, by having two traction motors, the knowledge of each motor's temperature helps operate each motor in an efficient region. Including motor temperature in designing EVs' energy management control strategy can significantly improve overall efficiency.

The copper losses for the front and rear motors for the Baseline and Thermal DP case studies are visualised in Figure 8.14 and Figure 8.15, respectively. The iron losses for the front and rear motors for the Baseline and Thermal DP case studies are displayed in Figure 8.16 and Figure 8.17, respectively.

The total PMSM losses are depicted in Figure 8.18 and Figure 8.19 for the front and rear PMSMs, respectively. It can be seen that the total PMSM losses are lower in the Thermal DP case compared

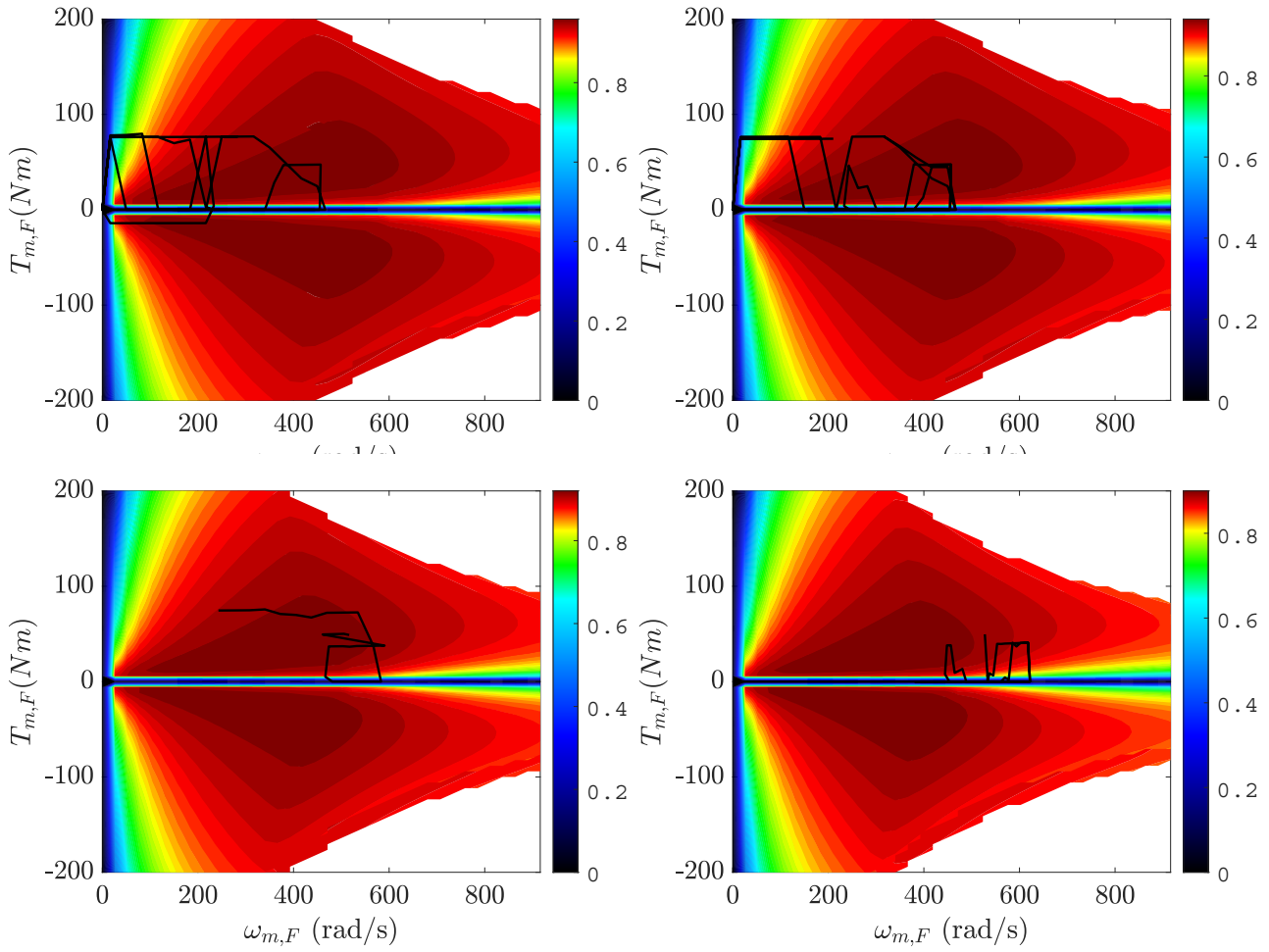


Figure 8.12: The stator windings' temperature of the front motor shown for the temperature intervals of 10 to 25 °C (top left), 25 to 40 °C (top right), 40 to 55 °C (bottom left) and 55 to 70 °C (bottom right). The efficiency visualised in every interval is the average of the respective temperature interval.

Table 8.1: Front and Rear PMSM energy losses for the Baseline and Thermal DP case studies, over the JN1015 drive cycle

Parameter	Axle	Case study	Symbol	Value
Copper energy loss	Front	Baseline	$W_{Cu,F}$	81.4216 KJ
Copper energy loss	Front	Thermal	$W_{Cu,F}$	58.1820 KJ
Copper energy loss	Rear	Baseline	$W_{Cu,R}$	37.9299 KJ
Copper energy loss	Rear	Thermal	$W_{Cu,R}$	27.1510 KJ
Iron energy loss	Front	Baseline	$W_{Fe,F}$	3.8946 KJ
Iron energy loss	Front	Thermal	$W_{Fe,F}$	4.3368 KJ
Iron energy loss	Rear	Baseline	$W_{Fe,R}$	11.9761 KJ
Iron energy loss	Rear	Thermal	$W_{Fe,R}$	11.8458 KJ
Total PMSM energy loss	Front	Baseline	$W_{L,F}$	85.31621 KJ
Total PMSM energy loss	Front	Thermal	$W_{L,F}$	62.5188 KJ
Total PMSM energy loss	Rear	Baseline	$W_{L,R}$	49.9060 KJ
Total PMSM energy loss	Rear	Thermal	$W_{L,R}$	38.9968 KJ

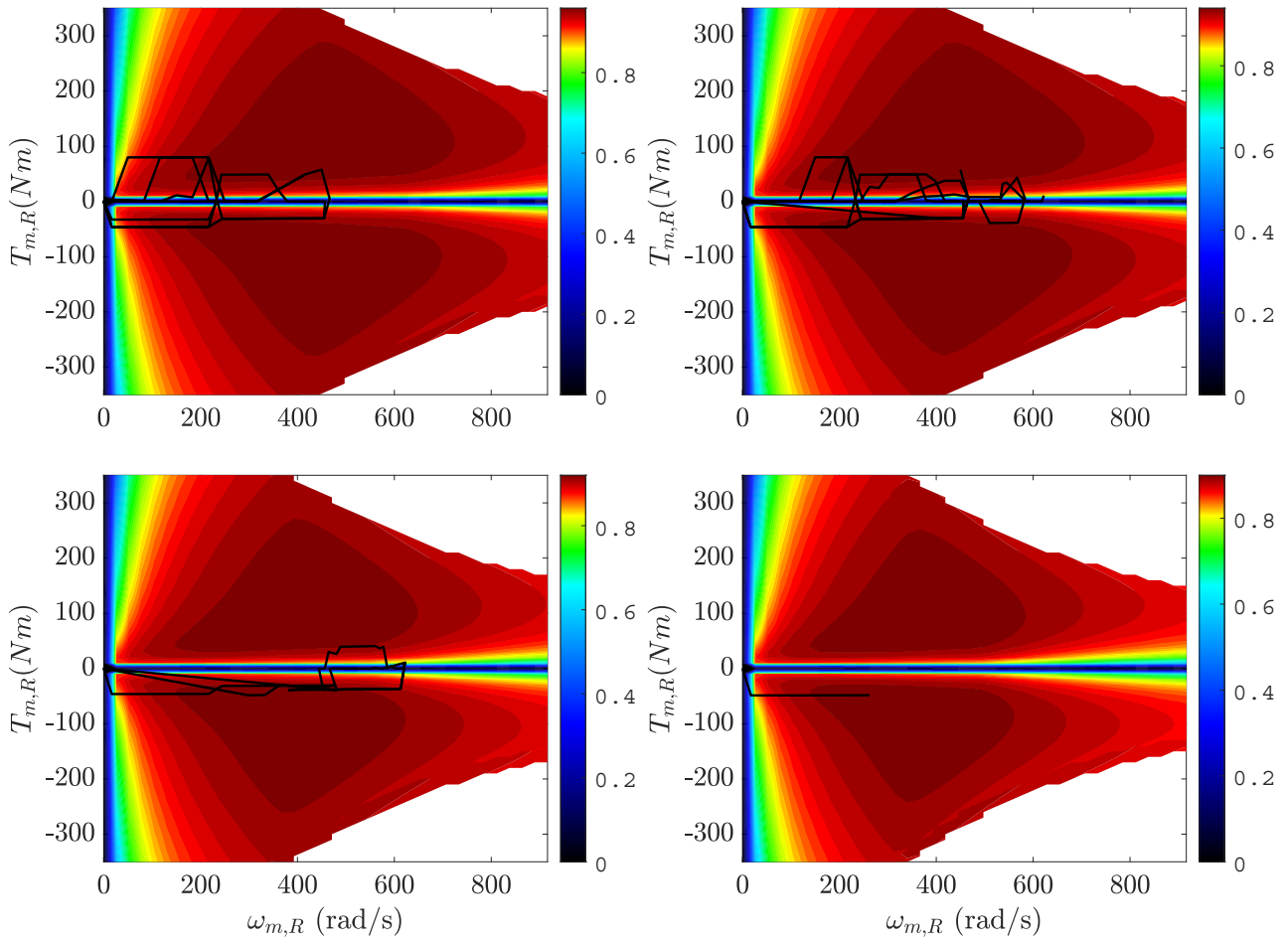


Figure 8.13: Stator windings' temperature of the rear motor shown for the temperature intervals of 10 to 25 °C (top left), 25 to 40 °C (top right), 40 to 55 °C (bottom left) and 55 to 70 °C (bottom right). The efficiency visualised in every interval is the average of the respective temperature interval.

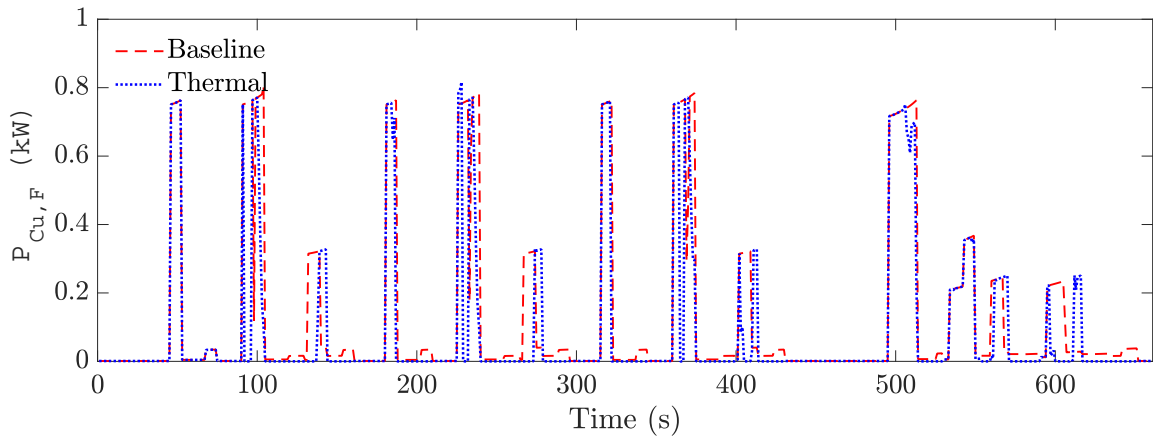


Figure 8.14: Front PMSM Copper loss $P_{Cu,F}$, for the Baseline and Thermal DP case studies over the JN1015 drive cycle.

to the Baseline DP case study.

The front and rear motor efficiency time profiles are shown in Figure 8.20 and Figure 8.21, respec-

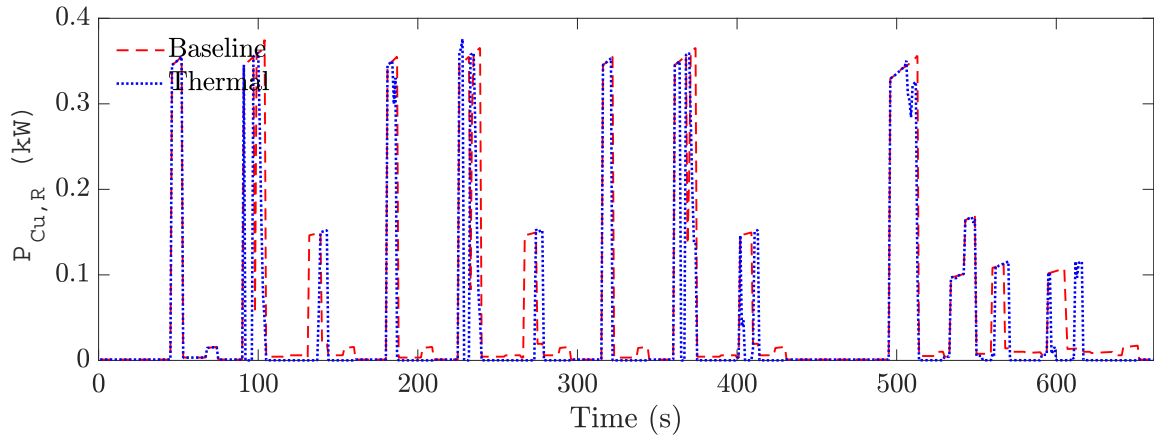


Figure 8.15: Rear PMSM copper loss $P_{Cu,R}$, for the Baseline and Thermal DP case studies over the JN1015 drive cycle.

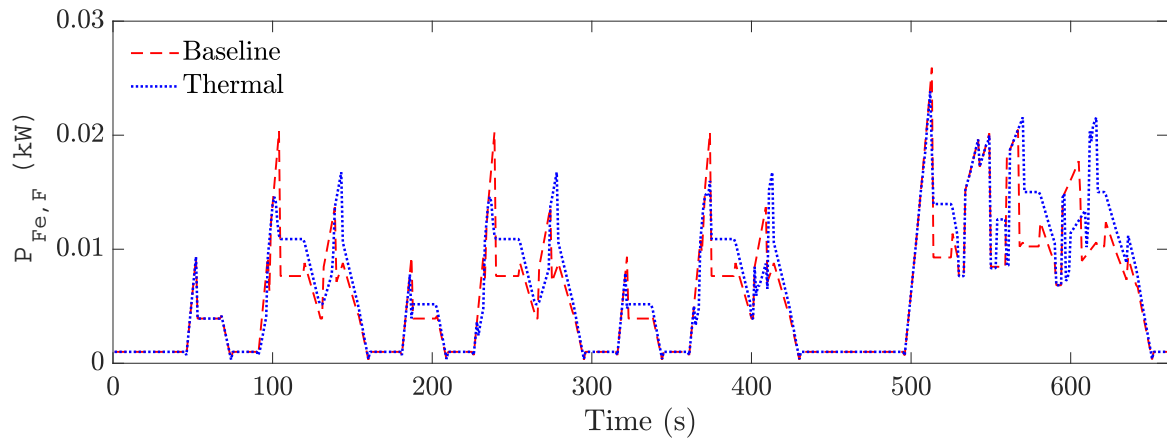


Figure 8.16: Front PMSM Iron loss $P_{Fe,F}$, for the Baseline and Thermal DP case studies over the JN1015 drive cycle.

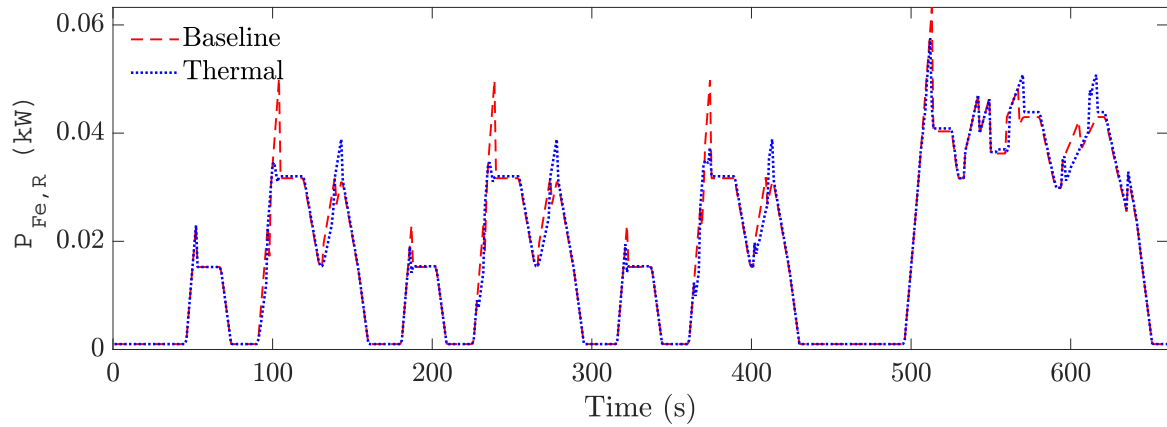


Figure 8.17: Rear PMSM Iron loss $P_{Fe,R}$, for the Baseline and Thermal DP case studies over the JN1015 drive cycle.

tively. It is evident that during motor operation (i.e. non-zero efficiency), the Thermal DP case study demonstrates equal or higher efficiencies compared to the Baseline DP case study.

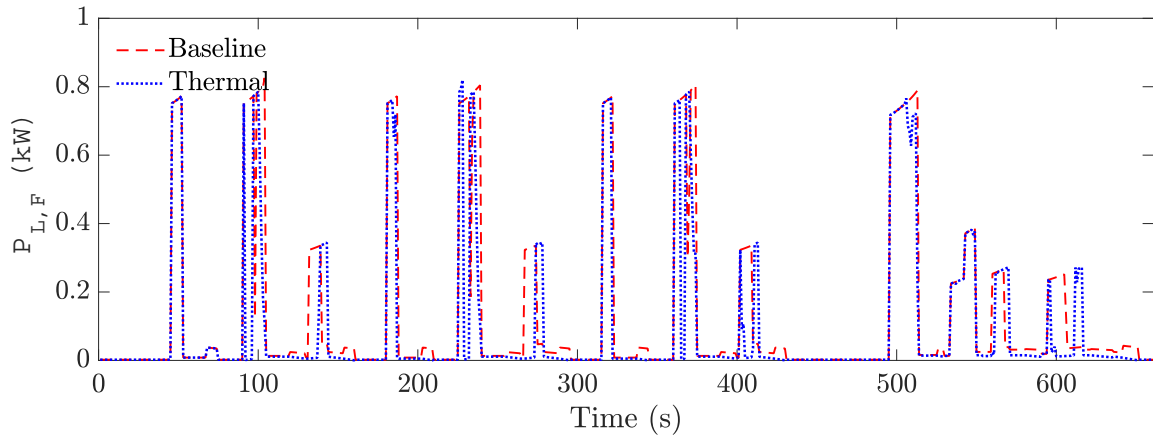


Figure 8.18: Total front PMSM loss $P_{L,F}$, for the Baseline and Thermal DP case studies over the JN1015 drive cycle.

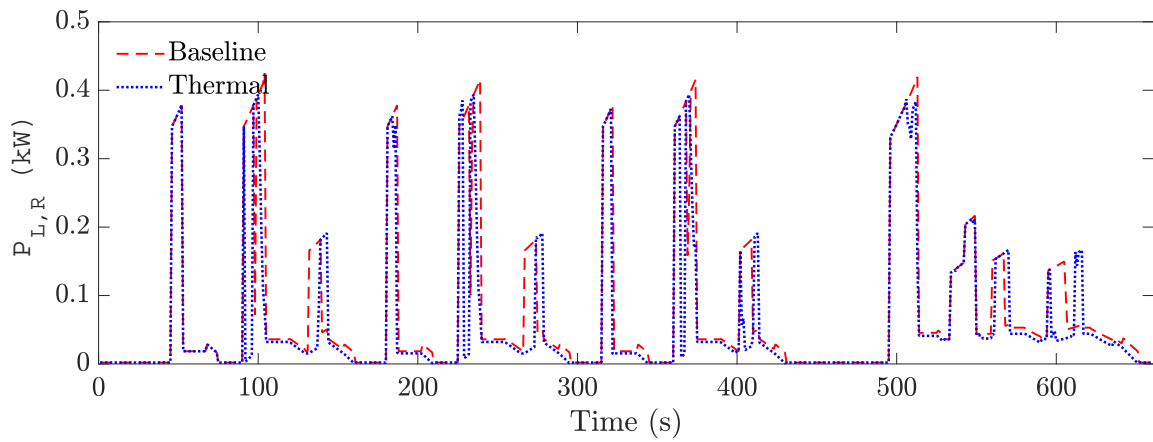


Figure 8.19: Total rear PMSM loss $P_{L,R}$, for the Baseline and Thermal DP case studies over the JN1015 drive cycle.

Table 8.2: Energy losses over the JN1015 drive cycle in other powertrain components: Inverter, Battery and Gearbox

Parameter	Case study	Symbol	Value
Battery energy loss	Baseline	W_B	52.1535 KJ
Battery energy loss	Thermal	W_B	41.1774 KJ
Inverter energy loss	Baseline	W_i	18.4782 KJ
Inverter energy loss	Thermal	W_i	14.1774 KJ
Gearbox energy loss	Baseline	W_g	60.64 KJ
Gearbox energy loss	Thermal	W_g	60.64 KJ

The total powertrain losses are depicted in Figure 8.22. It can be seen there is an 18.38% decrease in the total energy loss in the Thermal DP case study compared to the Baseline DP case study.

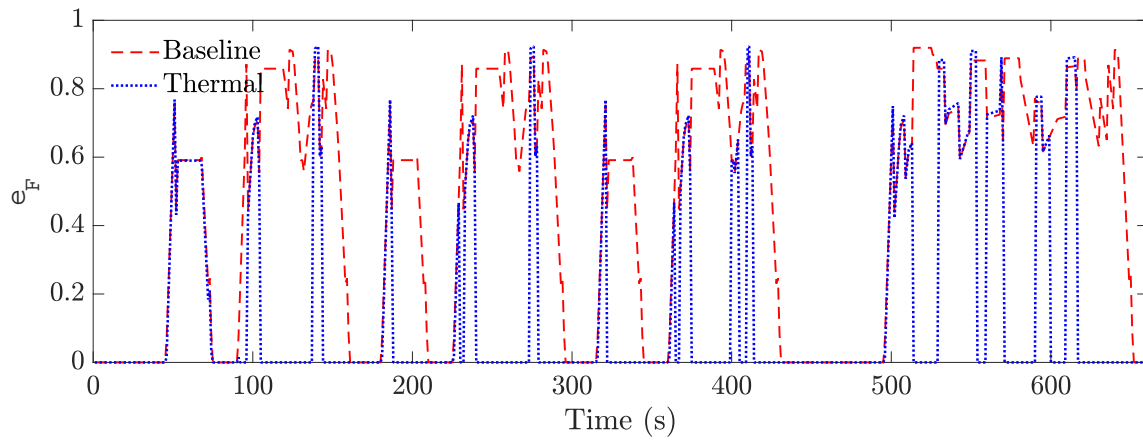


Figure 8.20: Time profile of the front PMSM efficiency e_F , for the Baseline and Thermal DP case studies over the JN1015 drive cycle.

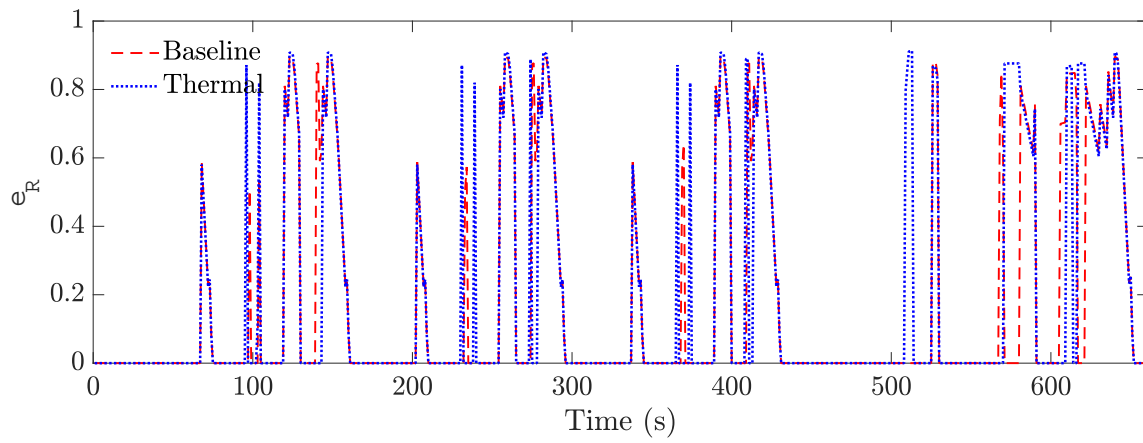


Figure 8.21: Time profile of the rear PMSM efficiency e_R , for the Baseline and Thermal DP case studies over the JN1015 drive cycle.

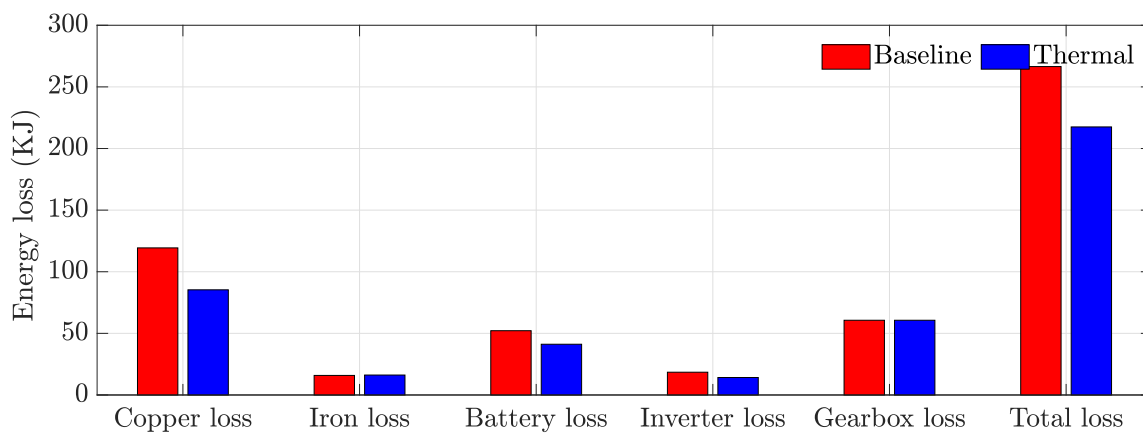


Figure 8.22: Comparison of the drivetrain losses between the Baseline and Thermal DP case studies over the JN1015 drive cycle.

8.4.5 SOC Profiles

The SOC profiles are visualised in Figure 8.23 with results summarised in Table 8.3. It can be seen that there is a 9.48% reduction in battery energy usage in the Thermal DP case study compared to the Baseline DP case study.

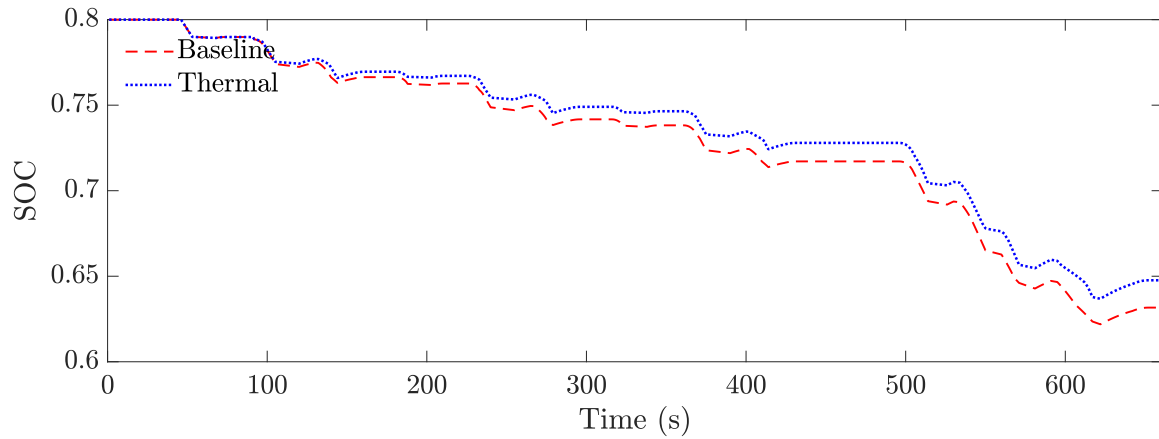


Figure 8.23: SOC time profiles of the Baseline and Thermal DP case studies over the JN1015 drive cycle.

Table 8.3: Final SOC for the Baseline and Thermal DP case studies

Parameter	Case study	Symbol	Value
Final state of charge	Baseline	SOC_{final}	0.6310
Final state of charge	Thermal	SOC_{final}	0.6476

8.5 Chapter Summary

The chapter presented an in-depth analysis of two different Dynamic Programming (DP) energy management strategies implemented on dual-motor EV models. The first standard DP had one state (SOC), and the second DP considered the temperature variation of the traction motors, having three states (SOC, front PMSM stator windings' temperature and rear PMSM stator windings' temperature). The thermal dynamics of the traction motors were modelled using the LPTN method, and the corresponding thermal parameters were identified and validated using experimental data from the industrial partner.

The chapter compared the Baseline and Thermal DP case study solutions and provided insights into the optimal energy management of dual-motor EV powertrains. The powertrain loss values showed that considering the thermal dynamics of the PMSMs reduces the total energy loss by 18.38% in the Thermal DP case study compared to the Baseline DP case study. Moreover, the SOC usage of the Thermal DP case study improved by 9.48% compared to the Baseline DP case study.

The Thermal DP achieved higher efficiency than the Baseline DP in the majority of the JN1015 drive cycle. The chapter analysed the front and rear PMSMs' stator windings' temperature profiles, indicating that the Thermal DP avoids letting one motor overheat and keeps both the front and rear motor temperatures in the same region. Overusing one motor was observed in the rear motor temperature profiles in the Baseline DP case study, leading to an overall less efficient energy management strategy compared to the Thermal DP case study.

In summary, the chapter provided a detailed study of the optimal energy management of dual-motor EV powertrains using DP and thermal modelling. The findings suggested that considering the thermal dynamics of the PMSMs results in a more efficient energy management strategy.

Part IV

Conclusion

Chapter 9

Conclusion

9.1 Summary of Achievements

The **Part Energy Management of HEVs** presented the modelling of a TTR HEV and implemented the ECMS and the global heuristic control strategies and their corresponding real-time versions: Torque levelling Threshold changing Strategy (TTS) and the Real-time TTS (RTTS). The simplified versions of these controllers were also introduced by eliminating one control parameter: Simplified-TTS (STTS) and Real-time STTS (RSTTS).

These strategies were developed based on the insights from XOS [122] and OPSS [6], which were designed for series HEVs. The TTS used the 'Threshold-changing' and 'Load-levelling' mechanisms, which outperformed the conventional ECMS for the WLTP driving cycles for two engine models, as summarised in Tables 6.3 and 6.4.

However, globally tuned controllers are not suitable for real-time applications. Hence, a real-time version of the TTS was developed using feedback control based on the SOC to compute the instantaneous threshold values and the engine torque. It also used a novel algorithm to recognise the specific driving type, such as urban or highway, to output the appropriate initial engine torque. The RTTS achieved similar performance to the TTS over the WLTP drive cycle. The real-time strategy was also tested on an experimental UK driving cycle, demonstrating its effectiveness in achieving CS operation

and improving fuel economy compared to the non-causal ECMS, which uses apriori knowledge of the driving cycle.

The heuristic methods were easily implementable in Simulink using logic gates, and these methods also benefited from shorter tuning time compared to optimisation-based approaches. These attributes make them realistic and favourable for general automotive applications.

In '**Part Energy Management of EVs**', two dual-motor EV models (Baseline and Thermal models), and two Dynamic Programming (DP) energy management strategies were developed (Baseline and Thermal DPs). The Thermal DP considered the thermal dynamics of the PMSMs by modelling and including them in the problem formulation. The optimal power split obtained from the Baseline DP case study was then fed into the Thermal DP environment, where it was discovered that the Thermal DP outperformed the Baseline DP. By considering the temperature-dependent efficiency of the PMSMs, a more optimal and realistic energy management strategy was achieved, resulting in greater minimisation of the PMSM losses. Additionally, it was observed that by using the motors more evenly and avoiding overloading a single motor in the Thermal DP case study, the overall efficiency was increased, resulting in a higher final SOC. The Thermal DP was able to maintain the temperature of the motors at similar levels and prevented either motor from overheating.

9.2 Future Work

Some potential future work based on the knowledge gained from this thesis is summarised in this section.

Chapter 3: Hybrid Electric Vehicle Model

1. Some components in the high-fidelity TTR vehicle model, such as the engine, battery and transmission system, could be further refined (e.g. the modelling of emissions and the degradation of the battery and other power electronics).
2. The thermal dynamics of some components, such as the PMSM and the battery, can be modelled to get a more realistic expression of the efficiency as opposed to steady-state maps.
3. The gearbox can be modelled so that the transient response is taken into account, which could affect the overall energy management solution.
4. The gearbox ratios and shifting strategy could be co-optimised to optimally control the gearshift commands, as well as the continuous power split between the primary and secondary sources.
5. The driver model could be further developed to take realistic reaction times into account in order to be more representative of a human driver.

Chapter 4: Conventional Control Strategies for the Energy Management of HEVs

1. A real-time ECMS could be implemented to act as a benchmark for the real-time novel heuristic methods developed in this work.
2. Other suitable conventional strategies could be implemented to achieve a more accurate benchmark.

Chapter 5: Heuristic Control Strategies for the Energy Management of HEVs

1. For further validation of the novel heuristic methods developed, these methods could be tested in a Hardware-In-the-Loop (HIL) environment and on vehicles.
2. The novel Driving Pattern Recognition (DPR) Algorithm could be tested over more drive cycles for further refinement.

Chapter 6: Simulation results for the Energy Management of HEVs

1. The performance results of the TTS and STTS differed for two different engine models; therefore, more engine types with various power ratings could be studied.
2. The impact of the sizing of the rest of the powertrain components could be analysed.

Chapter 7: Electric Vehicle Model

1. The thermal dynamics of other powertrain components, such as the battery, inverter, gearbox, and DC link, could be modelled and analysed. By modelling the thermal dynamics of these components, a more realistic estimation of the powertrain efficiency can be obtained. As model complexity increases, optimal control tools might no longer be suitable. Therefore, an appropriate optimisation method shall be selected.
2. More accurate gear change responses (e.g. transient response) can be implemented. Modelling the transient response of the gear changes could affect the losses and the optimal energy management solution.
3. A research could be conducted to optimise the brake-force-distribution strategy. This work uses a fixed split ratio of 30-70% between the friction and the regenerative braking (as long as enough regenerative braking is available). However, a more complex brake force distribution can be implemented, which takes other factors, such as slip, into account.
4. To implement heuristic strategies based on the optimal solutions obtained in this work, a high-fidelity vehicle model could be developed for this dual-motor EV. This model would incorporate

the insights gained from the optimal solutions and allow for the implementation of these strategies. With this approach, the vehicle could achieve a more efficient operation and provide a better understanding of the impact of various factors on its performance.

Chapter 8: Optimal Control Problem & Results for the Energy Management of EVs

1. Analysing the theoretical aspects makes it possible to understand the fundamental principles behind the optimal solutions, which can be used to refine the existing strategies or develop new heuristic strategies.
2. Real-time heuristic strategies inspired by DP could be developed and tested in a HIL environment and on vehicles.
3. Further validation of the energy management strategies could be obtained if more drive cycles are tested.

Bibliography

- [1] C. C. Chan, “The state of the art of electric and hybrid vehicles,” *Proceedings of the IEEE*, vol. 90, no. 2, pp. 247–275, Feb 2002.
- [2] “Possible alternative to linear variable differential transformers.” [Online]. Available: <https://www.nrdc.org/issues/energy1>
- [3] K. V. Singh, H. O. Bansal, and D. Singh, “A comprehensive review on hybrid electric vehicles: architectures and components,” *Journal of Modern Transportation*, vol. 27, no. 2, pp. 77–107, 2019.
- [4] P. Othaganont, F. Assadian, and D. J. Auger, “Multi-objective optimisation for battery electric vehicle powertrain topologies,” *Proceedings of the Institution of Mechanical Engineers, Part D: Journal of Automobile Engineering*, vol. 231, no. 8, pp. 1046–1065, 2017.
- [5] A. Sciarretta and L. Guzzella, “Control of hybrid electric vehicles,” *IEEE Control Systems*, vol. 27, no. 2, pp. 60–70, April 2007.
- [6] W. Shabbir, “Control strategies for series hybrid electric vehicles,” Ph.D. dissertation, 2015.
- [7] “Matlab and simulink - mathworks.” [Online]. Available: <https://www.mathworks.com/products/matlab.html>
- [8] F. Un-Noor, S. Padmanaban, L. Mihet-Popa, M. N. Mollah, and E. Hossain, “A comprehensive study of key electric vehicle (ev) components, technologies, challenges, impacts, and future direction of development,” *Energies*, vol. 10, no. 8, p. 1217, 2017.

- [9] “Vehicle mileage and occupancy.” [Online]. Available: <https://www.gov.uk/government/statistical-data-sets/nts09-vehicle-mileage-and-occupancy>
- [10] “Infrastructure for charging electric vehicles.” [Online]. Available: <https://www.gov.uk/government/publications/infrastructure-for-charging-electric-vehicles-approved-document-s>
- [11] M. Guarnieri, “Looking back to electric cars,” in *2012 Third IEEE HISTory of ELection-technology CONference (HISTELCON)*. IEEE, 2012, pp. 1–6.
- [12] A. Demircali, P. Sergeant, S. Koroglu, S. Kesler, E. Öztürk, and M. Tumbek, “Influence of the temperature on energy management in battery-ultracapacitor electric vehicles,” *Journal of cleaner production*, vol. 176, pp. 716–725, 2018.
- [13] J. Y. Yong, V. K. Ramachandaramurthy, K. M. Tan, and N. Mithulananthan, “A review on the state-of-the-art technologies of electric vehicle, its impacts and prospects,” *Renewable and sustainable energy reviews*, vol. 49, pp. 365–385, 2015.
- [14] M. Kebriaei, A. H. Niasar, and B. Asaei, “Hybrid electric vehicles: An overview,” in *2015 International Conference on Connected Vehicles and Expo (ICCVE)*. IEEE, 2015, pp. 299–305.
- [15] A. A. Racz, I. Muntean, and S.-D. Stan, “A look into electric/hybrid cars from an ecological perspective,” *Procedia Technology*, vol. 19, pp. 438–443, 2015.
- [16] M. Ehsani, Y. Gao, and A. Emadi, *Modern electric, hybrid electric, and fuel cell vehicles: fundamentals, theory, and design*. CRC press, 2009.
- [17] F. Porsche, “The first hybrid vehicle.”
- [18] Z. Rahman, K. L. Butler, and M. Ehsani, “A comparison study between two parallel hybrid control concepts,” SAE Technical Paper, Tech. Rep., 2000.
- [19] C. Lin, Z. Filipi, Y. Wang, L. Louca, H. Peng, D. N. Assanis, and J. Stein, “Integrated, feed-forward hybrid electric vehicle simulation in simulink and its use for power management studies,” SAE Technical Paper, Tech. Rep., 2001.

- [20] J. Meisel, W. Shabbir, and S. A. Evangelou, "Evaluation of the through-the-road architecture for plug-in hybrid electric vehicle powertrains," in *Electric Vehicle Conference (IEVC), 2013 IEEE International*. IEEE, 2013, pp. 1–5.
- [21] M. Ehsani, Y. Gao, and J. M. Miller, "Hybrid electric vehicles: Architecture and motor drives," *Proceedings of the IEEE*, vol. 95, no. 4, pp. 719–728, April 2007.
- [22] L. Guzzella, A. Sciarretta *et al.*, *Vehicle propulsion systems*. Springer, 2007, vol. 1.
- [23] T. E. Kraft, "Under review-build your own electric vehicle by s. leitman and b. brandt," 2009.
- [24] J. Larminie and J. Lowry, *Electric vehicle technology explained*. John Wiley & Sons, 2012.
- [25] F. Magnussen, "On design and analysis of synchronous permanent magnet machines for field-weakening operation in hybrid electric vehicles," Ph.D. dissertation, Elektrotekniska system, 2004.
- [26] Z. Guirong, Z. Henghai, and L. Houyu, "The driving control of pure electric vehicle," *Procedia Environmental Sciences*, vol. 10, pp. 433–438, 2011.
- [27] M. Jain and S. S. Williamson, "Suitability analysis of in-wheel motor direct drives for electric and hybrid electric vehicles," in *2009 IEEE Electrical Power & Energy Conference (EPEC)*. IEEE, 2009, pp. 1–5.
- [28] G. Chen and K. Tseng, "Design of a permanent-magnet direct-driven wheel motor drive for electric vehicle," in *PESC Record. 27th Annual IEEE Power Electronics Specialists Conference*, vol. 2. IEEE, 1996, pp. 1933–1939.
- [29] H. Qian, G. Xu, J. Yan, T. L. Lam, Y. Xu, and K. Xu, "Energy management for four-wheel independent driving vehicle," in *2010 IEEE/RSJ international conference on intelligent robots and systems*. IEEE, 2010, pp. 5532–5537.
- [30] "Electric cars, solar and clean energy — tesla united kingdom." [Online]. Available: https://www.tesla.com/en_gb

- [31] F. Caricchi, F. Crescimbin, A. Di Napoli, and M. Marcheggiani, "Prototype of electric vehicle drive with twin water-cooled wheel direct drive motors," in *PESC Record. 27th Annual IEEE Power Electronics Specialists Conference*, vol. 2. IEEE, 1996, pp. 1926–1932.
- [32] R. Wang, Y. Chen, D. Feng, X. Huang, and J. Wang, "Development and performance characterization of an electric ground vehicle with independently actuated in-wheel motors," *Journal of Power Sources*, vol. 196, no. 8, pp. 3962–3971, 2011.
- [33] H. Qian, T. L. Lam, W. Li, C. Xia, and Y. Xu, "System and design of an omni-directional vehicle," in *2008 IEEE International Conference on Robotics and Biomimetics*. IEEE, 2009, pp. 389–394.
- [34] K. M. Rahman, N. R. Patel, T. G. Ward, J. M. Nagashima, F. Caricchi, and F. Crescimbin, "Application of direct-drive wheel motor for fuel cell electric and hybrid electric vehicle propulsion system," *IEEE Transactions on Industry Applications*, vol. 42, no. 5, pp. 1185–1192, 2006.
- [35] T. Guilin, M. Zhiyun, Z. Libing, and L. Langru, "A novel driving and control system for direct-wheel-driven electric vehicle," in *2004 12th symposium on electromagnetic launch technology*. IEEE, 2004, pp. 514–517.
- [36] H. Ma, F. Balthasar, N. Tait, X. Riera-Palou, and A. Harrison, "A new comparison between the life cycle greenhouse gas emissions of battery electric vehicles and internal combustion vehicles," *Energy policy*, vol. 44, pp. 160–173, 2012.
- [37] L. Kütt, E. Saarijärvi, M. Lehtonen, H. Mölder, and J. Niitsoo, "A review of the harmonic and unbalance effects in electrical distribution networks due to ev charging," in *2013 12th International Conference on Environment and Electrical Engineering*. IEEE, 2013, pp. 556–561.
- [38] T. Donato, F. Ingrosso, F. Licci, and D. Laforgia, "A method to estimate the environmental impact of an electric city car during six months of testing in an italian city," *Journal of Power Sources*, vol. 270, pp. 487–498, 2014.
- [39] K. Jorgensen, "Technologies for electric, hybrid and hydrogen vehicles: Electricity from renewable energy sources in transport," *Utilities Policy*, vol. 16, no. 2, pp. 72–79, 2008.

- [40] F. Mwasilu, J. J. Justo, E.-K. Kim, T. D. Do, and J.-W. Jung, "Electric vehicles and smart grid interaction: A review on vehicle to grid and renewable energy sources integration," *Renewable and sustainable energy reviews*, vol. 34, pp. 501–516, 2014.
- [41] E. Sortomme and M. A. El-Sharkawi, "Optimal charging strategies for unidirectional vehicle-to-grid," *IEEE Transactions on Smart Grid*, vol. 2, no. 1, pp. 131–138, 2010.
- [42] C. C. Chan, "The state of the art of electric and hybrid vehicles," *Proceedings of the IEEE*, vol. 90, no. 2, pp. 247–275, 2002.
- [43] Z. Gelmanova, G. Zhabalova, G. Sivyakova, O. Lelikova, O. Onishchenko, A. Smailova, and S. Kamarova, "Electric cars. advantages and disadvantages," in *Journal of Physics: Conference Series*, vol. 1015, no. 5. IOP Publishing, 2018, p. 052029.
- [44] H. Shareef, M. M. Islam, and A. Mohamed, "A review of the stage-of-the-art charging technologies, placement methodologies, and impacts of electric vehicles," *Renewable and Sustainable Energy Reviews*, vol. 64, pp. 403–420, 2016.
- [45] "2017 bolt ev: All-electric vehicle — chevrolet." [Online]. Available: <http://www.chevrolet.com/bolt-ev-electricvehicle.html>
- [46] N. S. Pearre, W. Kempton, R. L. Guensler, and V. V. Elango, "Electric vehicles: How much range is required for a day's driving?" *Transportation Research Part C: Emerging Technologies*, vol. 19, no. 6, pp. 1171–1184, 2011.
- [47] "Government takes historic step towards net-zero with end of sale of new petrol and diesel cars by 2030." [Online]. Available: <https://www.gov.uk/government/news/government-takes-historic-step-towards-net-zero-with-end-of-sale-of-new-petrol-and-diesel-cars-by-2030>
- [48] G. Milev, A. Hastings, and A. Al-Habaibeh, "The environmental and financial implications of expanding the use of electric cars-a case study of scotland," *Energy and Built Environment*, vol. 2, no. 2, pp. 204–213, 2021.

- [49] M. Wolsink, "The research agenda on social acceptance of distributed generation in smart grids: Renewable as common pool resources," *Renewable and Sustainable Energy Reviews*, vol. 16, no. 1, pp. 822–835, 2012.
- [50] M. K. Hidrue, G. R. Parsons, W. Kempton, and M. P. Gardner, "Willingness to pay for electric vehicles and their attributes," *Resource and energy economics*, vol. 33, no. 3, pp. 686–705, 2011.
- [51] K. B. Wipke, M. R. Cuddy, and S. D. Burch, "Advisor 2.1: A user-friendly advanced powertrain simulation using a combined backward/forward approach," *IEEE transactions on vehicular technology*, vol. 48, no. 6, pp. 1751–1761, 1999.
- [52] K. Hauer and R. Moore, "Fuel cell vehicle simulation—part 1: benchmarking available fuel cell vehicle simulation tools," *Fuel cells*, vol. 3, no. 3, pp. 84–94, 2003.
- [53] G. Mohan, F. Assadian, and S. Longo, "Comparative analysis of forward-facing models vs backwardfacing models in powertrain component sizing," in *IET hybrid and electric vehicles conference 2013 (HEVC 2013)*. IET, 2013, pp. 1–6.
- [54] A. Sciarretta and L. Guzzella, "Control of hybrid electric vehicles," *IEEE control systems magazine*, vol. 27, no. 2, pp. 60–70, 2007.
- [55] G. Paganelli, "A general formulation for the instantaneous control of the power split in charge-sustaining hybrid electric vehicles," in *Proc. AVEC 2000, 5th Int. Symp. on Advanced Vehicle Control*, 2000.
- [56] A. Brahma, "Dynamic optimization of mechanical/electrical power flow in parallel hybrid electric vehicles," in *AVEC 2000, 5th Int. Symp. on Adv. Veh. Control, Ann Arbor, Aug. 2000*, 2000.
- [57] U. Zoelch and D. Schroeder, "Dynamic optimization method for design and rating of the components of a hybrid vehicle," *International Journal of Vehicle Design*, vol. 19, no. 1, pp. 1–13, 1998.

- [58] C.-C. Lin, J.-M. Kang, J. W. Grizzle, and H. Peng, “Energy management strategy for a parallel hybrid electric truck,” in *Proceedings of the 2001 American Control Conference*.(Cat. No. 01CH37148), vol. 4. IEEE, 2001, pp. 2878–2883.
- [59] F. R. Salmasi, “Control strategies for hybrid electric vehicles: Evolution, classification, comparison, and future trends,” *IEEE Transactions on Vehicular Technology*, vol. 56, no. 5, pp. 2393–2404, Sept 2007.
- [60] W. Greenwell and A. Vahidi, “Predictive control of voltage and current in a fuel cell–ultracapacitor hybrid,” *IEEE Transactions on Industrial Electronics*, vol. 57, no. 6, pp. 1954–1963, 2009.
- [61] S. Onori and L. Tribioli, “Adaptive pontryagin’s minimum principle supervisory controller design for the plug-in hybrid gm chevrolet volt,” *Applied Energy*, vol. 147, pp. 224–234, 2015.
- [62] H. Hemi, J. Ghouili, and A. Cheriti, “Combination of markov chain and optimal control solved by pontryagin’s minimum principle for a fuel cell/supercapacitor vehicle,” *Energy Conversion and Management*, vol. 91, pp. 387–393, 2015.
- [63] C. Sun, X. Hu, S. J. Moura, and F. Sun, “Velocity predictors for predictive energy management in hybrid electric vehicles,” *IEEE Transactions on Control Systems Technology*, vol. 23, no. 3, pp. 1197–1204, 2014.
- [64] H. Borhan, A. Vahidi, A. M. Phillips, M. L. Kuang, I. V. Kolmanovsky, and S. Di Cairano, “Mpc-based energy management of a power-split hybrid electric vehicle,” *IEEE Transactions on Control Systems Technology*, vol. 20, no. 3, pp. 593–603, 2011.
- [65] L. Johansson, M. Asbogard, and B. Egardt, “Assessing the potential of predictive control for hybrid vehicle powertrains using stochastic dynamic programming,” *IEEE Transactions on Intelligent Transportation Systems*, vol. 8, no. 1, pp. 71–83, 2007.
- [66] L. Johansson and B. Egardt, “A novel algorithm for predictive control of parallel hybrid powertrains based on dynamic programming,” *IFAC Proceedings Volumes*, vol. 40, no. 10, pp. 343–350, 2007.

- [67] K. Uthaichana, S. Bengea, R. DeCarlo, S. Pekarek, and M. Zefran, "Hybrid model predictive control tracking of a sawtooth driving profile for an hev," in *2008 American Control Conference*. IEEE, 2008, pp. 967–974.
- [68] G. Ripaccioli, A. Bemporad, F. Assadian, C. Dextreit, S. D. Cairano, and I. V. Kolmanovsky, "Hybrid modeling, identification, and predictive control: An application to hybrid electric vehicle energy management," in *International Workshop on Hybrid Systems: Computation and Control*. Springer, 2009, pp. 321–335.
- [69] G. Paganelli, G. Ercole, A. Brahma, Y. Guezennec, and G. Rizzoni, "General supervisory control policy for the energy optimization of charge-sustaining hybrid electric vehicles," *JSAE review*, vol. 22, no. 4, pp. 511–518, 2001.
- [70] C. Musardo, G. Rizzoni, Y. Guezennec, and B. Staccia, "A-ecms: An adaptive algorithm for hybrid electric vehicle energy management," *European Journal of Control*, vol. 11, no. 4-5, pp. 509–524, 2005.
- [71] P. Pisu and G. Rizzoni, "A comparative study of supervisory control strategies for hybrid electric vehicles," *IEEE transactions on control systems technology*, vol. 15, no. 3, pp. 506–518, 2007.
- [72] V. H. Johnson, K. B. Wipke, and D. J. Rausen, "Hev control strategy for real-time optimization of fuel economy and emissions," SAE Technical Paper, Tech. Rep., 2000.
- [73] D. Hermance and S. Sasaki, "Hybrid electric vehicles take to the streets," *IEEE spectrum*, vol. 35, no. 11, pp. 48–52, 1998.
- [74] C. G. Hochgraf, M. J. Ryan, and H. L. Wiegman, "Engine control strategy for a series hybrid electric vehicle incorporating load-leveling and computer controlled energy management," SAE Technical Paper, Tech. Rep., 1996.
- [75] F. Tianheng, Y. Lin, G. Qing, H. Yanqing, Y. Ting, and Y. Bin, "A supervisory control strategy for plug-in hybrid electric vehicles based on energy demand prediction and route preview," *IEEE Transactions on Vehicular Technology*, vol. 64, no. 5, pp. 1691–1700, 2014.

- [76] Z. Chen, C. C. Mi, J. Xu, X. Gong, and C. You, "Energy management for a power-split plug-in hybrid electric vehicle based on dynamic programming and neural networks," *IEEE Transactions on Vehicular Technology*, vol. 63, no. 4, pp. 1567–1580, 2013.
- [77] S. Delprat, T.-M. Guerra, and J. Rimaux, "Optimal control of a parallel powertrain: from global optimization to real time control strategy," in *Vehicular Technology Conference, 2002. VTC Spring 2002. IEEE 55th*, vol. 4. IEEE, 2002, pp. 2082–2088.
- [78] G. Paganelli, T. Guerra, S. Delprat, J. Santin, M. Delhom, and E. Combes, "Simulation and assessment of power control strategies for a parallel hybrid car," *Proceedings of the Institution of Mechanical Engineers, Part D: Journal of Automobile Engineering*, vol. 214, no. 7, pp. 705–717, 2000.
- [79] K. van Berkel, R. Titulaer, T. Hofman, B. Vroemen, and M. Steinbuch, "From optimal to real-time control of a mechanical hybrid powertrain," *IEEE Transactions on Control Systems Technology*, vol. 23, no. 2, pp. 670–678, 2015.
- [80] S.-i. Jeon, S.-t. Jo, Y.-i. Park, and J.-m. Lee, "Multi-mode driving control of a parallel hybrid electric vehicle using driving pattern recognition," *Journal of dynamic systems, measurement, and control*, vol. 124, no. 1, pp. 141–149, 2002.
- [81] R. Langari and J.-S. Won, "Intelligent energy management agent for a parallel hybrid vehicle-part i: system architecture and design of the driving situation identification process," *IEEE transactions on vehicular technology*, vol. 54, no. 3, pp. 925–934, 2005.
- [82] N. Fallahi and N. A. HALVAEI, "Intelligent energy management strategy for a separated-axle parallel hybrid electric vehicle," 2014.
- [83] K. Pietruszewicz, P. Waszczuk, and M. Kubicki, "Mfc/imc control algorithm for reduction of load torque disturbance in pmsm servo drive systems," *Applied Sciences*, vol. 9, no. 1, p. 86, 2018.
- [84] M. R. Mehrjou, N. Mariun, M. Karami, N. Misron, and M. A. M. Radzi, "Broken rotor bar detection in ls-pmsms based on statistical features analysis of start-up current envelope," in *2015*

- IEEE 3rd International Conference on Smart Instrumentation, Measurement and Applications (ICSIMA)*. IEEE, 2015, pp. 1–6.
- [85] H. Liang, Y. Chen, S. Liang, and C. Wang, “Fault detection of stator inter-turn short-circuit in pmsm on stator current and vibration signal,” *Applied Sciences*, vol. 8, no. 9, p. 1677, 2018.
- [86] B. Zhang, R. Qu, W. Xu, J. Wang, and Y. Chen, “Thermal model of totally enclosed water-cooled permanent magnet synchronous machines for electric vehicle applications,” in *2014 International Conference on Electrical Machines (ICEM)*. IEEE, 2014, pp. 2205–2211.
- [87] Z. Gao, R. S. Colby, T. G. Habetler, and R. G. Harley, “A model reduction perspective on thermal models for induction machine overload relays,” *IEEE Transactions on Industrial Electronics*, vol. 55, no. 10, pp. 3525–3534, 2008.
- [88] D. G. Dorrell, “Combined thermal and electromagnetic analysis of permanent-magnet and induction machines to aid calculation,” *IEEE Transactions on Industrial Electronics*, vol. 55, no. 10, pp. 3566–3574, 2008.
- [89] L. Alberti and N. Bianchi, “A coupled thermal–electromagnetic analysis for a rapid and accurate prediction of im performance,” *IEEE Transactions on Industrial Electronics*, vol. 55, no. 10, pp. 3575–3582, 2008.
- [90] D. D. Reigosa, P. García, F. Briz, D. Raca, and R. D. Lorenz, “Modeling and adaptive decoupling of high-frequency resistance and temperature effects in carrier-based sensorless control of pm synchronous machines,” *IEEE Transactions on Industry Applications*, vol. 46, no. 1, pp. 139–149, 2009.
- [91] D. D. Reigosa, F. Briz, M. W. Degner, P. García, and J. M. Guerrero, “Magnet temperature estimation in surface pm machines during six-step operation,” *IEEE Transactions on Industry Applications*, vol. 48, no. 6, pp. 2353–2361, 2012.
- [92] D. Reigosa, P. Garcia, F. Briz, D. Raca, and R. D. Lorenz, “Modeling and adaptive decoupling of transient resistance and temperature effects in carrier-based sensorless control of pm synchronous machines,” in *2008 IEEE Industry Applications Society Annual Meeting*. IEEE, 2008, pp. 1–8.

- [93] M. Ganchev, C. Kral, H. Oberguggenberger, and T. Wolbank, "Sensorless rotor temperature estimation of permanent magnet synchronous motor," in *IECON 2011-37th Annual Conference of the IEEE Industrial Electronics Society*. IEEE, 2011, pp. 2018–2023.
- [94] X. Fan, R. Qu, J. Li, D. Li, B. Zhang, and C. Wang, "Ventilation and thermal improvement of radial forced air-cooled fscw permanent magnet synchronous wind generators," *IEEE Transactions on Industry Applications*, vol. 53, no. 4, pp. 3447–3456, 2017.
- [95] R. Camilleri, D. A. Howey, and M. D. McCulloch, "Predicting the temperature and flow distribution in a direct oil-cooled electrical machine with segmented stator," *IEEE Transactions on Industrial Electronics*, vol. 63, no. 1, pp. 82–91, 2015.
- [96] O. Wallscheid and J. Böcker, "Global identification of a low-order lumped-parameter thermal network for permanent magnet synchronous motors," *IEEE Transactions on Energy Conversion*, vol. 31, no. 1, pp. 354–365, 2015.
- [97] N. Jaljal, J.-F. Trigeol, and P. Lagonotte, "Reduced thermal model of an induction machine for real-time thermal monitoring," *IEEE Transactions on Industrial Electronics*, vol. 55, no. 10, pp. 3535–3542, 2008.
- [98] C. Kral, A. Haumer, and S. B. Lee, "A practical thermal model for the estimation of permanent magnet and stator winding temperatures," *IEEE Transactions on Power Electronics*, vol. 29, no. 1, pp. 455–464, 2013.
- [99] T. Huber, W. Peters, and J. Bocker, "A low-order thermal model for monitoring critical temperatures in permanent magnet synchronous motors," 2014.
- [100] J. Nerg, M. Rilla, and J. Pyrhonen, "Thermal analysis of radial-flux electrical machines with a high power density," *IEEE Transactions on industrial electronics*, vol. 55, no. 10, pp. 3543–3554, 2008.
- [101] T. Huber, W. Peters, and J. Böcker, "Monitoring critical temperatures in permanent magnet synchronous motors using low-order thermal models," in *2014 International Power Electronics Conference (IPEC-Hiroshima 2014-ECCE ASIA)*. IEEE, 2014, pp. 1508–1515.

- [102] F. Boseniuk and B. Ponick, "Parameterization of transient thermal models for permanent magnet synchronous machines exclusively based on measurements," in *2014 International Symposium on Power Electronics, Electrical Drives, Automation and Motion*. IEEE, 2014, pp. 295–301.
- [103] G. D. Demetriades, H. Z. De La Parra, E. Andersson, and H. Olsson, "A real-time thermal model of a permanent-magnet synchronous motor," *IEEE Transactions on Power Electronics*, vol. 25, no. 2, pp. 463–474, 2009.
- [104] J. Fan, C. Zhang, Z. Wang, Y. Dong, C. Nino, A. Tariq, and E. Strangas, "Thermal analysis of permanent magnet motor for the electric vehicle application considering driving duty cycle," *IEEE Transactions on Magnetics*, vol. 46, no. 6, pp. 2493–2496, 2010.
- [105] Q. Chen, Z. Zou, and B. Cao, "Lumped-parameter thermal network model and experimental research of interior pmsm for electric vehicle," *CES Transactions on Electrical Machines and Systems*, vol. 1, no. 4, pp. 367–374, 2017.
- [106] L. Zhiyong, W. Xuehuan, and C. Linhong, "Thermal analysis of pmsm based on lumped parameter thermal network method," in *2016 19th International Conference on Electrical Machines and Systems (ICEMS)*. IEEE, 2016, pp. 1–5.
- [107] D. Gaona, O. Wallscheid, and J. Böcker, "Glocal identification methods for low-order lumped parameter thermal networks used in permanent magnet synchronous motors," in *2017 IEEE 12th International Conference on Power Electronics and Drive Systems (PEDS)*. IEEE, 2017, pp. 1–126.
- [108] Y. Zhu, M. Xiao, K. Lu, Z. Wu, and B. Tao, "A simplified thermal model and online temperature estimation method of permanent magnet synchronous motors," *Applied Sciences*, vol. 9, no. 15, p. 3158, 2019.
- [109] S. Evangelou and W. Shabbir, "Dynamic modeling platform for series hybrid electric vehicles." ELSEVIER SCIENCE BV, 2016, pp. 533–540. [Online]. Available: <http://dx.doi.org/10.1016/j.ifacol.2016.08.078>

- [110] A. Shukla, “Modelling and simulation of hybrid electric vehicles,” 2012.
- [111] “Ricardo wave software.” [Online]. Available: <http://www.ricardo.com/en-gb/software/products/wave/>
- [112] X. Li and S. A. Evangelou, “Torque-leveling threshold-changing rule-based control for parallel hybrid electric vehicles,” *IEEE Transactions on Vehicular Technology*, vol. 68, no. 7, pp. 6509–6523, 2019.
- [113] C. M. Shepherd, “Design of primary and secondary cells ii. an equation describing battery discharge,” *Journal of the Electrochemical Society*, vol. 112, no. 7, pp. 657–664, 1965.
- [114] O. Tremblay and L.-A. Dessaint, “Experimental validation of a battery dynamic model for ev applications,” *World Electric Vehicle Journal*, vol. 3, no. 1, pp. 1–10, 2009.
- [115] F. Krismer and J. W. Kolar, “Efficiency-optimized high-current dual active bridge converter for automotive applications,” *IEEE Transactions on Industrial Electronics*, vol. 59, no. 7, pp. 2745–2760, 2012.
- [116] *AFM-140 Axial Flux Motor*.
- [117] M. Thommyppillai, S. Evangelou, and R. Sharp, “Advances in the development of a virtual car driver,” *Multibody System Dynamics*, vol. 22, no. 3, pp. 245–267, 2009.
- [118] L. Serrao, S. Onori, and G. Rizzoni, “Ecms as a realization of pontryagin’s minimum principle for hev control,” in *American Control Conference, 2009. ACC’09*. IEEE, 2009, pp. 3964–3969.
- [119] C. Lin, J.-M. Kang, J. W. Grizzle, and H. Peng, “Energy management strategy for a parallel hybrid electric truck,” in *Proceedings of the 2001 American Control Conference*, vol. 4, 2001, pp. 2878–2883.
- [120] A. Sciarretta, M. Back, and L. Guzzella, “Optimal control of parallel hybrid electric vehicles,” *IEEE Transactions on control systems technology*, vol. 12, no. 3, pp. 352–363, 2004.

- [121] X. Li, A. Nazemi, and S. A. Evangelou, "Real-time adaptive heuristic control strategy for parallel hybrid electric vehicles," in *IECON 2018-44th Annual Conference of the IEEE Industrial Electronics Society*. IEEE, 2018, pp. 2133–2138.
- [122] W. Shabbir and S. A. Evangelou, "Exclusive operation strategy for the supervisory control of series hybrid electric vehicles," *IEEE Transactions on Control Systems Technology*, vol. 24, no. 6, pp. 2190–2198, 2016.
- [123] J. T. Kessels, M. W. Koot, P. P. Van Den Bosch, and D. B. Kok, "Online energy management for hybrid electric vehicles," *IEEE Transactions on vehicular technology*, vol. 57, no. 6, pp. 3428–3440, 2008.
- [124] P. Mock, J. Kühlwein, U. Tietge, V. Franco, A. Bandivadekar, and J. German, "The wltp: How a new test procedure for cars will affect fuel consumption values in the eu," *International Council on Clean Transportation*, vol. 9, pp. 35–47, 2014.
- [125] X. Yan, J. Fleming, C. Allison, and R. Lot, "Portable automobile data acquisition module (adam) for naturalistic driving study," 2017.
- [126] B. Chen, X. Pan, and S. A. Evangelou, "Optimal energy management of series hybrid electric vehicles with engine start-stop system," *arXiv preprint arXiv:2203.16126*, 2022.
- [127] H. Ding, X. Gong, and Y. Gong, "Estimation of rotor temperature of permanent magnet synchronous motor based on model reference fuzzy adaptive control," *Mathematical Problems in Engineering*, vol. 2020, 2020.
- [128] P. Sergeant and A. Van den Bossche, "Reducing the permanent magnet content in fractional-slot concentrated-windings permanent magnet synchronous machines," in *2012 XXth International Conference on Electrical Machines*, 2012, pp. 1405–1411.
- [129] P. Nguyen Phuc, H. Vansompel, D. Bozalakov, K. Stockman, and G. Crevecoeur, "Inverse thermal identification of a thermally instrumented induction machine using a lumped-parameter thermal model," *Energies*, vol. 13, no. 1, p. 37, 2019.

- [130] “What is a resistance thermometer (rtd, pt100, prt) sensor - reference information.” [Online]. Available: <https://www.tc.co.uk/rtd-pt100-information/what-is-resistance-thermometer.html#rtd-theory>
- [131] R. L. Murray and K. E. Holbert, “Radiation and materials,” in *Nuclear Energy (Eighth Edition)*. Butterworth-Heinemann, 2020, pp. 81–99.
- [132] J. Lee and J.-I. Ha, “Temperature estimation of pmsm using a difference-estimating feedforward neural network,” *IEEE Access*, vol. 8, pp. 130 855–130 865, 2020.
- [133] K. Bingi, B. R. Prusty, A. Kumra, and A. Chawla, “Torque and temperature prediction for permanent magnet synchronous motor using neural networks,” in *2020 3rd International Conference on Energy, Power and Environment: Towards Clean Energy Technologies*. IEEE, 2021, pp. 1–6.
- [134] H. Guo, Q. Ding, Y. Song, H. Tang, L. Wang, and J. Zhao, “Predicting temperature of permanent magnet synchronous motor based on deep neural network,” *Energies*, vol. 13, no. 18, p. 4782, 2020.
- [135] H. A. Yavasoglu, Y. E. Tetik, and H. G. Ozcan, “Neural network-based energy management of multi-source (battery/uc/fc) powered electric vehicle,” *International Journal of Energy Research*, vol. 44, no. 15, pp. 12 416–12 429, 2020.
- [136] F. Biral, “Massimo guiggiani: The science of vehicle dynamics: handling, braking, and ride of road and race cars,” 2017.
- [137] O. Sundstrom and L. Guzzella, “A generic dynamic programming matlab function,” in *2009 IEEE control applications,(CCA) & intelligent control,(ISIC)*. IEEE, 2009, pp. 1625–1630.
- [138] D. Bertsekas, *Dynamic programming and optimal control: Volume I*. Athena scientific, 2012, vol. 1.
- [139] M. Hasanzadeh and Z. Rahmani, “Real-time optimization of plug-in hybrid electric vehicles based on pontryagin’s minimum principle,” *Clean Technologies and Environmental Policy*, vol. 23, 11 2021.